DISSERTATION | DOCTORAL THESIS

Titel | Title

Molecularly Imprinted Polymers for Sensing in Water: Penicillin VK and Gold Nanoparticles

verfasst von | submitted by

Mahdieh Bagheri

angestrebter akademischer Grad | in partial fulfilment of the requirements for the degree of

Doktorin der Naturwissenschaften (Dr.rer.nat.)

Wien | Vienna, 2025

Studienkennzahl lt. Studienblatt | Degree programme code as it appears on the student record sheet:	UA 796 605 419
Dissertationsgebiet lt. Studienblatt | Field of study as it appears on the student record sheet:	Chemie
Betreut von | Supervisor:	Univ.-Prof. Mag. Dr. Peter Lieberzeit

Acknowledgments

The completion of this thesis, the result of several years of work, would not have been possible without the support, encouragement and inspiration of many people. I am so grateful to all those who have accompanied me during my Ph.D. studies at University of Vienna.

First and foremost, I would like to express my deepest gratitude to my supervisor, Univ.-Prof. Mag. Dr. Peter Lieberzeit, for providing me with the opportunity to be a part of his working group and for his invaluable guidance, encouragement and generous support.

I would also like to thank all members of the Department of Physical Chemistry, particularly Dieter, for his helpful comments and his unfailing assistance with technical matters. My warm thanks go as well to Elke Lampert, whose support with administrative issues was invaluable, and whose kind conversations always made my visits to her office a pleasure. Moreover, I want to thank Dr. Christian Dank for his support with the IR and NMR spectroscopy.

I am very grateful to my colleagues Julia, Chiara Luna, Houra, Ester, Olen, Adriana, Felix and Shahin. Thank you for the nice times we shared together, for creating such a friendly atmosphere and for the fun moments inside and outside the lab.

My deepest gratitude goes to my family for their endless love, encouragement and belief in me. I am especially grateful to my parents for always believing in me and their constant prayers and support, even from a distance. I am also grateful to my two beloved sisters, Soheila and Anahita, for their love and for always cheering me on in difficult times.

This thesis would not have been possible without the presence of my friends, particularly Sara, who have been by my side and inspired me with their love and support. I would especially like to thank Michael, who supported and motivated me so much during the last steps of this journey. Your encouragement meant the world to me.

Finally, I gratefully acknowledge the Austrian Research Promotion Agency (FFG) for funding the project of *"Fabrication of Multi-Analyte Nano sensors for Biological Targets (AquaNOSE)"* through a grant agreement no. 864893.

To my beloved parents,

and

to all the brave and free women of Iran.

Contents

1. Introduction 1

1.1. Objectives of Research 1

1.2. Target Analytes 3

1.2.1. Penicillin V 3

1.2.2. Gold Nanoparticles 5

2. Theoretical Background 8

2.1. Molecular Imprinting 8

2.1.1. Homopolymer MIP System 9

2.1.2. Co-Polymer MIP System 12

2.1.3. Precipitation Polymerization 12

2.1.4. In-Situ Polymerization 13

2.1.5. Controlled Radical Polymerization 13

2.2. MIP Characterization Methods 16

2.2.1. Scanning Electron Microscopy 17

2.2.2. Atomic Force Microscopy 18

2.2.3. Dynamic Light Scattering 20

2.2.4. Zeta Potential 22

2.3. Chemosensors 23

2.3.1. Quartz Crystal Microbalance 24

2.3.2. Cyclic Voltammetry 26

3. Chemicals and Methods 29

3.1. Chemicals, Material and Devices 29

3.1.1. Custom Sensor Electrodes Manufacturing Methods 33

3.1.2. Electrode Screen Printing 33

3.1.3. Physical Vapor Deposition 34

3.1.4. QCM Measuring Cell 36

3.1.5. QCM Measurements 37

3.1.6. FBAR Measurements 39

3.2. Materials Characterization 41

3.2.1. Scanning Electron Microscopy 41

3.2.2. ATR-FTIR 41

3.2.3. Atomic Force Microscopy 41

3.2.4. Zeta Potentials of Particles 43

3.2.5. Surface Zeta Potentials 43

4. Penicillin VK Sensor 44

4.1. Experimental 44

4.1.1. Pen VK NIP and MIP NPs 44

4.1.2. Pen VK Conversion 46

4.1.3. Pen V Free Acid MIP NPs 46

4.1.4. Optimization of Binding Affinity of Pen V MIP NPs 47

4.1.5. MIP and NIP QCM Preparation 48
4.1.6. Cyclic Voltammetry 49
4.2. Results and Discussion 50
4.2.1. Morphology and Size of MIP and NIP NPs 50
4.2.2. Verification of Pen V Acid Formation 55
4.2.3. Sensor Characteristic 58
4.2.4. Optimization of Binding Affinity of Pen V MIP NPs 65
4.2.5. Cyclic Voltammetry 70
4.3. Summary and Conclusion 72
5. Gold Nanoparticles Sensors 74
5.1. Experimental 74
5.1.1. In-Situ Polymerization of Au NPs on QCM Chips 74
5.1.2. Au NPs Extraction from the Polymer Matrix 77
5.1.3. Au NPs Surface Modification 78
5.1.4. Zeta Potential Measurements 79
5.2. Results and Discussion 80
5.2.1. Optimizing In-Situ Polymerization 80
5.2.2. Polymer Thickness 81
5.2.3. Template Extraction 84
5.2.4. Au NPs Surface Modification 86
5.2.5. Sensor Measurements 92
5.3. Summary and Conclusion 101
6. Conclusions and Outlook 103
Abstract 105
Zusammenfassung 106
References 108
Scientific Contribution 116

Abbreviation	Full Term
AFM	Atomic Force Microscopy
ATR-FTIR	Attenuated Total Reflectance Fourier Transform Infrared Spectroscopy
ATRP	Atomic Transfer Radical Polymerization
Au NP	Gold Nanoparticle
CRP	Controlled Radical Polymerization
CTA	Chain Transfer Agent
dH_2O	Distilled Water
DLS	Dynamic Light Scattering
EDL	Electrical Double Layer
FBAR	Film Bulk Acoustic Resonators
HPLC	High-Performance Liquid Chromatography
ICP-MS	Inductively Coupled Plasma Mass Spectrometry
IF	Imprinting Factor
LC	Liquid Chromatography
LoD	Limit of Detection
MIP	Molecularly Imprinted Polymer
MNP	Magnetite Nanoparticle
MS	Mass Spectrometry
NIP	Non-Imprinted Polymer
NMP	Nitroxide-Mediated Polymerization
PVP	Polyvinylpyrrolidone
QCM	Quartz Crystal Microbalance
RAFT	Reversible Addition-Fragmentation Chain Transfer
RDRP	Reversible-Deactivation Radical Polymerization
SEM	Scanning Electron Microscopy
SF	Selectivity Factor
SPE	Solid Phase Extraction
TDD	Targeted Drug Delivery

TEM	Transmission Electron Microscopy
TSM	Thickness Shear Mode
WHO	World Health Organization

1. Introduction

1.1. Objectives of Research

This thesis is divided into two parts, focusing on the design and development of artificial sensors based on molecularly imprinted polymers (MIPs) for the detection of various analytes, ranging from small molecules to engineered nanoparticles (ENPs).

The first part builds upon the AquaNOSE project, which was supported by the Austrian Research Promotion Agency (FFG) under grant agreement number 864893. The main goal of this project was to develop advanced multi-analyte nano sensors capable of detecting a wide range of biological targets, from small molecules to larger biological entities. A particular focus of the AquaNOSE project has been the detection of Penicillin.

In this section, the thesis contributes to the design and development of thin film and nanoparticle (NP) MIPs to detect Penicillin V (Pen V) in liquid media. Previous work in the group on Penicillin thin-film MIPs successfully developed acrylate-based MIP thin-film sensors for the detection of Penicillin V potassium (Pen VK), Penicillin G potassium (Pen GK) and Amoxicillin sodium (Amo Na) [1]. Building on this foundation, the second approach focused on synthesizing Pen V MIP NPs by:

1. Clarifying that the approach involves synthesizing acrylate-based MIP NPs
2. Maintaining the size specification of less than 200 nm
3. More clearly linking the size requirement to the project's specifications and targets
4. Retaining the goal of enabling specific and sensitive detection capabilities

The synthesized MIP NPs are incorporated into the detection system by depositing them onto a quartz crystal microbalance (QCM). This approach combines the selectivity of MIPs with the sensitivity of QCM measurements, potentially offering improved performance in Penicillin detection.

The second section focuses on sensing ENPs based on MIP sensors in aqueous solutions. The primary work on ENPs detection began at the University of Vienna within the EU project "INSTANT" (EU-FP7-NMP-2011-SME-5-NMP4-SE-2012-280550), using polyurethane (PU) MIPs. Former PhD students, Leo Schranzhofer and Christoph Jungmann, successfully imprinted different series of ENPs, such as Ag [2], TiO_2, ZnO using various imprinting strategies including bulk, sedimentation and stamp imprinting.

Later, the work evolved with the idea of imprinting metal NPs MIPs in the "SMARTNANO" project (funded by the Austrian Science Fund (FWF), project no. I3568-N28). Predecessors Monika Marjanovic and Shahin Haghdoust used in-situ polymerization to develop an in-situ polymer on a multi-parametric transducer capable of measuring three different parameters: impedance, frequency shift and heat transfer resistance. This work demonstrated promising results in imprinting magnetite nanoparticles (MNPs) and Ag NPs.

Despite successful work in ENPs imprinting and MIP sensor development, gold nanoparticles (Au NPs) remained a more challenging and problematic analyte to imprint and remove. The QCM results in previous research projects did not show favorable outcomes for Au NPs. Therefore, this thesis focuses on three main aspects:

1. Implementing a controlled radical polymerization (CRP) method for in-situ imprinting of Au NPs to achieve an even polymer layer and controlled polymer thickness.
2. Improving Au NP removal by modifying the stabilizer layer of the NPs.
3. Enhancing the affinity assay of Au NP MIP and characterizing the sensitivity pattern of MIPs based on the particle core, shell and sizes.

These approaches aim to overcome the challenges associated with Au NP imprinting and improve the overall performance of Au NP MIP sensors.

1.2. Target Analytes

1.2.1. Penicillin V

Pharmaceuticals are designed to enhance the health of humans and animals; however, their presence in the environment, even at low concentrations (ng/L and below), can harm natural ecosystems, which in turn may affect both human and animal health. These drugs find their way into surface waters and sediments through various channels, including effluents from pharmaceutical manufacturing, improper disposal and metabolic excretion [3]. This has harmful effects on the environment, such as impacts on aquatic organisms, the development of antibiotic resistance in bacteria and mixture effects from multiple pharmaceuticals. The assessment of the presence of these components, even in limited amounts, is challenging due to the mixture of compounds, their metabolites and transformation products. Another challenge is the limited data on long-term, low-dose effects [4]. These issues emphasize the need for a more sustainable approach to pharmaceutical use and disposal to minimize environmental impacts. One of the most promising solutions in this case is the sensitive scanning of low amounts of these compounds in wastewater for better and more efficient wastewater treatment.

The discovery of Penicillin by Alexander Fleming in 1928 [5] brought about a major change in anti-infective medicine and became one of the most used β-lactams antibiotic worldwide. These powerful compounds have become essential in both human and veterinary medicine, serving dual roles as infection preventatives [6] and growth promoters in animal food supplements [7,8]. The versatility of Penicillins lies in their molecular structure: a variable R group attached to an important β-lactam ring, which is responsible for their ability to fight bacteria. This structural flexibility has allowed the development of multiple types of Penicillins, each designed for specific bacterial threats [9]. Figure 1 renders the chemical structure of three famous members of the Penicillins family: Pen V, Pen G and Amo.

Penicillin G R= CH_2Ph

Penicillin V R= CH_2OPh

Amoxicillin R=$CH(NH_2)PhOH$

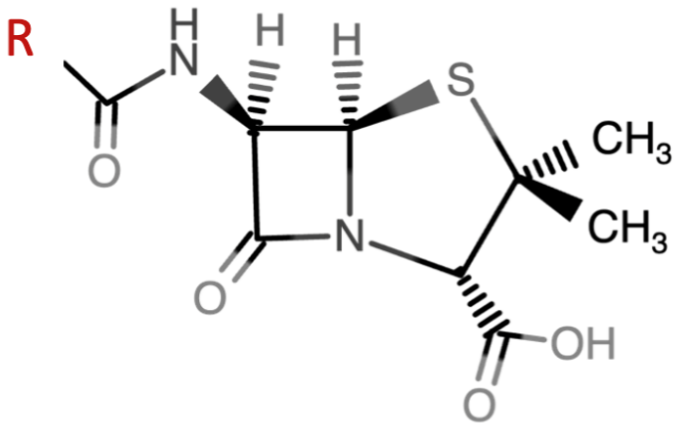

Figure 1: Penicillin structural homology: conserved β-lactam ring and variable R groups.

Antibiotics, especially the Penicillin group, have a massive effect on wastewater pollution. Antibiotic contamination affects microbial communities, algae, plants and animals in aquatic ecosystems [10]. Numerous studies report antibiotic resistance in various cases which is a big concern in human and animal health. Mechanisms of antibiotic resistance development include decreased permeability, biofilm formation, efflux pump modification and enzyme synthesis that hydrolyze drugs [11]. The World Health Organization's (WHO) AWaRe (Access, Watch, Reserve) classification framework shows that antibiotic consumption patterns from 2000 to 2021 increased globally [12,13], especially in low- and middle-income countries. This emphasizes the need for improved monitoring, regulations and investments to promote appropriate antibiotic use in terms of reducing antimicrobials (AMs) resistance [14,15].

Several methods have been described for the identification and quantification of the most prescribed antibiotics, including various classes of Penicillin. Some methods combine solid phase extraction (SPE), liquid chromatography (LC) and tandem mass spectrometry (MS/MS) to analyze various antibiotics in wastewater samples [16,17]. High-performance liquid chromatography–tandem mass spectrometry (HPLC–MS/MS) is useful for identifying and quantifying AMs [18,19]. Immunosensor methods combining different determination techniques such as fluorescence [20] and electrochemical transducers [21] are widely employed. Although these methods are sensitive and selective, they can be expensive and time-consuming. Despite their advantages, the cost and

duration of immunosensor-based analyses may limit their practical application in some settings. Hence, MIPs, also known as artificial antibodies, can serve as a straightforward screening method [22,23]. MIPs combined with various transducers such as electrochemical, optical, mass-sensitive and thermal transducers have indeed become a significant topic in research for detecting a wide range of targets. This approach offers several advantages, such as high selectivity, stability and cost-effectiveness compared to traditional antibody-based methods. Section 2.1 will discuss this topic in more detail.

1.2.2. Gold Nanoparticles

Gold nanoparticles (Au NPs) are engineered nanomaterials that typically range from 1 to 150 nm in diameter. Their small size gives them unique optical, electronic and catalytic properties. Au NPs find wide applications in pharmacy, biomedicine, industry, consumer products and analytical chemistry [24]. Au NPs, as a core of nano pharmaceuticals, have attracted considerable attention in cancer treatment [25] and in advanced medical applications due to the possibility to control their size and morphology, as well as their ease of functionalization with various molecules, including antibodies, DNA and drugs. These properties make Au NPs a good choice for targeted drug delivery (TDD) [26], where precise delivery and specific interactions are crucial.

To date, Au NPs are utilized in many areas as shown in Figure 2 due to their high surface area-to-volume ratio and versatile surface properties.

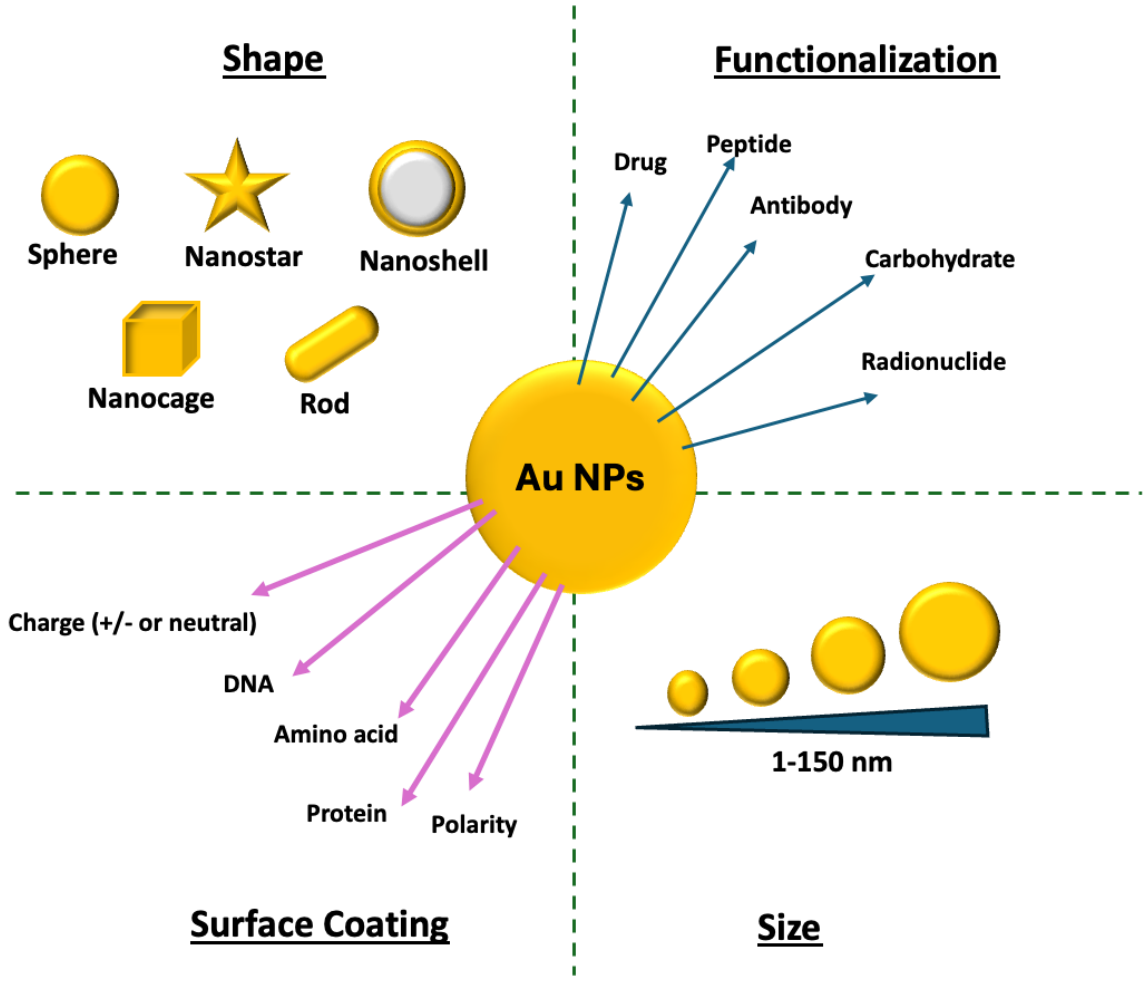

Figure 2: Schematic illustration of Au NPs with diverse morphologies, dimensions, surface coating and functionalization [27].

However, aside from their advantages, recent studies have investigated the environmental fate and effects of Au NPs after entering wastewater treatment plants and being released into the environment. These investigations focus on both short- and long-term health impacts on organisms and the broader ecosystem, highlighting potential risks alongside the benefits of Au NP technology [28,29]. Moreover, many in vivo studies show Au NPs can be collected in organs such as the liver, spleen and kidneys, potentially causing oxidative damage and cytotoxicity [30]. Au NP size, shape, surface coating and functionalization affect toxicity. For example, smaller Au NPs (~20 nm) are generally more toxic than larger ones (~80 nm). In terms of shape, spherical and prismatic particles show higher toxicity than others [31]. Overall, there is a complex interplay

between Au NP physicochemical properties and their biological interactions. Furthermore, the accumulation of Au NPs in sewage treatment plant biomass and their later transfer to ecosystems through biosolids application may lead to potential ecotoxicological risks to the soil microbial communities at environmentally relevant concentrations. The persistence and bioavailability of Au NPs in these complex matrices and their long-term effects on microbial diversity, function and ecosystem processes require further research [32].

Additionally, innovative modern methods for rapid and efficient detection of Au NPs in environmental samples need to be developed. Various analytical methods are available for the identification of NPs, including microscopic techniques (TEM, SEM, AFM), spectroscopic methods (IR, XRD, XPS, EDX) and other specialized techniques such as dynamic light scattering (DLS) and MS. Electron microscopy methods (SEM and TEM) are primarily used to determine NP morphology and size, with scanning electron microscopy (SEM) providing surface information and transmission electron microscopy (TEM) providing insights into internal structure. DLS is popular for measuring the size and distribution in colloidal solutions and calculating the hydrodynamic radius based on Brownian motion. Spectroscopic techniques provide information on the structural properties and composition of NPs. Inductively coupled plasma mass spectrometry (ICP-MS), especially single NP ICP-MS has become increasingly important for the analysis of metal NPs and their elemental composition. While these methods provide comprehensive characterization, they often require expensive equipment, extensive sample preparation and skilled operators. The choice of technique depends on the specific characteristics of the investigated NP and the information required for the application or study.

2. Theoretical Background

2.1. Molecular Imprinting

The concept of molecular recognition is finely exemplified by selective antibodies and enzymes in nature. But what if one could create artificial materials that function similarly to these natural receptors? Answering this challenge, MIPs have emerged as an excellent choice in the world of sensors.

MIPs are polymers designed to recognize and capture specific molecules, much like a key fitting into a lock [33,34]. These "plastic antibodies" are now widely used in applications ranging from environmental monitoring to medical diagnostics [35]. What makes MIPs special is their ability to create three-dimensional cavities within a polymer matrix, allowing for custom-designed receptors fit target molecules [36].

This molecular-level precision, combined with the versatility and stability of synthetic polymers, makes MIPs a powerful alternative to their natural compeer. By offering the selectivity of biological receptors with the robustness of synthetic materials, MIPs are opening a new chapter in sensing technology and molecular recognition. MIPs are synthesized through a process involving functional monomers and cross-linkers, arranged precisely around template molecules. This molecular architecture begins with the formation of a complex between functional monomers and the template. Subsequently, polymerization occurs in the presence of cross-linkers and initiators, resulting in a robust polymeric matrix. The final step involves the extraction of the template, leaving behind cavities that mirror the target molecule in size, shape and chemical affinity (Figure 3).

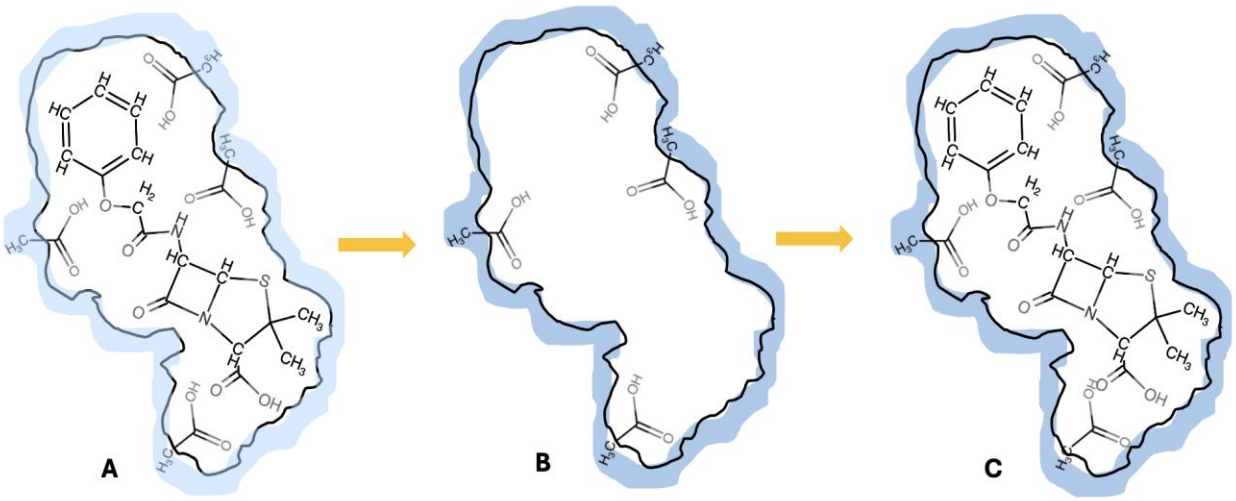

Figure 3: Three steps of the molecular imprinting process: (A) Template imprinting, (B) Template extraction, (C) Template rebinding (MAA shown as monomer and Pen V as imprinted template).

Both in nature and chemical sensors, many types of interactions, be it non-polar, π-π, dipolar/hydrogen bonding etc. are employed. A variety of monomers and cross-linkers are available to suit the target analyte. The polymer matrices produced in this way exhibit favorable chemical, mechanical and thermal stability.

2.1.1. Homopolymer MIP System

The selection of suitable functional monomers and cross-linkers is very important to create effective MIPs with high selectivity and affinity for target analytes. The choice of monomer should aim to maximize template-monomer interactions. Based on the chemical structure of the template, the common series of MIPs are classified according to the type of monomer (Figure 4). Acrylic MIPs, based on acrylic and methacrylic acid derivatives, are widely used due to their high ability to form hydrogen bonds and electrostatic interactions [37]. Vinyl MIPs, using heterocycle-based monomers such as 4-Vinylpyridine (4-VP) and 2-Vinylpyridine (2-VP), are more suitable for templates with acidic functional groups [38]. Other popular types include Styrene-based MIPs,

polyethylene glycol (PEG)-based MIPs and others, each with their advantages and suitable for a variety of purposes and applications [39].

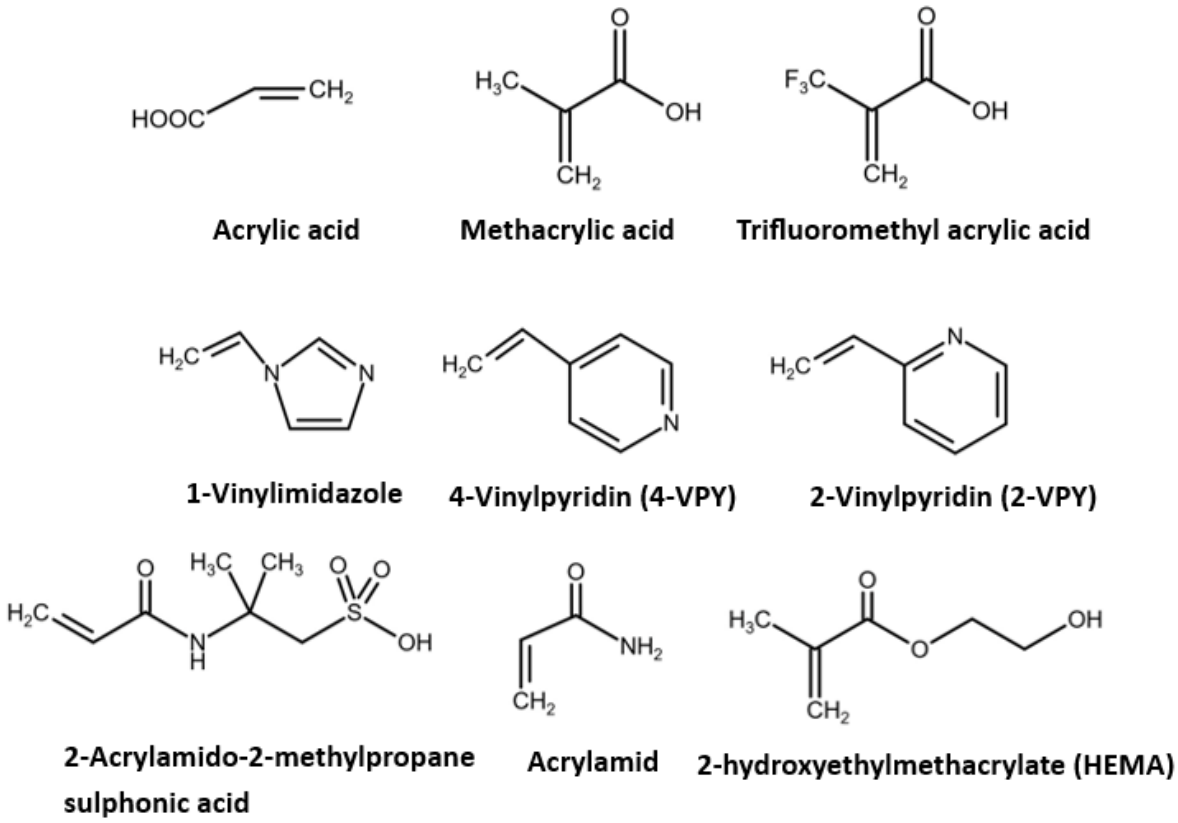

Figure 4: Structure of the most common monomers used for molecular imprinting [40].

Figure 5 shows the most common cross-linker types used in synthesizing the polymer. The choice of cross-linker depends on the desired polymer properties: rigidity, porosity and hydrophilicity. Highly cross-linked polymers tend to form rigid structures with high porosity, while less cross-linked polymers may have a gel-like structure.

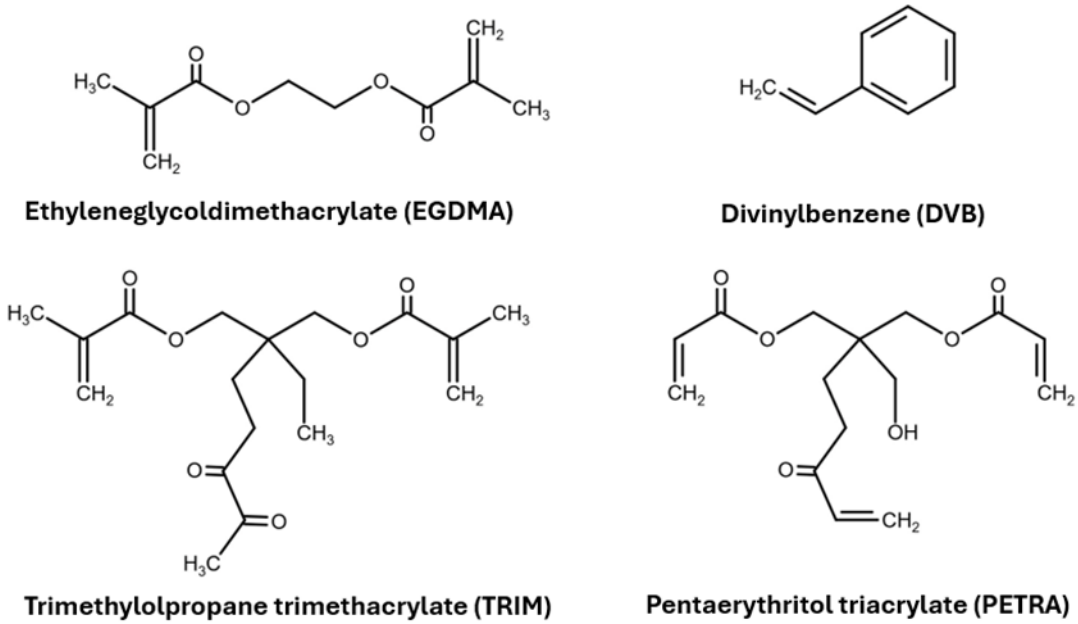

Figure 5: Structure of the most common cross-linkers used for molecular imprinting [40].

Hydrophilic cross-linkers (such as MBA or PEGDMA) can increase the swelling capacity of the polymer in aqueous media [41]. Hydrophobic cross-linkers (such as DVB) can reduce swelling and improve stability in organic solvents. Thermal and mechanical stability is generally higher in highly cross-linked polymers (using DVB or TRIM) [42].

Moreover, the choice of cross-linker can affect whether the polymer forms beads, a monolith, or a thin film. In precipitation polymerization, the choice and concentration of cross-linker can influence the size and uniformity of polymer particles.

A homopolymer consists of only one type of repeating monomer unit. When synthesized with a single cross-linker, these polymers have more predictable properties based on the characteristics of the monomer and the cross-linker chosen. This uniformity leads to more consistent and easily controllable polymer structures and properties.

2.1.2. Co-Polymer MIP System

A co-monomer system uses different monomers in a polymer structure, often combined with various cross-linkers. This approach offers more flexibility in tuning polymer properties. Advantages include improved performance, enhanced mechanical properties and the ability to create polymers with a wider range of properties suitable for specific applications, potentially leading to more versatile and efficient materials.

Many studies have demonstrated improved performance for template detection by using dual-monomer MIPs, where the MIPs are prepared using two functional monomers [43,44]. While the chosen monomers must complement each other in terms of their interaction with the template molecule, the combination of monomers is a critical factor in determining the performance of the resulting polymer.

Even though using multiple functional monomers can potentially enhance the recognition and binding properties of MIPs, it is not easy to mix any two or more monomers. Additionally, many factors should be considered, such as polymerization kinetics of different monomers, the risk of non-specific binding in complex matrices and the correct spatial arrangement of monomers around the template. These factors, among others, can significantly impact the effectiveness of the MIP [45-47].

2.1.3. Precipitation Polymerization

In precipitation polymerization, the monomer, initiator and cross-linker are dissolved in a solvent. As polymerization progresses, the growing polymer chains become insoluble and precipitate from the solution. Precipitation polymerization, as a simple one-step method, often produces uniform, spherical particles without the need for stabilizers or surfactants [48-50]. Particle size and morphology can be influenced by factors such as monomer concentration, initiator type and concentration, solvent type and their respective ratios [51,52]. Besides all the advantages of high-

quality MIP NP production, the main disadvantages are the excessive use of solvent and template [49].

In most cases, precipitation polymerization of acrylic monomers (e.g., MAA-based systems) yields nanoparticles with uniform size distribution [53], which can subsequently be functionalized with various chemical groups to improve performance in specific applications.

2.1.4. In-Situ Polymerization

In-situ polymerization refers to synthesizing MIPs directly on the sensor surface or within the sensor structure, rather than separately and then coating them onto the sensor. In-situ polymerization is a powerful approach that enables highly integrated and efficient sensing in MIP sensor technology. Advantages include better adhesion and contact between the MIP and the transducer element, as well as control over MIP thickness and morphology. This method is mostly used in MIPs functionalized with core-shell ENPs such as Au, Ag, Fe_3O_4, SiO_2 and TiO_2 [54-57]. Nevertheless, despite these benefits, in-situ polymerization also presents challenges. For example, in electropolymerized MIPs, the range of suitable monomers is restricted because they must provide both electrochemical activity and molecular recognition capability [58-60].

In addition, achieving precise thickness and uniformity of the MIP layer, as well as avoiding interference from sensor components during polymerization, remain significant difficulties [61]. Controlled radical polymerization has been proposed as a solution to overcome these limitations and to enable more reliable MIP structures.

2.1.5. Controlled Radical Polymerization

Controlled radical polymerization (CRP), also known as reversible-deactivation radical polymerization (RDRP), is a technique that allows precise control over polymer architecture. CRP techniques control the polymer architecture through mechanisms that maintain a low

concentration of active radicals and establish a balance between active and inactive species [47,62]. By maintaining a low concentration of active radicals and ensuring that all chains have equal growth opportunity, CRP techniques enable precise control over polymer structure and properties. This method relies on three different mechanisms:

1. Atomic transfer radical polymerization (ATRP): ATRP achieves uniform growth of all polymer chains by using a reversible redox reaction catalyzed by a transition metal complex.
2. Nitroxide-mediated polymerization (NMP): NMP controls polymerization by reversible termination of growing chains with nitroxide radicals.
3. Reversible addition-fragmentation chain transfer (RAFT): RAFT polymerization controls molecular weight by reversibly transferring radicals between growing chains using a chain transfer agent (CTA).

However, ATRP and RAFT have been more widely applied and studied compared to NMP in recent years. RAFT polymerization has gained considerable popularity due to its versatility with different monomers and mild reaction conditions. It is of particular interest in academic research and is increasingly used in industrial applications [63]. Despite ATRP offering precise control, RAFT stands out for its metal-free nature, broader monomer compatibility and easier industrial scalability. Its simplicity and adaptability make RAFT a highly promising method for future polymer applications [63].

RAFT: $P_n\bullet + CTA\text{-}P_m$. $CTP\text{-}P_n + P_m\bullet$

ATRP: $P_n\text{-}X$ + activator $P_n\bullet$ + deactivator

RAFT polymerization enables precise control over molecular weight, polymer architecture and end-group fidelity by introducing a CTA to mediate the growth of polymer chains via a degenerative chain transfer process. As shown in Figure 6, the initial radical adds to the CTA (R– Z), forming a reactive intermediate. This intermediate fragments into a dormant macro-CTA (P_m–Z) and a new radical (R•), which starts another chain. This process ensures all CTAs become macro-CTAs.

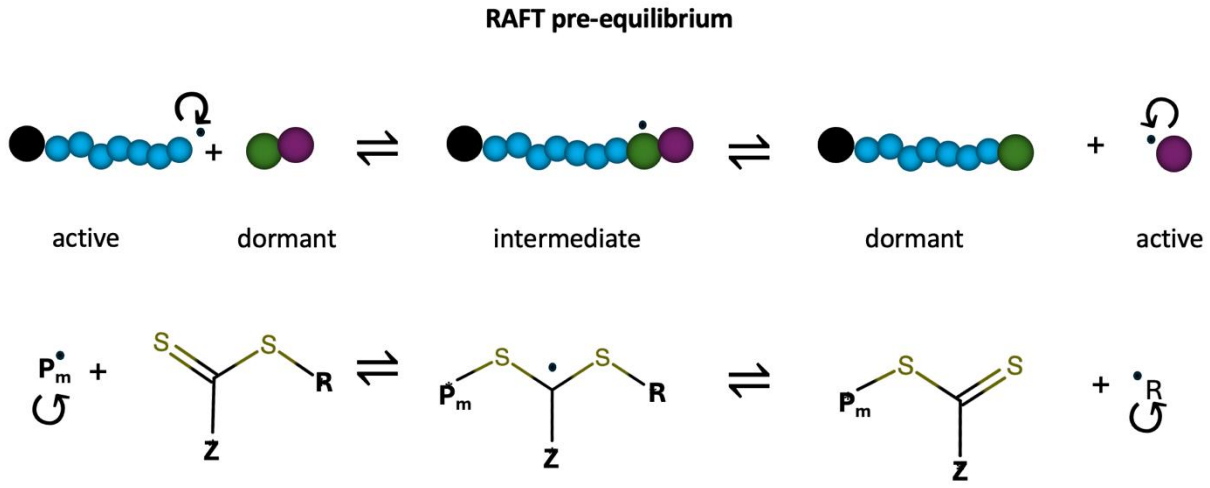

Figure 6: The mechanism of RAFT begins with a pre-equilibrium step in the degenerative chain transfer process, showing the dormant and active states of a polymer chain, P_m [63].

Once all small-molecule CTAs are consumed, equilibrium is established in the main state, between growing radicals (P_m, P_n) and dormant species as shown in Figure 7. Active chains repeatedly transfer between macro-CTAs, maintaining low radical concentration and minimizing termination. Termination via coupling or disproportionation still occurs, but at a lower frequency. The total number of dead chains correlates with the amount of free radical initiator used.

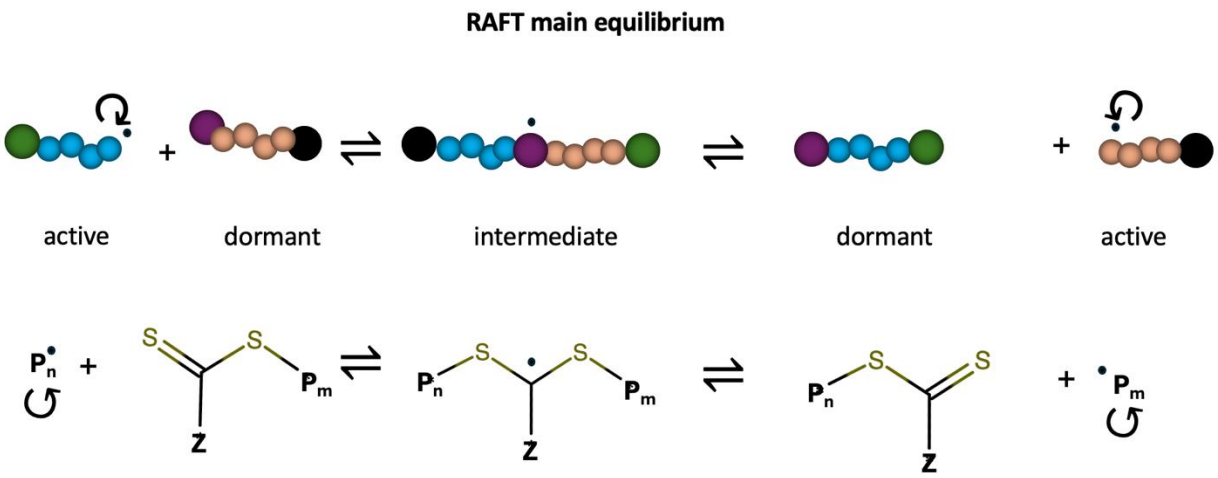

Figure 7: The RAFT main equilibrium represents the reversible addition–fragmentation chain transfer between two polymer chains, P_m and P_n [63].

Besides thermal methods, there are also: Photochemical RAFT (e.g. photoiniferter, PET-RAFT), electrochemical RAFT (eRAFT), ultrasonic or mechanical forces (sono-RAFT) [64,65]. RAFT is especially valuable when integrated into MIP sensor fabrication, where control over film thickness, binding site accessibility and polymer chain length directly influences sensor sensitivity and selectivity.

2.2. MIP Characterization Methods

Established methods to characterize MIP include optical microscopy, electron microscopy (including scanning electron microscopy and transmission electron microscopy) and atomic force microscopy for gaining a better understanding of the structure, morphology and chemical properties of MIP surfaces. In addition, these techniques can effectively monitor template removal and analyte rebinding, especially in the case of large analytes. This information is crucial for optimizing MIP performance, ensuring reproducibility and developing new applications in fields such as sensing, separation and catalysis.

2.2.1. Scanning Electron Microscopy

Scanning electron microscopy (SEM) is a powerful imaging technique to scan the sample surface. It uses a focused electron beam, providing high-resolution images of the sample´s topography and composition [66]. SEM was first developed in the 1930s–1940s and advanced significantly through work in Cambridge and industrial applications worldwide. Today, SEM is widely used for high-resolution imaging and analysis across numerous scientific and industrial fields [67,68].

SEM works by directing an electron beam with energy up to 40 keV to a sample in ultrahigh vacuum. As these primary electrons interact with the sample, they produce a variety of signals, including secondary electrons, backscattered electrons and characteristic X-rays. Secondary electrons emitted from 5 to 10 nm below the sample surface are mostly used for imaging and provide detailed topographical information. Backscattered electrons, which are produced deeper in the sample, can distinguish regions of different chemical composition. X-rays emitted during the process can be analyzed for elemental composition using techniques such as energy-dispersive X-ray spectroscopy (EDX) [69].

The capabilities of SEM go beyond “just” imaging. It is suitable for providing information about sample structure, orientation and elemental composition. This technique is widely used to characterize the surface of materials, including MIPs.

However, SEM has its limitations. Samples must be electrically conductive and often require depositing a thin conductive coating on top of non-conductive materials. This coating process may be detrimental to some samples, especially in MIP applications. In addition, the high vacuum environment required for SEM operation may not be suitable for all sample types. Despite these challenges, SEM remains a vital tool in materials science, providing unparalleled insights into the microscopic world of surface structures and compositions.

2.2.2. Atomic Force Microscopy

Atomic force microscopy (AFM) is a powerful imaging technique that yields high-resolution surface information of the three-dimensional topography of a sample surface by measuring interaction between a fine tip and the surface being examined. As shown in Figure 8, in principle, a tip mounted on a flexible cantilever approaches the sample surface. The instrument maintains a constant force between the tip and surface through a vertical piezoelectric scanner by adjusting z-direction movement [70]. Tip-surface interaction forces are typically detected using an optical lever system, where the laser beam reflects off the cantilever onto a position-sensitive detector to measure small cantilever displacement. AFM can function in various modes, including contact, non-contact and tapping.

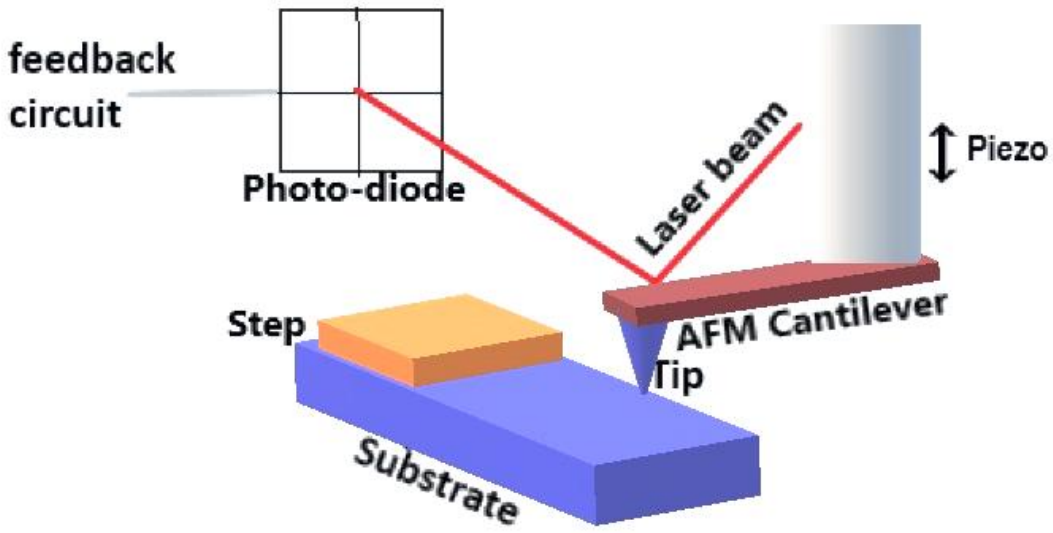

Figure 8: The AFM setup shows a cantilever with a sharp tip scanning the sample surface with nanometer-scale measurement of surface topography.

When the tip approaches the sample surface, various forces occur between them, such as Van der Waals forces, electrostatic forces, or even chemical binding. As the tip interacts with the sample, forces between the tip and sample cause deflections of the cantilever. Figure 9 shows the relationship between tip-surface distance and tip-surface force, which is related to the different operating modes. At the right-hand part of the graph (tip far from surface), the force is close to zero. This region typically is not used for imaging in AFM. In the attractive interaction area, the tip moves closer to the surface primarily due to Van der Waals forces. The tip oscillates above the surface without making contact and maps the surface only by weak attractive forces (non-contact mode). Repulsive interaction by overlapping electron orbitals between atoms in the tip and sample, makes the tip get very close to or contact the surface (contact-mode) [71]. In contact-mode the tip experiences repulsive forces while scanning, as it is in direct contact with the surface. In tapping mode, the tip ''taps'' the surface and, hence, oscillates between the attractive and repulsive area with each oscillation cycle.

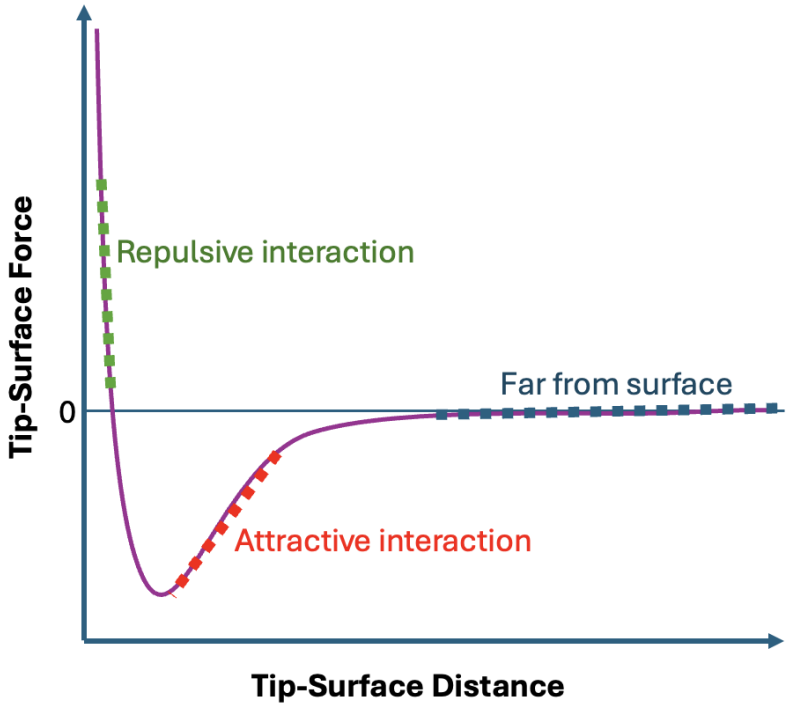

Figure 9: Force-distance curve that describes the attractive and repulsive interactions between the tip and the sample surface depending on their distance.

Tapping mode, also known as intermittent contact mode, represents a balanced approach between contact and non-contact AFM techniques. It enables consistent imaging across a wide range of materials, reducing the risk of surface damage while providing sensitivity to mechanical properties such as elasticity and contrast. However, this method may involve a minor reduction in spatial resolution and demands more advanced operational control compared to contact mode [72,73].

Non-contact mode, where the tip remains at a fixed distance and interacts only through Van der Waals forces, is especially useful for imaging extremely fragile samples. It provides high sensitivity to surface forces but typically results in lower lateral resolution and may be more sensitive to environmental influences such as humidity or temperature. Ultimately, the choice of scanning mode depends on the sample characteristics, the level of resolution required and the specific type of surface information being sought [74].

2.2.3. Dynamic Light Scattering

Dynamic light scattering (DLS) measures the diameters and size distribution of particles in solution. DLS is widely used in various fields, including nanoparticle characterization, polymer size analysis [75] and protein aggregation [76,77] studies. The technique is primarily based on the Brownian motion of particles in solution and on how they scatter light.

Brownian motion refers to the random, erratic movement of particles suspended in a fluid (liquid or gas) [78,79], resulting from their collision with fast-moving atoms or molecules in the fluid. The particle movement is characterized by four key aspects:

- Random: The movement has no preferred direction.
- Continuous: It never stops if the temperature is above absolute zero.
- Independent: Each particle moves independently of others.

- Scale-dependent: More noticeable for smaller particles and at smaller scales.

Understanding Brownian motion is critical to interpreting DLS results, as the technique relies on measuring the speed of this motion to determine particle size. The faster the Brownian motion, the smaller the particle, which is reflected in more rapid fluctuations of the scattered light intensity in DLS measurements.

Figure 10 shows a DLS measurement set-up: a laser beam is directed at the sample and the particles scatter the incident light in all directions. A detector, typically positioned at a specific angle (often 90° or 173°), measures the intensity of the scattered light over time. Due to Brownian motion, the particles are constantly moving, causing fluctuations in the scattered light intensity. The system uses a digital correlator to measure the rate of these intensity fluctuations, generating a correlation function. This function is analyzed to determine the diffusion coefficients of the particles. Finally, using the Stokes-Einstein equation, the hydrodynamic diameter of the particles is calculated from the diffusion coefficient. This hydrodynamic diameter includes the core particle size plus any coating or hydration layer.

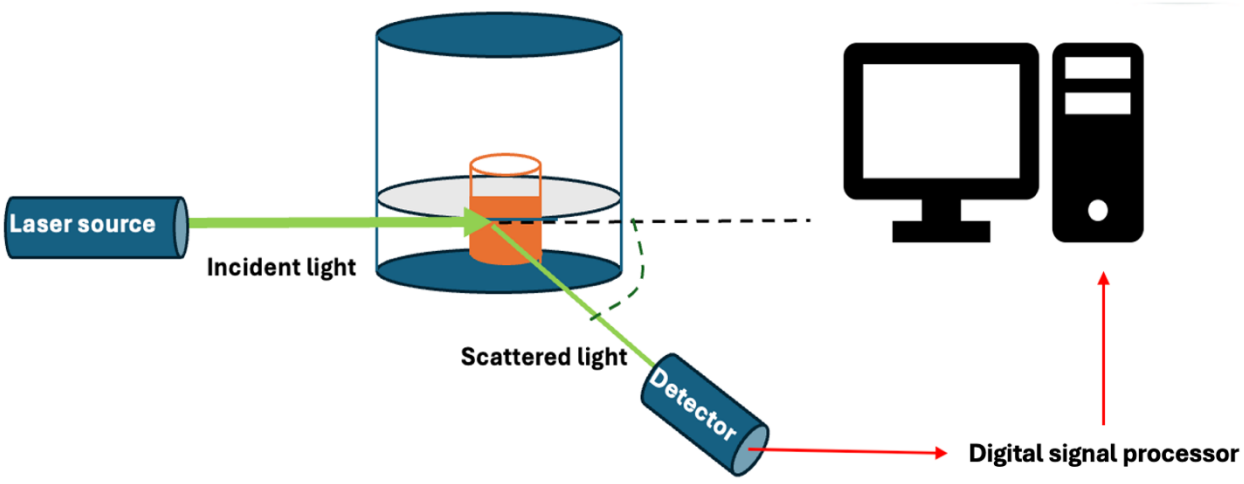

Figure 10: Typical setup of a DLS measurement.

2.2.4. Zeta Potential

Zeta potential is a key concept in understanding the behavior of particles or surfaces immersed in a liquid medium. When a charged surface is in contact with an electrolyte solution, it attracts oppositely charged ions from the uniform distribution of anions and cations. Anions will be attracted toward a positively charged particle, leading to a higher concentration of anions near the surface. Similarly, repulsion of cations will result in a lower concentration of cations near the surface. The shear (slipping) plane is a transition point between the rigid layer associated with the particle surface (which includes tightly bound material) and the free liquid. The region from the particle surface to the shear plane is known as the electrical double layer (EDL).

Figure 11 shows EDL consisting of two parts: the stern layer (the immobile layer closest to the surface) and the diffuse layer (where ions are more mobile but still influenced by the surface charge).

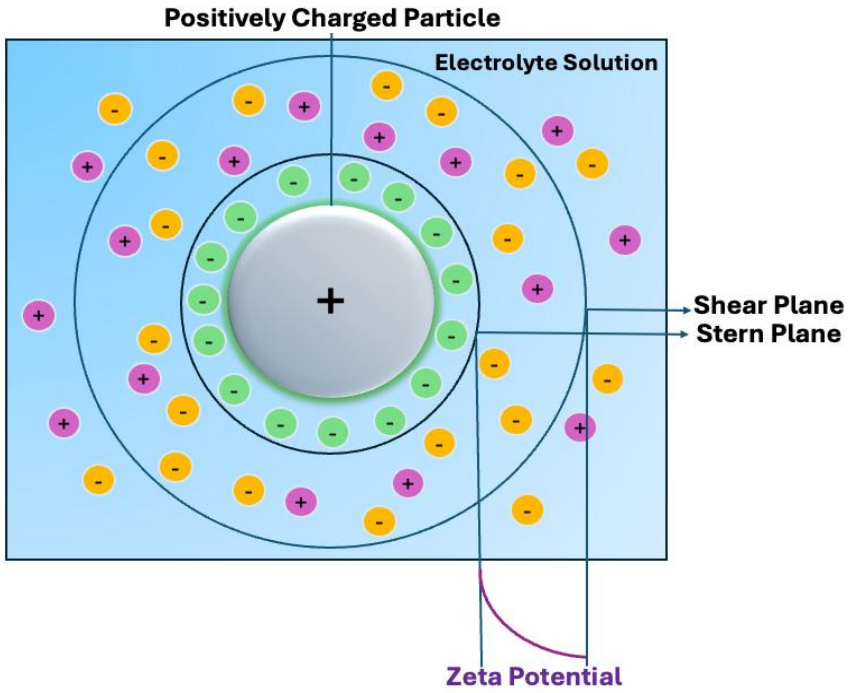

Figure 11: The concept of zeta potential in a colloidal system. The electrical potential at the shear plane. It reflects the net electrical potential at the point where the particle stops dragging liquid along with it.

The zeta potential is defined as the electric potential at this shear plane relative to the bulk of the solution. It is a crucial parameter for understanding the stability of colloidal systems and the behavior of particles in solution. To determine particle size alongside charge, electrophoretic light scattering is often coupled with DLS [80]. For solid surfaces, zeta potential is commonly measured through streaming potential or streaming current methods. When a liquid flows through a narrow capillary, it drags ions from EDL, generating a net charge movement. This charge displacement results in a measurable streaming potential or current, from which one can calculate the zeta potential of the surface [81].

2.3. Chemosensors

A chemical sensor consists of three main parts: a sensitive layer (receiver), a transducer and a data processing unit. The sensing layer selectively responds to the target analyte while avoiding interactions with undesired compounds. Biosensors typically employ biological recognition elements such as enzyme-substrate binding [82], ligand binding [83] and immunological interactions [84]. Synthetic receptors, such as MIPs, are an alternative option to overcome the limitations of chemical, thermal and mechanical stability compared to biological receptors. A transducer is a device that converts a chemical response into an electrical signal. Different types of transducers are used in chemical sensing, which are classified based on the principles of signal processing as shown in Figure 12 [85,86].

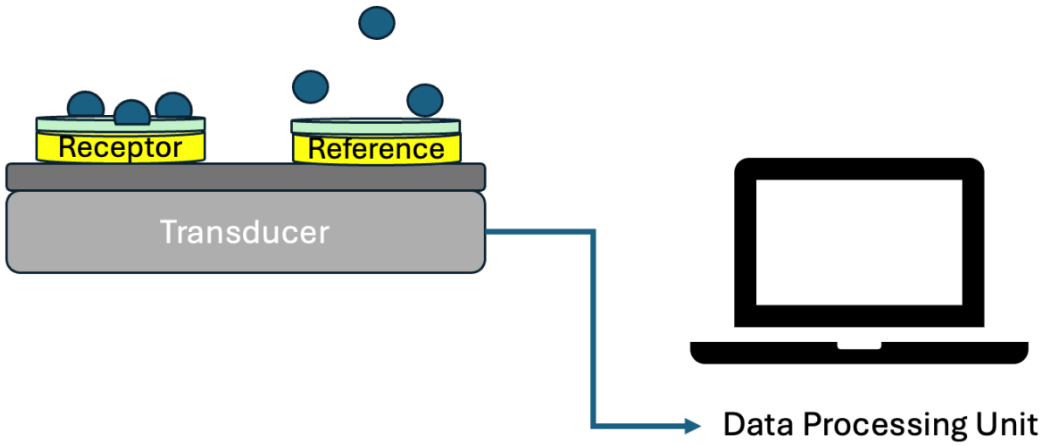

Figure 12: Schematic of a chemical sensor setup showing the receptor and corresponding reference in contact with the analyte, a transducer and a computer as the data processor.

Among the various transducers, piezoelectric devices have gained significant attention due to their high sensitivity. One of the most prominent examples is the quartz crystal microbalance (QCM), a piezoelectric mass sensor that measures changes in mass through shifts in the resonant frequency of a quartz crystal.

2.3.1. Quartz Crystal Microbalance

Quartz crystal microbalance (QCM) is a piezoelectric mass sensor that measures changes in mass through shifts in the resonant frequency of a quartz crystal [87]. A combination of QCM and MIPs produces mass-sensitive sensors that operate based on changes in the mass loaded onto the receptor layer [88,89].

Typically, QCMs are fabricated from AT-cut α-quartz, where the crystal is sliced at a specific angle (35.25° to the Z-axis) to ensure temperature stability and optimal performance in thickness shear mode (TSM) [90]. When an alternating voltage is applied across electrodes on opposite surfaces of the crystal, it induces oscillations at a resonant frequency determined by the crystal's thickness. Thinner crystals oscillate at higher frequencies, resulting in higher sensitivity [91]. However, this also makes them more fragile and mechanically less stable. QCM measurements rely on the inverse piezoelectric effect. An alternating voltage applied across both the sensing and electrode sides of the crystal initiates oscillations. Upon mass loading (e.g., analyte binding), these oscillations change, leading to a measurable shift in frequency as shown in Figure 13.

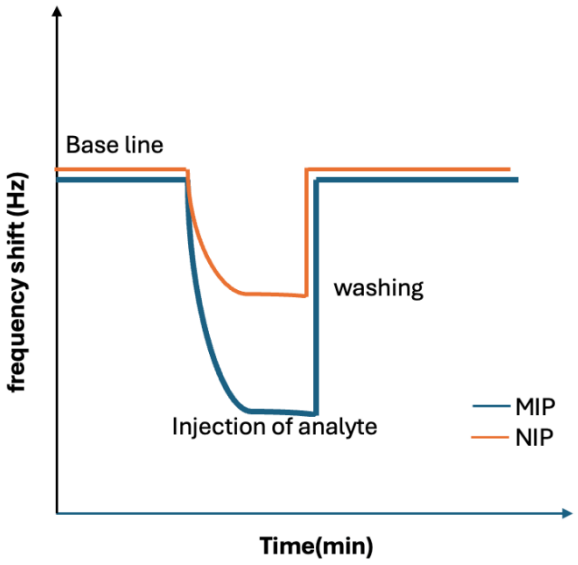

Figure 13: Principle of QCM measurement in a dual-electrode system, showing the responses of the receptor layer (MIP) and the reference layer (NIP).

The orange graph represents the non-imprinted polymer (NIP), which is measured as a reference. The observed frequency shift can be attributed to non-specific interactions between the NIP and the target analyte. In contrast, the blue graph represents the molecularly imprinted polymer (MIP), which selectively interacts with the target molecule. This frequency shift can be correlated to the change in mass using the Sauerbrey equation, which forms the basis of QCM mass sensing [92].

$$\Delta f = \left(\frac{-2f_0^2}{A\sqrt{\mu_q \rho_q}}\right)\Delta m = -C_f \Delta m$$

Δf: Frequency change (Hz) ,f_0: Fundamental frequency of the resonator (Hz), A: Active electrode area (cm^2), μ: Density of quartz (2.643 g cm^{-3}), ρ: Shear modulus of quartz (2.947 x1011 g cm^{-1} s^{-2}), Δm: Mass change, C_f: Sauerbrey constant.

It is important to consider that the Sauerbrey equation holds true only when measurements are conducted in air, where the mass layer is rigid, thin and uniformly distributed [93]. Under these ideal conditions, the deposited film behaves like a true mechanical extension of the quartz crystal, oscillating synchronously with it. This results in a direct and linear relationship between the frequency shift and the mass of the adsorbed analyte. However, in liquid environments, the situation becomes more complex. The viscous damping introduced by the surrounding fluid affects both the oscillation of the quartz and the behavior of the polymer layer [94], potentially leading to non-ideal effects such as the Anti-Sauerbrey effect, where a positive frequency shift is observed after mass loading. This may occur due to non-parallel oscillation between the quartz and the attached layer, or when analyte molecules do not fully incorporate into the receptor cavities and instead remain loosely bound or accumulate on the surface. In such cases, models like the Kanazawa-Gordon equation are necessary [95], as they account for the density and viscosity of the liquid, as well as the viscoelastic properties of the sensing layer [96].

2.3.2. Cyclic Voltammetry

Cyclic voltammetry (CV) is one of the most widely used electrochemical techniques for investigating redox (oxidation–reduction) behavior [97,98]. It is particularly effective for studying the binding interactions of MIPs with specific analytes and for evaluating the rebinding process between the MIP and the target molecule [99,100]. Due to their high selectivity and sensitivity [101], MIPs have been widely applied in electrochemical sensors [102,103].

A typical CV experiment involves a three-electrode system, as shown in Figure 14, consisting of:

- Working electrode (WE), where the redox reaction of the analyte or redox probe occurs
- Reference electrode (RE), which maintains a stable reference potential (e.g., Ag/AgCl or saturated calomel electrode)
- Counter electrode (CE), which completes the circuit by allowing current to flow

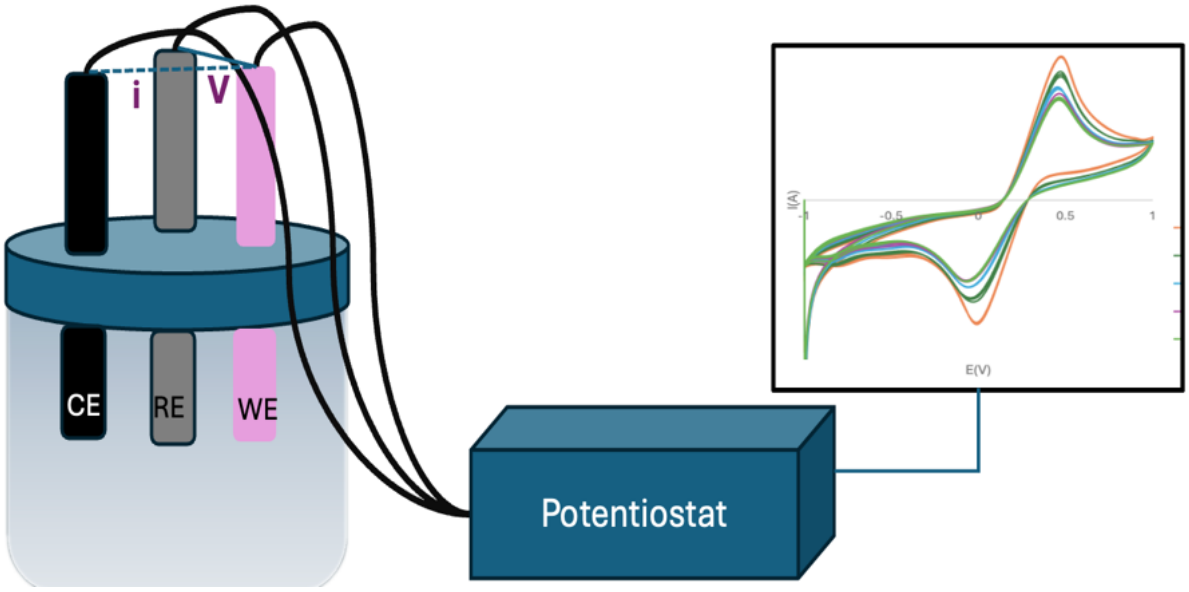

Figure 14: Experimental setup for CV: The WE, RE and CE are immersed in an electrochemical cell containing the electrolyte solution. The entire system is connected to a potentiostat, which controls the applied potential and measures the current response. The data is then recorded and analyzed using appropriate software.

This system is connected to a potentiostat, which controls the potential applied to the WE relative to the RE and measures the resulting current between the WE and CE. To evaluate the rebinding process, a thin film of the MIP is coated onto the WE. When the modified electrode is immersed in a solution containing the target analyte, specific rebinding into the MIP's imprinted cavities occurs.

This selective binding can block or hinder the charge transfer between a redox-active species in solution (e.g. ferri/ferrocyanide) and the electrode surface [104]. During the cyclic scan of potential, this results in a reduction in peak current, indicating restricted electron transfer. The greater the amount of analyte bound, the more pronounced the current suppression, providing a quantitative measure of binding strength and specificity.

A NIP with lack of specific binding sites can be used as a reference. Therefore, less or no current change should be observed upon analyte exposure, and this confirms the selectivity of the MIP layer.

3. Chemicals and Methods

3.1. Chemicals, Material and Devices

Table 1: Chemicals and materials utilized in this thesis.

Chemical	Abbreviation	Supplier	Purity (%)
1-dodecanethiol	-	Sigma-Aldrich	98
1-ethyl-3-(3-dimethylaminopropyl) carbodiimide	EDC	Merck	
11-mercaptho-1-undecanol	MUD	Sigma-Aldrich	97
16-mercaptohexadecanoic acid	MHDA	Merck	98
2,2'-Azobis(2-amidinopropane) dihydrochloride	AAPH	Sigma-Aldrich	97
2,2’-Azobis(2-methylpropionitrile)	AIBN	Sigma-Aldrich	98
4-Cyano-4-(thiobenzoylthio)pentanoic acid	CPA	Merck	<= 100
Acetic acid	AcOH	Merck	100
Acrylic acid	AA	Merck	-
Amoxicillin sodium	Amo Na	Sandoz	-
Argon 5.0	Ar	Messer	≥ 99.99
Dimethyl sulfoxide	DMSO	VWR	<= 100
Ethanol	EtOH	VWR	absolute for analysis
Ethylene glycol dimethacrylate (stabilized)	EGDMA	Sigma-Aldrich	98%
Hydrochloric acid 37%	HCl	Merck	for analysis
Methacrylic acid (stabilized with hydroquinone momomethyl ether)	MAA	Sigma-Aldrich	-
Methanol	MeOH	Merck	-
N-hydroxysuccinimide	NHS	Merck	98
Penicillin G potassium	Pen GK	Sandoz	
Penicillin V potassium	Pen VK	Sandoz	

Potassium chloride	KCl	VWR Chemicals	for analysis
Potassium hydroxide	KOH	Merck	for analysis
Potassium nitride	KNO3	Merck	for analysis
Potassium phosphate dibasic	K2HPO4	Sigma-Aldrich	≥ 98
Potassium phosphate monobasic	KH2PO4	Sigma-Aldrich	≥ 99
Pyridine			
Sodium dodecyl sulfate	SDS	Chemsolute	98
Sodium hydroxide	NaOH	Merck	for analysis
Toluene	Toluene	Sigma-Aldrich	≥ 99.7
Trimethylolpropane trimethacrylate	TRIM	Sigma-Aldrich	
Urea; CH4N2O		Sigma-Aldrich	

Preparation of Phosphate-Buffered Saline (PBS)

To prepare 1 liter PBS (10 mM, pH 7.4), the chemicals (Table 2) were dissolved in 800 mL of distilled water (dH_2O). The pH of the buffer was verified using a pH meter and, if necessary, adjusted with HCl or NaOH. Finally, dH_2O was added to bring the total volume to 1 liter.

Table 2: Chemicals for preparing PBS

Chemicals	Amount (g)	Concentration (M)
NaCl	8	0.137
KCl	0.2	0.0027
$Na_2HPO_4.2H_2O$	1.76	0.01
$NaH_2PO_4.2H_2O$	0.277	0.0018

Table 3: Instruments used

Instrument	Model	Manufacturer
Atomic Force Microscopy (AFM)	Bruker MultiMode VIII with ScanAsyst and Peak Force QNM expansion	Bruker
Balance	Entris	Sartorius Entris
Balance	BP210S	Sartorius Entris
Balance	BP2100	Sartorius Entris
Centrifuge	Centrifuge 5702	Eppendorf
Dynamic Light Scattering (DLS)	Zetasiser ZS ZEN-3600 Nanophox	Malvern Instrument Ltd.
FBAR	Film Bulk Acoustic Resonators	Biomensio Ltd
FTIR	Spectrum 100	Perkin Elmer
Frequency Counter	53131A 225 MHz Universal Counter	Agilent
Light Microscope	Eclipse LV100	Nikon
Network Analyzer	E5062A (300 kHz – 3 GHz)	Agilent
Physical Vapor Deposition (PVD)	75 PRO Line	Kurt J. Lesker
Plasma Cleaner	Zepto One	Diener electronic
Power Supply	EA-PS 2032-025	EA Elektro-Automatik
Scanning Light Microscope (SEM)	55 VP	Zeiss Supra
Spin Coater	Spin Coat G3P-8	Specialty Coating Systems
UV Lamp	VL-215LM	Vilber
Ultrasonic Bath	Elmasonic S120	Elma Schmidbauer GmbH
Vortex Mixer	REAX 2000	Heidolph
pH-meter	713 pH-meter	Metrohm

3.1.1. Custom Sensor Electrodes Manufacturing Methods

AT-cut quartz disks as the blank QCM chips, with a fundamental frequency of 10 MHz in a thickness of 168 µm and a diameter of 13.8 mm were purchased from Roditi International Corporation Ltd, UK. Figure 15 shows a dual electrode system on the connection side to the oscillator circuit. In the first step, the bottom side of QCM was screen printed two electrodes (4 mm diameter with a distance of 1 mm in-between of electrodes) using bright gold paste (GGP 1229 DH, Heraeus) and silk-screen stencils template as will be discussed in section 3.1.2.

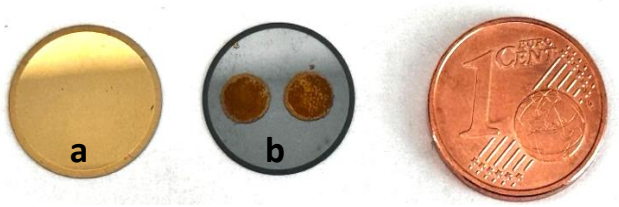

Figure 15: QCM coated with a fully metallised and duel electrodes system. Both are shown next to a 1 cent coin for size comparison.

3.1.2. Electrode Screen Printing

Two electrodes were silk-screen printed onto the surface of blank quartz discs using gold paste. Figure 16 shows the silk-screen stencils used for printing the gold. To do this, the quartz plates were secured in place using a vacuum pump. Then, the gold paste was spread across the surface with a rubber squeegee. Afterward, the screen-printed quartz discs were placed in an oven at 400°C for 4 hours to completely harden the paste and remove organic components. Once cooled, the discs were ready for the next step: fully metallizing the sample side via physical vapor deposition (PVD).

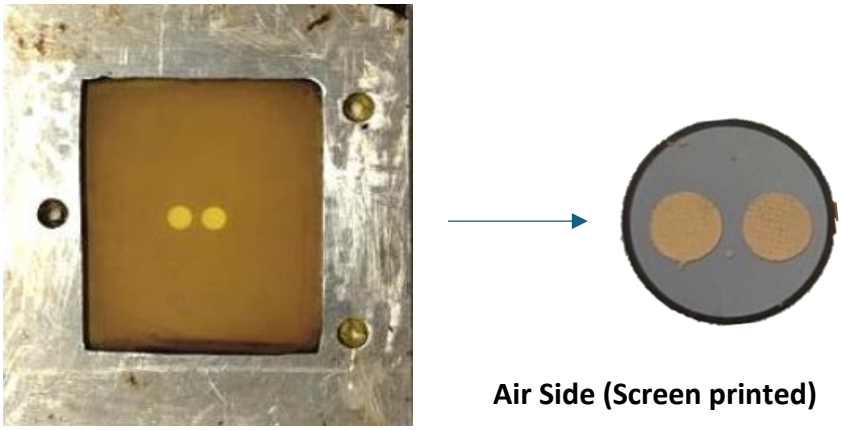

Figure 16: The left-hand side of the image represents homemade silk-screen stencil using for electrode screen printing and right-hand side is the printed electrodes on the QCM.

3.1.3. Physical Vapor Deposition

The opposite side of the disk was fully metallized using a Kurt J. Lesker PVD 75 system, a high-performance physical vapor deposition (PVD) unit designed for thin film coating applications (Figure 17). This system operates under high vacuum conditions and is widely used for sputtering or evaporation-based depositions of metallic, dielectric, or composite films. This machine is equipped with three sources: two for sputtering and one for thermal evaporation.

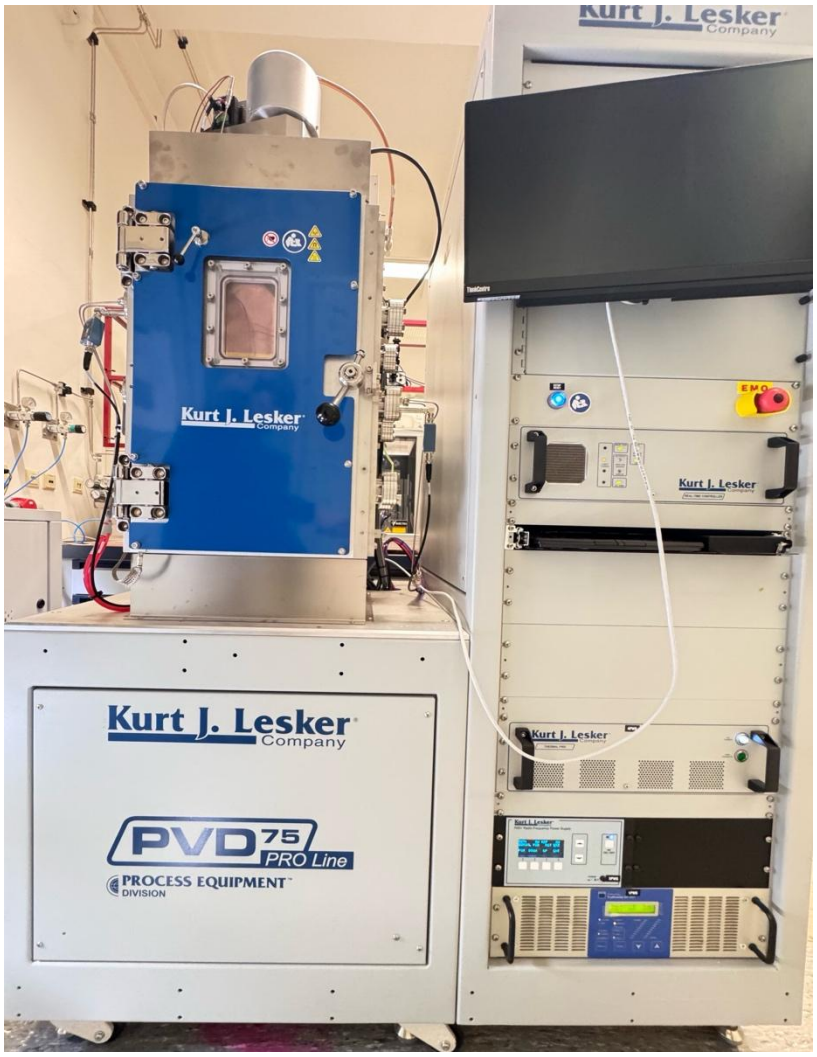

Figure 17: Physical Vapor Deposition (PVD) System – Kurt J. Lesker PVD 75 PRO Line. The system consists of a vacuum chamber (left side, blue panel) where substrates are loaded and film deposition takes place. The chamber is equipped with safety interlocks, a viewing window and gas inlet/outlet ports for precise control of deposition conditions. A variety of substrate holders and target mounts can be configured depending on the deposition method (DC, RF, or thermal evaporation).

First, a 30 nm chromium interlayer was deposited by sputtering (using the EJTCRXX352TK4 target from Kurt J. Lesker). Next, a 50 nm gold layer was deposited via thermal evaporation to minimize material waste. The PVD chamber operates at pressures ranging from 10^{-3} to 10^{-7} Torr and heats

substrates up to 350°C. During deposition, the substrate holder rotates at up to 20 rpm to ensure uniform film coverage; exceeding this speed can lead to an uneven layer. After deposition, the QCM chips were annealed at 200°C for 2 hours to stabilize the chromium and gold layers and resulted final QCM chip as shown in Figure 18. Finally, the QCM chips were cleaned with EtOH and then plasma-cleaned (Zepto One, Diener) at a pressure of 1.3×10^{-3} mbar and 5.5 W power for 15 minutes, immediately before use.

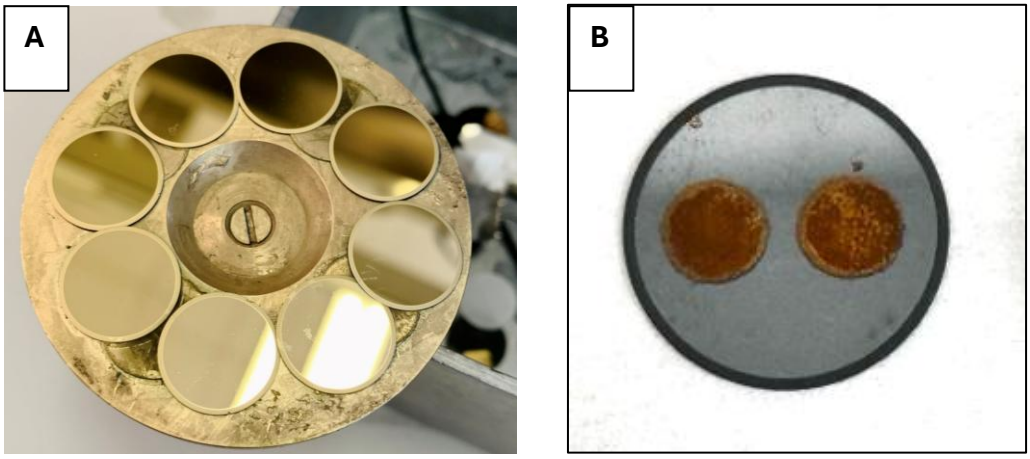

Figure 18: (A) QCM disk with a fully metallized gold surface using PVD and (B) the bottom side of the quartz disk.

3.1.4. QCM Measuring Cell

Figure 19 illustrates the measuring cell, which consists of a two-part body, each part measuring 5 × 5 cm, constructed from polymethyl methacrylate (PMMA). The QCM holder is made of PDMS (polydimethylsiloxane) and comprises two sections: a lower part that accommodates the electrodes and an upper lid that contacts the top surface of the QCM. During measurements, the QCM is securely clamped between these two sections.

To ensure that only the polymer-coated area is exposed to the liquid phase, the rest of the QCM surface is isolated from the measuring solution. This configuration enables selective interaction between the analyte and the polymer layers, namely the MIP and NIP.

The sample chamber holds approximately 200 µL and is designed to contain both MIP and NIP compartments. Once the QCM is positioned inside the chamber, the entire setup is fastened using screws on all four corners for stability. Each electrode is individually connected to separate channels on the oscillator circuit, enabling independent monitoring of frequency shifts for both the MIP and NIP layers.

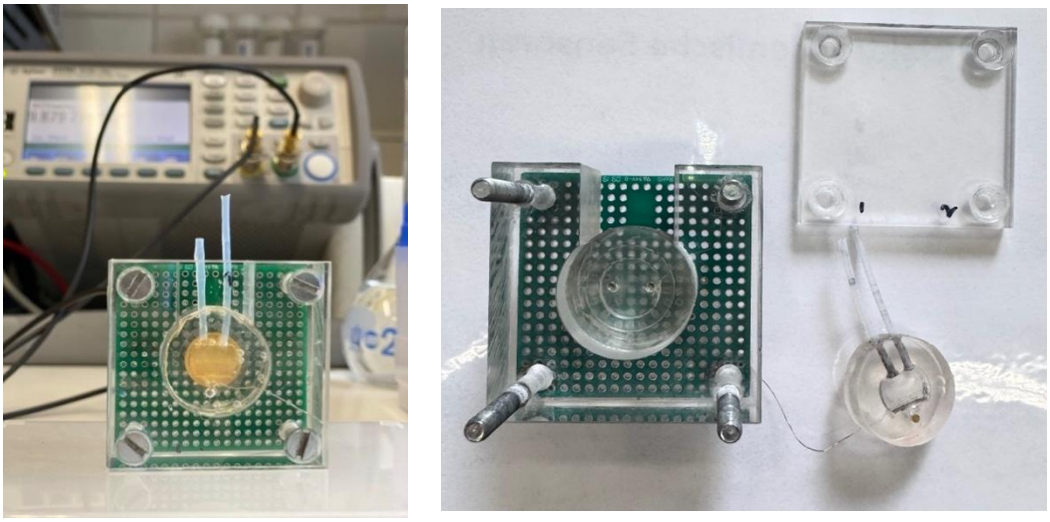

Figure 19: Close QCM measurement cell (left) and open cell (right).

3.1.5. QCM Measurements

The QCM measurement setup, as shown in Figure 20, consists of a homemade measuring cell and an oscillator circuit containing two individual printed circuit boards for dual electrode connection. A laboratory power supply (EA-PS 2032-025, EA Elektro-Automatik) and a frequency counter (Universal Counter 53131A, 225 MHz, Agilent Technologies) were used to operate the oscillators and to read out the frequencies of the two channels as a function of time, respectively. The power supply was set to 15 V during the measurements.

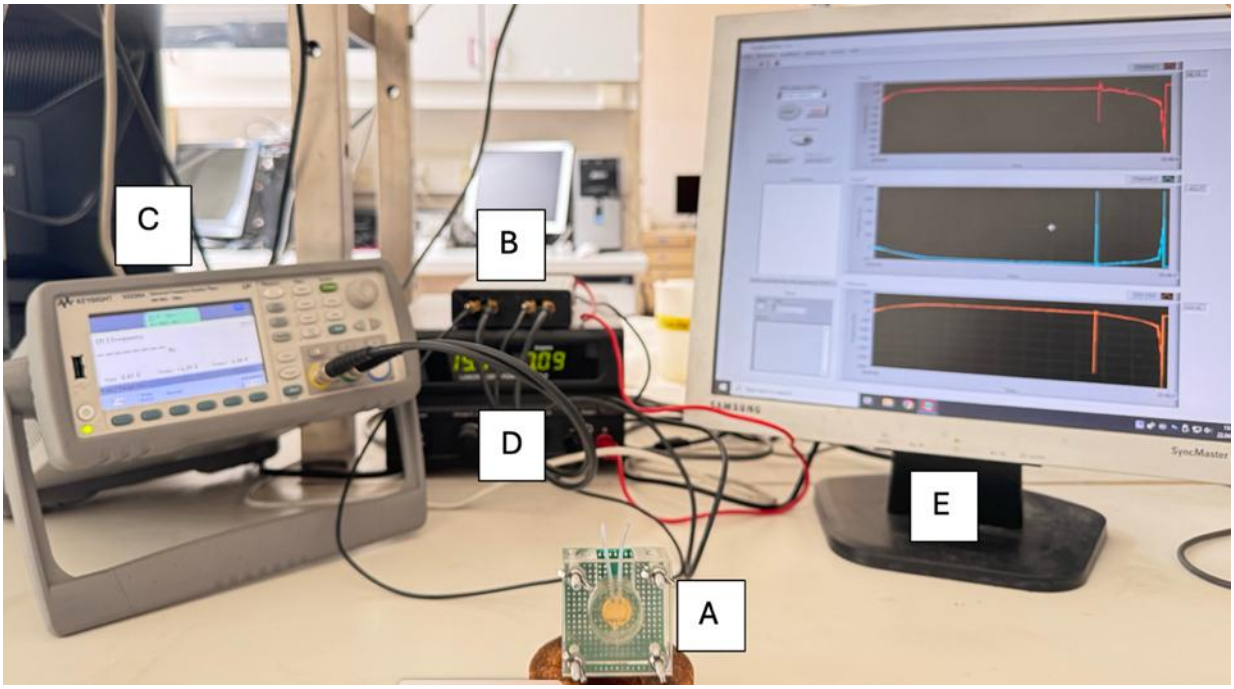

Figure 20: QCM measurement setup, (A) Measuring cell, (B) Oscillator circuit, (C) Frequency counter, (D) Power supplier, (E) Computer.

After placing the QCM in the flow cell, the damping and resonance frequencies in air and after filling with the background solution were measured using a network analyzer (E5062A ENA Series, 300 kHz – 3 GHz, Agilent Technologies). Only QCMs with damping values above -10 dB in air were used for the measurements.

Before starting the measurement, the QCM stabilized to a baseline frequency by adding 400 µL background solution before introducing the analyte. The measurement flow cell was positioned vertically throughout the entire process and both injections and washing steps were performed manually and continuously without any stops or pauses. After each analyte injection, the QCM was washed with 1 mL of background solution to return the frequency to its baseline. The data were recorded in real time using a LabVIEW-based routine, which read out the data from the frequency counter and generated CSV files. These files were subsequently processed and graphed using Microsoft Excel.

3.1.6. FBAR Measurements

In addition to QCM measurements, film bulk acoustic resonators (FBAR) were also employed to enhance the accuracy of Pen V detection using Pen V MIP and NIP NPs. The FBAR was provided by Biomensio Ltd, a partner of the AquaNose project. Both QCM and FBAR operate on the principle of detecting mass changes via resonance frequency shifts and require surface functionalization for selective analyte binding [105].

The FBAR chip used in this study consists of 64 individual resonators arranged in a 4 × 16 array, with each pixel measuring 200 µm × 200 µm on a chip smaller than 1 cm² as shown in Figure 21. Each pixel contains an integrated read-out circuit composed of an interface block, a voltage-controlled oscillator (VCO), a local control unit and a frequency meter (digital counter). The main control system determines the voltage applied to each VCO, which in turn sets the oscillation frequency. The frequency counter then monitors this frequency. Frequency changes reflect the binding of molecules to the FBAR surface [106].

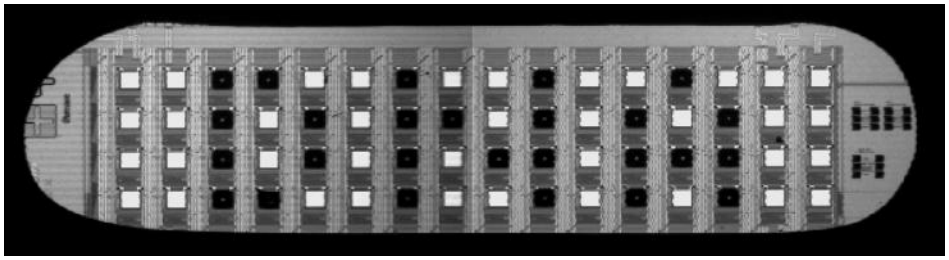

Figure 21: The FBAR array chip consisting of 64 pixels with some of the pixels functionalized [106].

Figure 22 shows the FBAR sensor surface after nanoparticle coating. For preparation, 3 µL of MIP NPs were pipetted directly onto 32 pixels (half of the chip) and spin-coated at 750 rpm for 10 seconds. The remaining 32 pixels were coated with the corresponding NIP NPs using the same procedure. The chips were then dried overnight in a desiccator, washed with stirring in dH_2O for 1 hour and dried again in the desiccator prior to measurement.

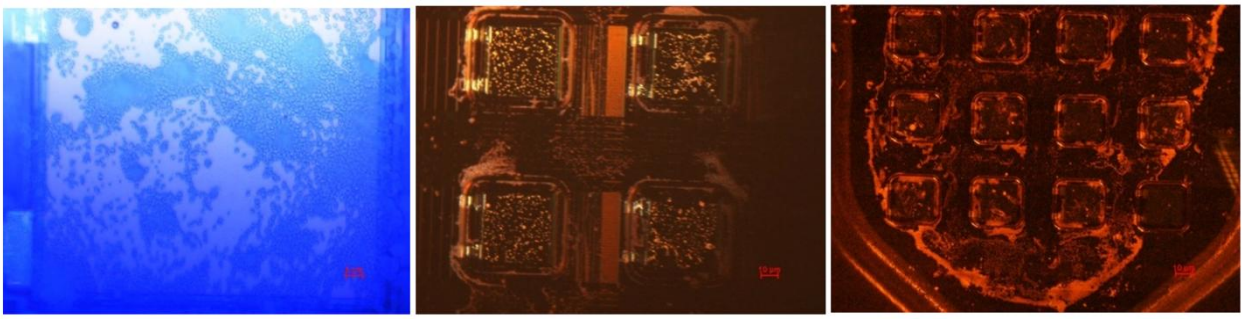

Figure 22: Optical microscopy images of FBAR pixels coated with MIP NPs: 1, 4 and 12 pixels shown respectively.

As shown in Figure 23, the FBAR chip was placed in the measurement setup and the output was recorded via a connected PC. FBAR measurements were initiated by recording a stable baseline for at least 5 minutes. This was followed by sample injection with an interaction time of 1 minute. After each measurement, the pixels were washed with dH_2O to wash out the analyte and restore baseline conditions.

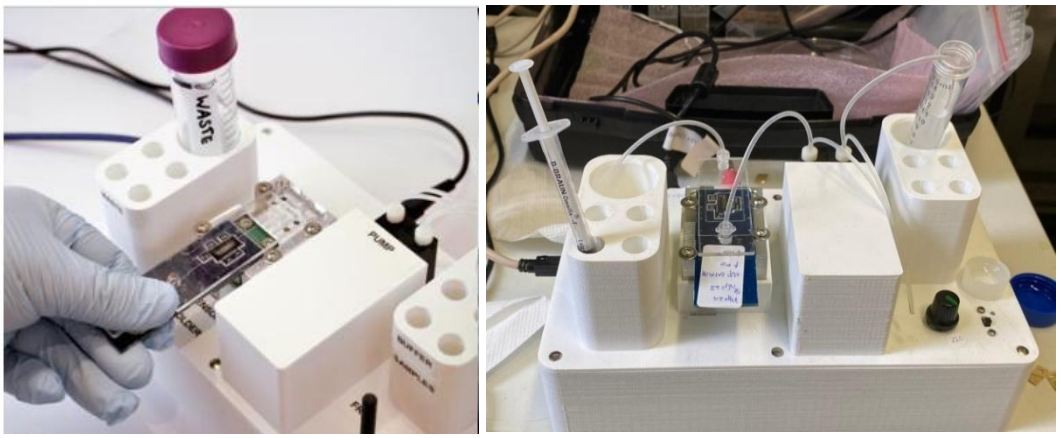

Figure 23: Full FBAR measurement setup.

3.2. Materials Characterization

3.2.1. Scanning Electron Microscopy

Scanning electron microscopy (SEM) was used to assess the morphology and structure of both MIP and NIP layers for the Pen V and Au NP-based sensors. SEM imaging was performed using a 55 VP SEM system (Carl Zeiss).

For the Pen V MIP and NIP nanoparticles, samples were prepared by depositing the polymeric NPs onto 1 × 1 cm glass slides. Specifically, 5 µL of NP suspension (1000 mg/L in ethanol) was spin-coated using a PI-KEM LTD G3P-8 spin coater, with adding 2 µL of Methyl acrylate to the coating solution to enhance particle adhesion. The samples were then sputter-coated with a 5 nm gold layer using a Leica EM SCD050 sputter coater.

For the Au NP-based MIP and NIP sensors, SEM analysis was performed directly on the QCM surfaces, as the polymerization process was carried out in-situ.

3.2.2. ATR-FTIR

To confirm the conversion of Pen VK to its free acid form, Fourier-transform infrared spectroscopy with attenuated total reflection (ATR-FTIR) was performed using a Spectrum 100 spectrometer (PerkinElmer) equipped with a Golden Gate diamond ATR accessory (Specac). Spectra were recorded in the wavenumber range of 4000-600 cm^{-1}, with each spectrum representing the average of 8 consecutive scans. Solid samples were analyzed directly by pressing them onto the ATR crystal, without requiring any additional sample preparation.

3.2.3. Atomic Force Microscopy

Atomic force microscopy (AFM) measurements were performed on the Au NP-based MIP samples to evaluate the success of template imprinting, determine the height of the polymer

layer and confirm the extraction of nanoparticles from the polymer matrix. These measurements also complemented the QCM results by providing visual confirmation of rebinding efficiency and enabled visualization of the Au NP distribution within the polymer.

For this purpose, the modified QCM sensors coated with polymer were securely attached to a magnetic sample holder using double-sided adhesive tape. The measurements were conducted in both tapping and contact modes under ambient conditions using Bruker MultiMode VIII Atomic Force Microscope (AFM) equipped with ScanAsyst and PeakForce QNM (Quantitative Nanomechanical Mapping) capabilities, as show in Figure 24.

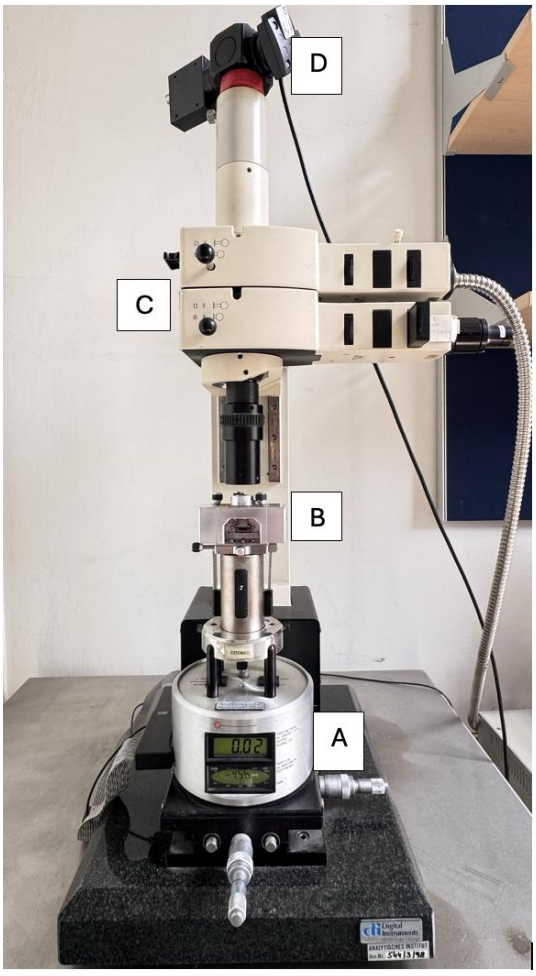

Figure 24: The AFM mounted on a vibration-isolated granite base for ultra-stable sample handling containing: (A) Laser/Detector assembly, (B) Cantilever probe holder, (C) Light microscope, (D) Camera.

The images were processed using the open-source software Gwydion. Table 4 summarizes the key parameters of the two AFM probes used.

Table 4: AFM tips and the respective measurement mode.

Mode	Tips
Tapping Mode	SNL-10 (BRUKER)
Contact Mode	TESPA-V2 (BRUKER)

3.2.4. Zeta Potentials of Particles

Zeta potentials and particle sizes of both unmodified and modified Au NPs, as well as the sizes of Pen V MIP and NIP nanoparticles, were measured using a Zetasizer Nano ZS (Malvern Panalytical). For zeta potential measurements, a Folded Capillary Zeta Cell (DTS1070, Malvern Panalytical) was used. For size measurements, a semi-micro cuvette (Lot: 230887, Th. Geyer) was employed. For size estimation of the MIP and NIP nanoparticles, a suspension with a particle concentration of 1 mg/mL was prepared in ethanol (EtOH).

3.2.5. Surface Zeta Potentials

Solid surface zeta potentials of the in-situ synthesized poly (MAA-co-TRIM) thin films were determined via measuring the streaming current (SurPASS, Anton Paar). Gold coated glass slides (20 x 10 mm) were used for the in-situ polymerization for the respective polymer thin films. For the zeta potential measurement, two coated glass slides were mounted in an adjustable gap cell. A solution of 1 mM KCl served as the background buffer; the gap distance of the cell was adjusted to 130 µm. The initial pH of the system was adjusted to 10.00 using 0.05 M KOH and then gradually decreased by titration with 0.06 M HCl. Zeta potential values were recorded after each titration step based on the measured streaming current, until a final pH of 2.00 was reached.

4. Penicillin VK Sensor

This chapter focuses on the synthesizing of MIP nanoparticles aimed at the recognition of Penicillin VK (Pen VK) using both QCM and FBAR techniques.

4.1. Experimental

Pen VK MIP and NIP NPs synthesis using precipitation polymerization, a method for producing monodisperse particles with controlled and uniform size and morphology [107]. Acrylate-based polymer NPs serve as effective MIPs due to their much higher surface-to-volume ratio than MIP thin films. In addition, polymer NPs offer excellent mechanical strength, chemical resistance and versatility in functionalization [108-110].

4.1.1. Pen VK NIP and MIP NPs

Preparation of NIP NPs

Initially, NIP NPs were synthesized by using 100 µL (1.2 mmol) MAA and 57 µL (0.3 mmol) EGDMA in 10 mL ACN, with 70 mg AIBN as the initiator. The mixture was purged with argon to remove oxygen, followed by thermal polymerization for 24 hours at 60°C. However, the resulting nanoparticles did not exhibit a regular, spherical morphology. Therefore, TRIM was used as a replacement for EGDMA. In this case, 100 µL (1.2 mmol) MAA and 100 µL (0.3 mmol) TRIM were used, along with 70 mg AIBN as the initiator. The mixture was purged with argon for 15 minutes to remove oxygen, then polymerized thermally for 24 hours at 60°C, as shown in Figure 25. The resulting nanoparticles were precipitated using a centrifuge at 3000 g for 3 hours, washed twice with 10 mL each of ACN and ethanol and then dried at 80°C overnight. The resulting nanoparticles were collected by centrifugation at 3000 g for 3 hours, washed twice with 10 mL each of ACN and ethanol and dried at 80°C overnight.

Figure 25: Polymerization solution in the oil bath: before polymerization (left) and after 24 hours of polymerization at 60°C (right).

Preparation of MIP NPs

For MIP NPs, the acrylic polymer was synthesized using MAA as the functional monomer and TRIM as the cross-linker. Pen VK salt, the commercial form of Pen V, was used as the template. Pen VK is soluble in protic solvents such as ethanol, methanol and dH_2O, but not in acetonitrile, which is the preferred solvent for precipitation polymerization. Therefore, MeOH and a binary solvent system of H_2O:ACN (1:9, v/v) were used to dissolve Pen VK in the polymerization mixture, with a total solvent volume of 10 mL.

Specifically, 50 mg of Pen VK was dissolved in 10 mL of each solvent system (MeOH and H_2O:ACN, 1:9, v/v). To this solution, 100 µL (1.2 mmol) MAA was added and stirred for 20 minutes at room temperature. Subsequently, 100 µL (0.3 mmol) TRIM was introduced as the cross-linker, followed by 70 mg AIBN as the initiator. After the mixture was purged with argon for 15 minutes it polymerized thermally at 60°C for 24 hours, as in the case of NIP NPs. The resulting MIP NPs were precipitated, washed twice with 10 mL each of ACN and ethanol and dried at 80°C overnight.

Both solvents resulted in an aggregated polymer structure rather than discrete nanoparticles, likely due to unfavorable solvation dynamics or polarity mismatches. To overcome this issue, the binary solvent system was replaced by pure acetonitrile. However, this required converting

Pen VK to Pen V free acid and making it soluble in ACN. This adjustment enabled to use a single solvent, improving polymer dispersion and nanoparticle formation.

4.1.2. Pen VK Conversion

Pen VK was converted into its free acid following a previously described method [111,112]. A total of 50 mg Pen VK was dissolved in 5 mL dH_2O and stirred with a magnetic stirrer for approximately 10 minutes until fully dissolved. Subsequently, 10 mL HCl (0.1 M) was added dropwise under continuous stirring, resulting in the crystallization and precipitation of Pen V acid. The precipitate was collected by vacuum filtration using a sintered glass filter, washed with 100 mL of deionized water and then dried in a desiccator for 3 days.

4.1.3. Pen V Free Acid MIP NPs

The MIP NPs with Pen V free acid were synthesized following the same recipe as described in section 4.1.1 by dissolving 50 mg Pen V free acid in 10 mL of ACN. The NIP NPs were prepared using the same procedure as MIP, but without adding the template. All NPs were precipitated using a centrifuge at 3000 g for 3 hours, washed twice with 10 mL each of ACN and ethanol and then dried at 80°C overnight.

MIP Size Control

To achieve nanoparticle sizes below 200 nm, as required by the project's objective of compatibility with the commercial measuring chip (section 1.1), MIP nanoparticles were synthesized using the optimized molar ratio of MAA:TRIM:Pen V (2.10:3.5:1) and 20% w/w AIBN in 40 mL ACN. In this formulation, 50 Pen V free acid (0.143 mmol) was combined with 25 µL of MAA (0.3 mmol), 150 µL TRIM (0.5 mmol) and 55 mg AIBN.

The corresponding NIP nanoparticles were prepared using the same formulation, excluding Pen V free acid.

Template Extraction

Table 5 summarizes several approaches to remove Pen V from MIP NPs.

Table 5: Extraction methods for removing Pen V from MIP nanoparticles

Solvent	Method	Time (hour)
EtOH	Soxhlet extraction	24
MeOH, 10% AcOH	Soxhlet extraction	24
EtOH	Stirring	24 or 48
AcOH:MeOH (1:9)	Stirring	24 or 48
AcOH:MeOH (2:8)	Stirring, sonication	24, then for 30 min

After evaluating all methods based on the sensing measurement results, the following procedure was selected: Pen V was extracted in the AcOH:MeOH (2:8, v/v) for 24 hours and sonicated for 30 minutes and consequently washed with dH_2O. Each time NPs were collected by centrifuge at 3000 g for 60 min.

4.1.4. Optimization of Binding Affinity of Pen V MIP NPs

Modifications to the polymer composition, involving the use of co-monomer and co-cross-linker systems, were also investigated to enhance the sensitivity and selectivity of the sensors. Different co-monomer and co-cross-linker systems were investigated to achieve optimal sensitivity and selectivity with high reproducibility [113,114]. Six different types of MIP nanoparticles and their NIP counterparts were synthesized, each incorporating varying ratios of the co-monomers MAA and AA [115-117] and the co-cross-linkers TRIM and EGDMA [118-120]. Table 6 summarizes the compositions of these particles along with their corresponding diameters. The MIP and NIP nanoparticles were prepared using the same procedure described previously in section 4.1.3.

Table 6: MIP NP and NIP NP compositions

Polymer	Monomer (µL; mmol)	Cross-linker (µL; mmol)	MIP NPs Size ± S.D (nm)	NIP NPs Size ± S.D (nm)
MIP 1	MAA (84.8; 1)	TRIM (241.6; 1)	650 ± 20	200 ± 15
MIP 2	MAA:AA (76.4:6.86; 0.9:0.1)	TRIM (241.6; 1)	600 ± 70	200 ± 40
MIP 3	MAA:AA (59.4:20.57; 0.7:0.3)	TRIM (241.6; 1)	600 ± 15	200 ± 60
MIP 4	MAA (84.8; 1)	EGDMA (188.4; 1)	700 ± 50	200 ± 45
MIP 5	MAA (84.8; 1)	TRIM:EGDMA (120:94.2; 0.5:0.5)	700 ± 10	230 ± 25

4.1.5. MIP and NIP QCM Preparation

2 mg MIP and NIP NPs were dispersed in 1 mL ethanol along with 3 µL Methyl acrylate to promote particle adhesion to the surface. The solution was then sonicated for an additional 20 minutes to improve dispersion. A 5 µL aliquot of the solution was spin-coated onto the QCM at 3000 rpm for 10 seconds. Figure 26 shows the distribution of the nanoparticles on the QCM chips. Each side of the QCM electrodes were individually coated with MIP and NIP NPs respectively.

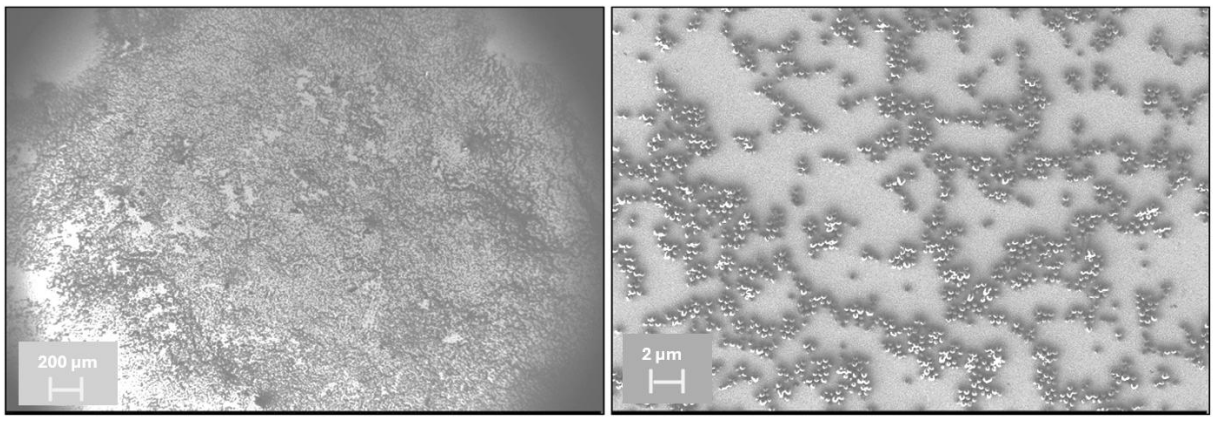

Figure 26: SEM image of coated NPs on the QCM surface (200 µm and 10 µm scale bar).

4.1.6. Cyclic Voltammetry

Cyclic voltammetry measurements were conducted on a Nova (Version 2.1.5) Metrohm Autolab B.V. (Ecochemie, Netherlands) at a scan rate of 0.05 V s^{-1}, at a potential range from -1.0 to +1.0 V vs Ag/AgCl/3M KCl (Metrohm 6.0733.100) as the reference electrode; a platinum wire served as the counter electrode. In the first step, the QCMs were prepared as described in section 4.1.5. However, the MIP and NIP were prepared separately on individual QCMs for CV measurements. The gold-coated QCMs were used as the working electrodes.

Figure 27 shows the measurement setup. The QCMs with MIP and NIP NPs were separately placed in a custom-made CV measurement cell, where they served as the respective working electrode (WE) with a 7 mL volume cap. The electrochemical cell containing the three electrodes was filled with 7 mL, 10 mM PBS (pH 7.4), 700 µL 0.05 M $K_4[Fe(CN)_6]\cdot 3H_2O$ and 700 µL 0.05 M $K_3[Fe(CN)_6]$. The Fe^{3+}/Fe^{2+} redox system in PBS at pH 7.5 served as the electrochemical indicator. Different concentrations of Pen VK (2, 3.5 and 5 mM) were tested. The CV was run for approximately 1 minute after injecting the analyte. After each measurement, the QCM was washed with PBS followed by adding fresh solution.

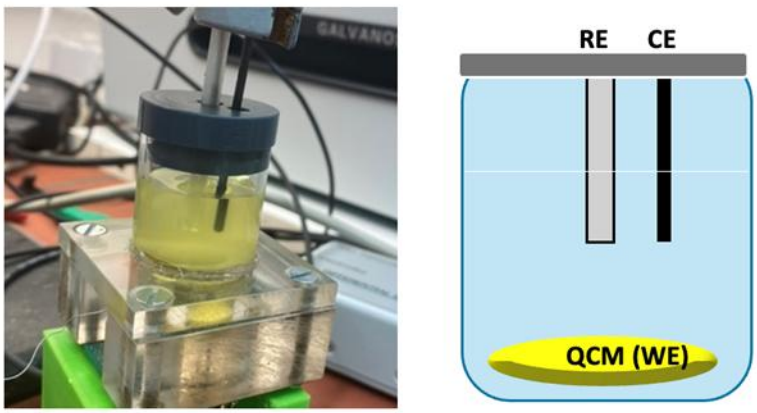

Figure 27: Photo and schematic setup of the CV experiment including working electrode (WE, QCM), reference electrode (RE) and counter electrode (CE).

4.2. Results and Discussion

This study presents a comprehensive approach to the development, characterization and validation of MIP NPs for the selective recognition of Pen VK. Through the integration of advanced synthesis techniques, surface modification and sensor validation methods, the results demonstrated the efficiency of MIP-based sensors for Pen VK detection using QCM, CV and FBAR.

4.2.1. Morphology and Size of MIP and NIP NPs

In the initial attempt, NIP nanoparticles were synthesized to identify the most suitable functional monomer and cross-linker for achieving optimal nanoparticle morphology. This was followed by the optimization of monomer, cross-linker and initiator concentrations [121,122]. Initially, MAA and EGDMA were selected as the monomer and cross-linker, respectively, with AIBN as the initiator in ACN. Figure 28 shows the chemical structures of both EGDMA and TRIM.

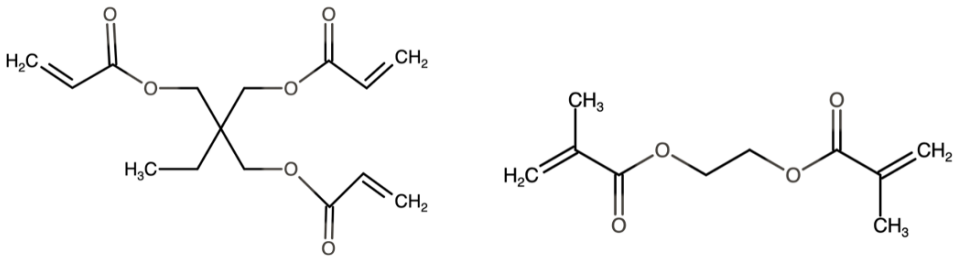

Figure 28: Chemical structures of the cross-linkers, TRIM and EGDMA.

Figure 29 shows the resulting NIP nanoparticles, which exhibit an irregular shape (see section 4.1.1).

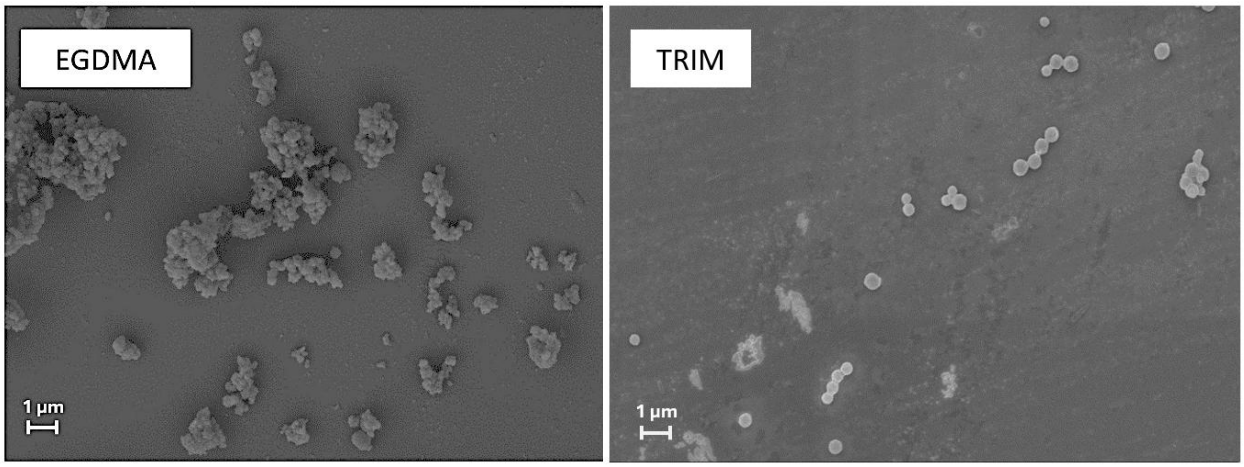

Figure 29: NIP nanoparticles synthesized with MAA:EGDMA (left) and MAA:TRIM (right).

Therefore, EGDMA was replaced by TRIM [123], a three-dimensional cross-linker known to lead to more spherical and symmetrical particles [119,124]. After obtaining the optimum formulation for uniform and homogeneous NIP NPs, MIP NPs were synthesized. As previously mentioned, MIP NPs were initially synthesized using Pen VK, as it is the commercially available form. However, Pen VK is only soluble in protic solvents, so polymerization was performed in MeOH instead of ACN. SEM images in Figure 30 show that MIPs synthesized in MeOH exhibit a clustered structure, indicating they did not form discrete NPs.

This morphology is likely due to the poor solubility of the hydrophobic polymer components in MeOH, leading to aggregation into larger structures.

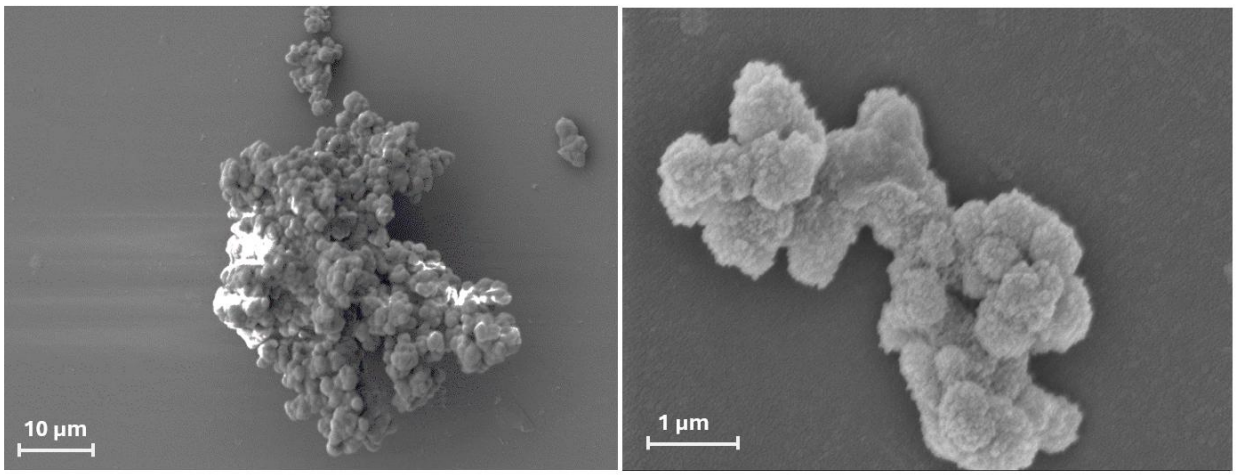

Figure 30: SEM images of MIP NPs (MAA:TRIM:PEN VK) in MeOH. The images at 10 µm and 1 µm scales reveal that the polymer particles exhibit a highly aggregated and irregular morphology. At the 1 µm scale, the surface appears rough and porous.

Figure 31 shows the resulting NIP NPs synthesized in both MeOH and ACN using MAA and TRIM as the monomer and cross-linker respectively.

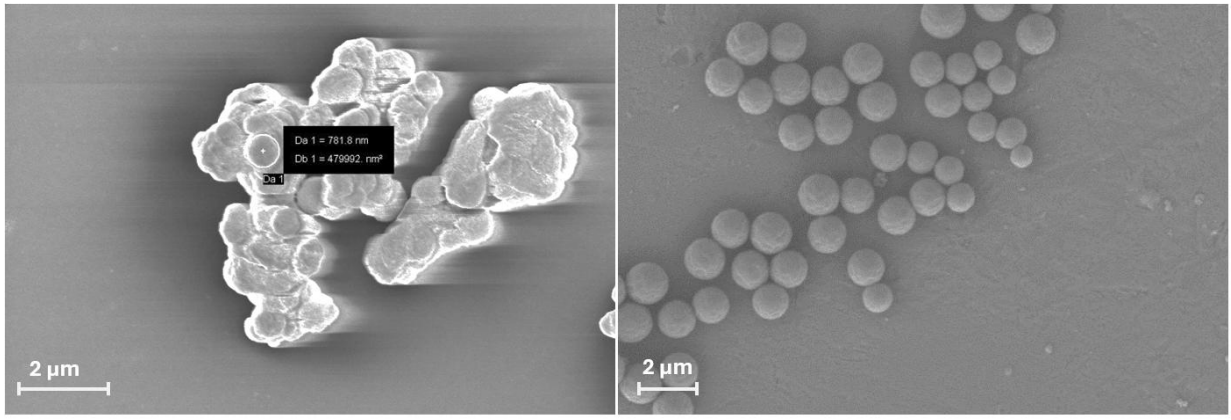

Figure 31: Left: NIP NPs synthesized with MAA:TRIM in MeOH; Right: NIP NPs synthesized with MAA:TRIM in ACN.

Based on these results, a binary solvent system was used in the next step. A small amount of Pen VK was dissolved in dH_2O as the protic component, which was then mixed with ACN in a 9:1 (v/v) ratio (ACN:dH_2O). Figure 32 (left) shows the resulting MIP and NIP NPs. The polymer structure appears highly aggregated and clustered, indicating poor NP dispersion.

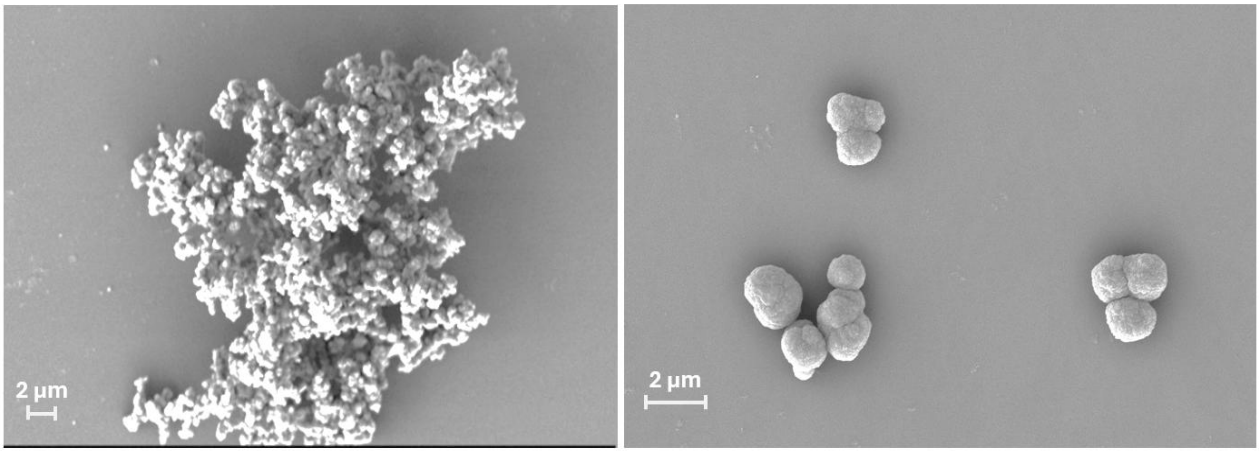

Figure 32: Left: NIP NPs of MAA:TRIM in ACN:dH_2O; Right: MIP NPs MAA:TRIM:Pen VK in ACN:dH_2O.

The solvent was then switched to ACN as the only solvent, which requires using Pen V free acid instead of salt. To achieve this, Pen VK was converted to Pen V free acid as described in section 4.1.2. Figure 32 (right) shows the results that using Pen V free acid, MAA as the monomer and TRIM as the cross-linker in acetonitrile results in spherical MIP nanoparticles. MAA forms strong hydrogen bonds and electrostatic interactions with the Pen V molecules, establishing a well-defined pre-polymerization complex. TRIM, with its three-dimensional structure, provides a highly cross-linked network, ensuring a rigid and stable polymer matrix. Acetonitrile, being an aprotic solvent, supports these interactions and enhances the solubility of the components, leading to controlled and uniform growth of the polymer particles [125].

Figure 33 reveals a heterogeneous population of nanoparticles with a broad size distribution. While most particles are spherical, their diameters vary significantly, ranging from below 100 nm to over 500 nm.

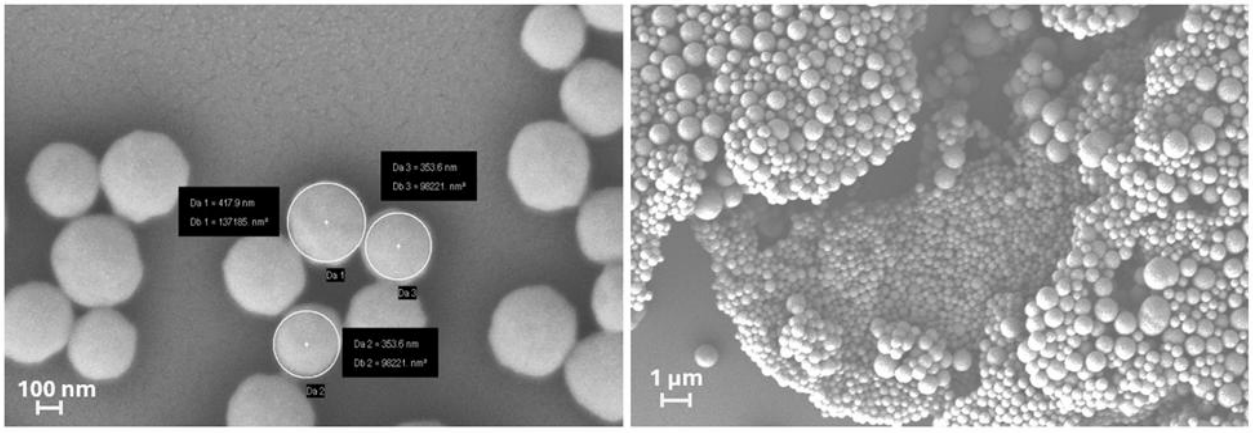

Figure 33: SEM images of MIP NPs in ACN with highly variable sizes and broad distribution.

Pen V MIP NP Size Modification

Modification of Pen V MIP NPs size was achieved using the optimized molar ratio of MAA:TRIM:Pen V (2.10:3.5:1) and 20% w/w AIBN in 40 mL of ACN. Figure 34 and Figure 35 show SEM and DLS results of the MIP NPs with particle sizes ranging from 178 nm to 222 nm.

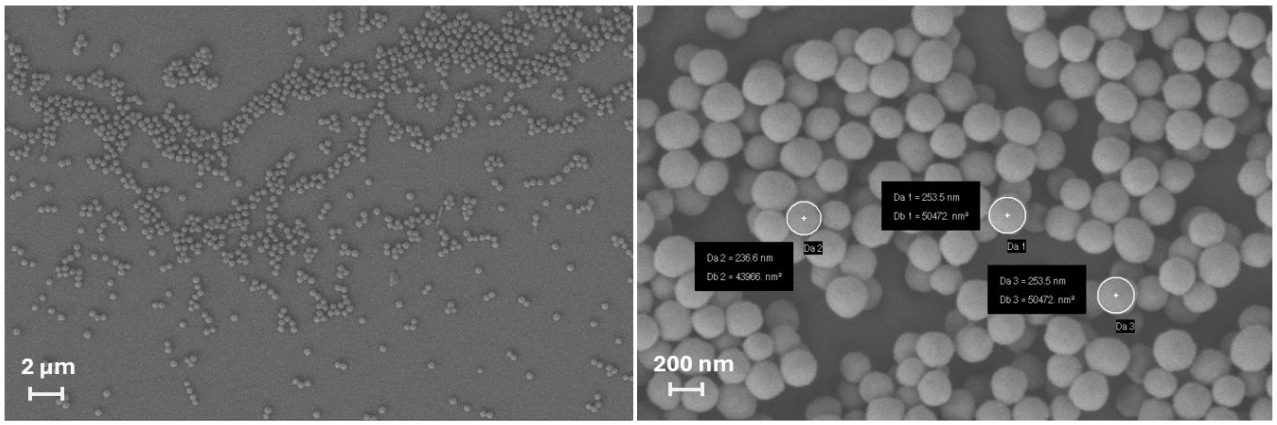

Figure 34: SEM images of Pen V MIP NPs at magnifications with scale bars of 2 µm and 200 nm.

Initially, limited control over the polymerization conditions resulted in broader size distribution and some aggregation as shown in Figure 33 previously. However, by increasing the pre-polymerization time from 10 to 20 minutes, a narrower size distribution and more well-defined, individual nanoparticles were successfully synthesized.

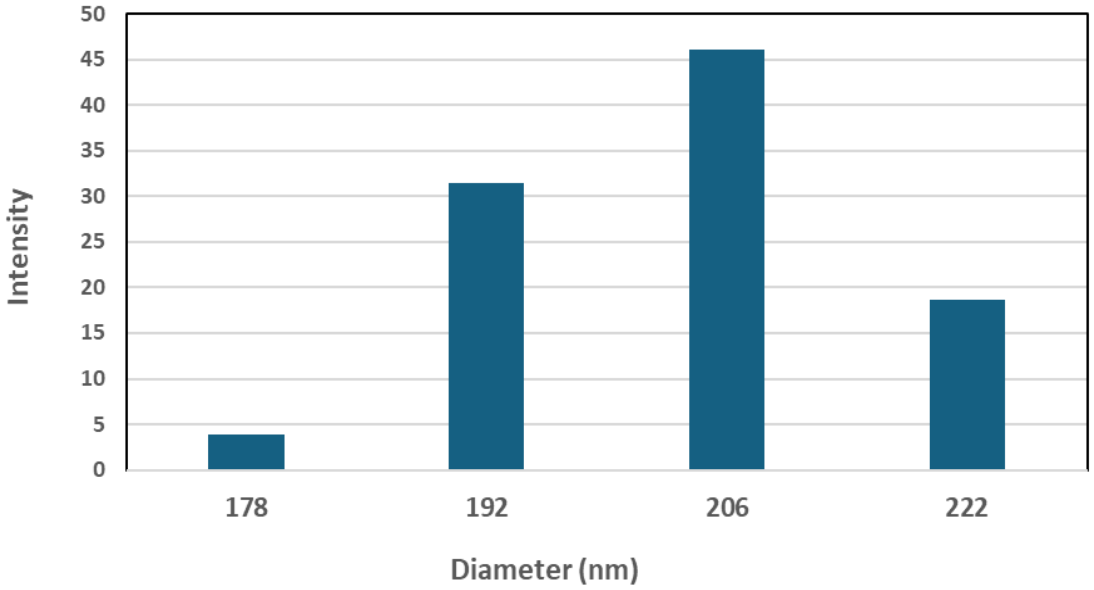

Figure 35: DLS results of Pen V MIP NPs dispersed in EtOH, showing the PDI of 0.16.

4.2.2. Verification of Pen V Acid Formation

For the characterization of Pen V free acid, ATR-FTIR was performed using a PerkinElmer spectrometer equipped with a gold diamond ATR module (Specac). ATR-FTIR was used instead of traditional FT-IR because it allows for direct analysis of solid and liquid samples without the need for sample preparation, such as grinding with KBr or forming pellets. For the Pen V sample, ATR was ideal as it provided a fast, non-destructive method that ensured good surface contact and reliable spectral data without altering the sample's physical state. Figure 36 shows IR spectra of both Pen VK (orange line) and Pen V free acid (blue line) both in solid form. The O–H stretch of a carboxylic acid typically appears as a very broad envelope in the range of 2500–3500 cm^{-1} due to strong hydrogen bonding and dimer formation in the solid state. This broad band is often shallow

and can easily merge with the baseline, making it difficult to distinguish as a sharp peak. Moreover, in solids, carboxylic acid groups commonly engage in extensive hydrogen bonding, which causes a red-shift and further broadening of the O–H stretch compared to the sharp, well-defined O–H signals observed for free, non-bonded alcohols in solution. In addition, the broad O–H absorption overlaps with the C–H stretching region and various combination or overtone bands, often masking any distinct O–H feature.

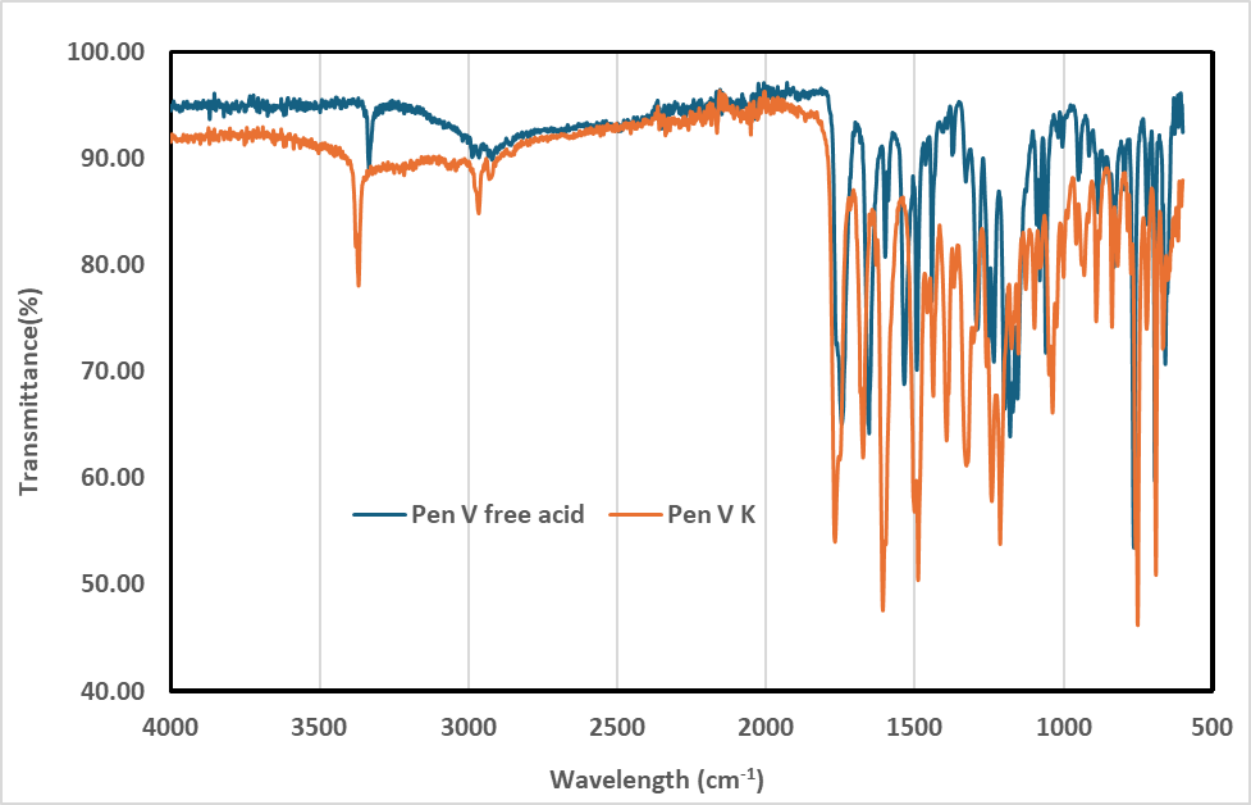

Figure 36: ATR-IR spectra of Pen VK (orange line) and Pen V free acid (blue line).

Additionally, as Figure 37 shows the IR spectrum of Pen V free acid, the carbonyl (C=O) stretching band of the carboxylic acid group typically appears around 1700–1670 cm^{-1}.

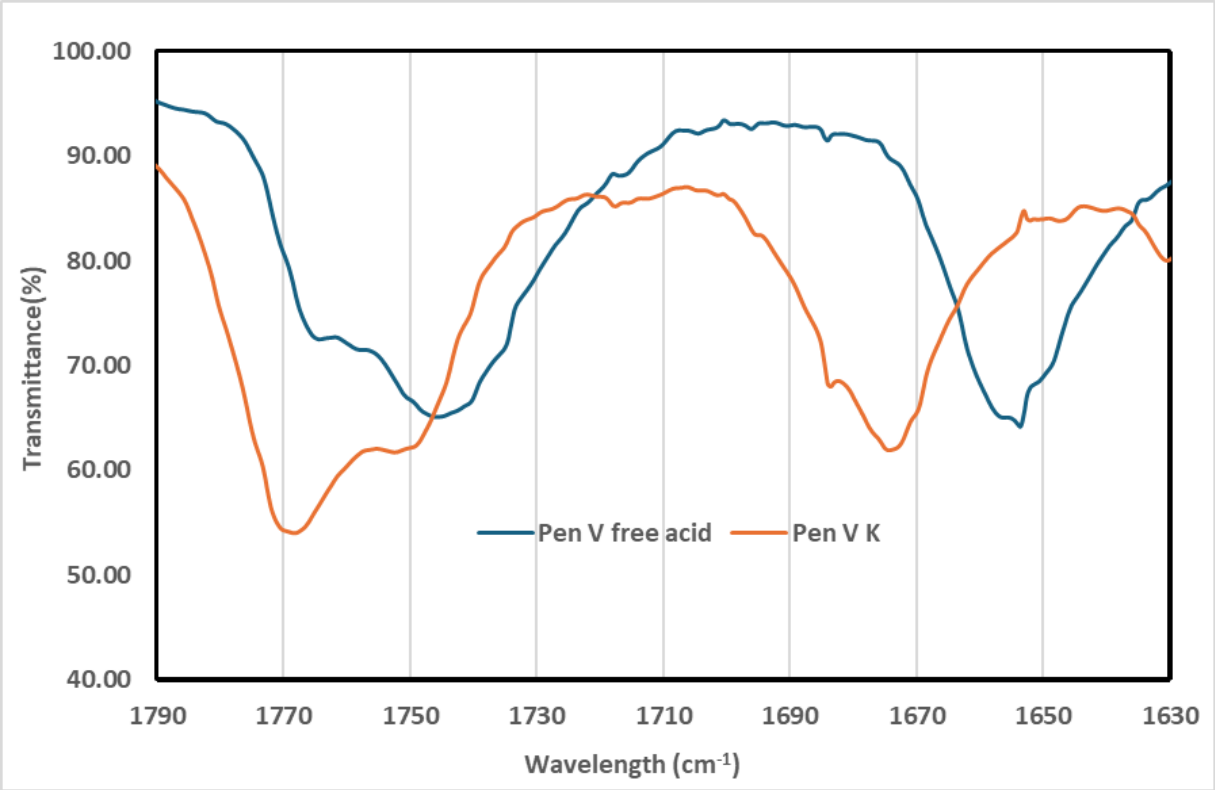

Figure 37: The Lactam ring spectra at 1760-1790 and C=O carboxylic peak around 1650-1725.

However, in the solid-state, this band often shifts slightly to a lower frequency, around 1670–1650 cm^{-1}. This shift is attributed to the formation of hydrogen-bonded dimers between carboxylic acid groups. In the solid form, Pen V molecules can associate through intermolecular hydrogen bonding between –COOH groups, leading to dimerization. This hydrogen bonding stabilizes the carbonyl group, reduces the double bond character slightly and consequently lowers the stretching frequency.

Additionally, the β-lactam C=O stretching band at ~1775 cm^{-1} is clearly visible in both spectra, confirming that the Penicillin core remains intact, i.e. they do not decompose.

4.2.3. Sensor Characteristic

Measurement Background

To determine the sensitivity of the sensor Pen VK, initially, measurements were conducted in an aqueous KNO_3 solution (0.1 M) to minimize the influence of changes in ionic strength on QCM measurements and thereby improve the accuracy and reliability of the results. However, as shown in Figure 38: The QCM result of sensitivity measurement of sensors at a concentration of 10-50 mM of Pen V in dH2O and KNO3., the sensitivity (slope) was 17.69 in KNO_3 and 17.4 in dH_2O, which are very close to each other.

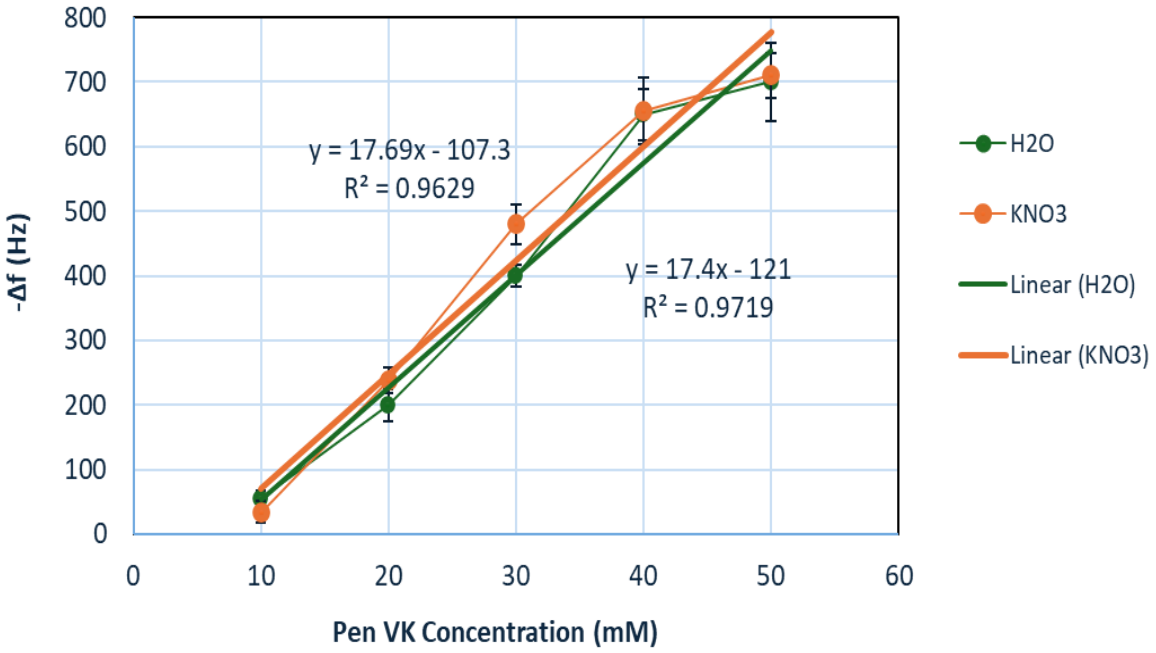

Figure 38: The QCM result of sensitivity measurement of sensors at a concentration of 10-50 mM of Pen V in dH_2O and KNO_3.

The high R^2 values (0.97 and 0.96) indicate that the linear models fit the data well in both media. This suggests that the frequency shift per unit concentration of Pen VK and hence the sensitivity of the MIP sensors is minimally affected by ionic strength. Therefore, since the aim of this study

was to measure Pen VK in water, further QCM measurements were conducted using dH_2O at a neutral pH of 7.4.

Template Extraction and Sensitivity

Figure 39 shows the QCM responses of MIP and NIP nanoparticles extracted via soxhlet extraction using EtOH as the washing solvent. The sensors were prepared loading approximately 3 ng of MIP or NIP NPs on each electrode and exposed to Pen VK at two different concentrations: 50 mM and 25 mM. Each concentration was injected three times, followed by washing with dH_2O to return to the baseline.

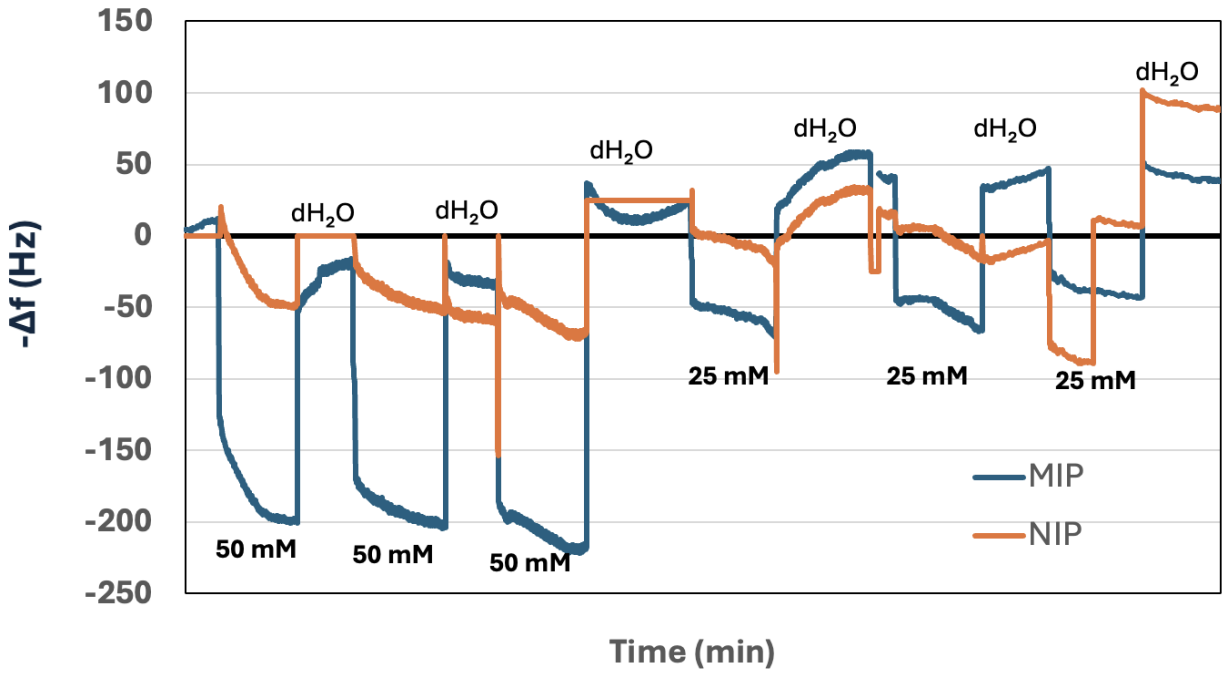

Figure 39: QCM responses of Pen V MIP and NIP NPs extracted via soxhlet extraction and EtOH at 50 and 25 mM of Pen VK.

The responses clearly demonstrate concentration-dependent binding behavior, with two times higher frequency shifts observed at 50 mM compared to 25 mM. Importantly, all signals are

reversible, i.e. the frequency returns to baseline after each washing cycle. The MIP nanoparticles consistently exhibit significantly higher frequency shifts than corresponding NIP, which indicates specific recognition of Pen VK. For instance, at a concentration of 50 mM Pen VK, the MIP nanoparticles exhibited frequency shifts of approximately −200 Hz, while the corresponding NIP signal was around −50 Hz, resulting in an imprinting factor (IF) of 4.

For reproducibility tests as shown in Figure 39, the QCM responses were obtained from three consecutive exposures to the same sample, with washing steps in between. Each concentration was injected three times and the results consistently showed similar responses each time.

Figure 40 shows the QCM responses of MIP and NIP nanoparticles after template extraction using AcOH:MeOH (2:8). The sensors were tested with three different concentrations of Pen VK in dH_2O at 50 mM, 25 mM and 12 mM. The MIP-based sensors exhibit significantly higher responses, reaching up to –500 Hz, compared to nanoparticles where the template was removed via soxhlet extraction, which only yielded approximately –200 Hz.

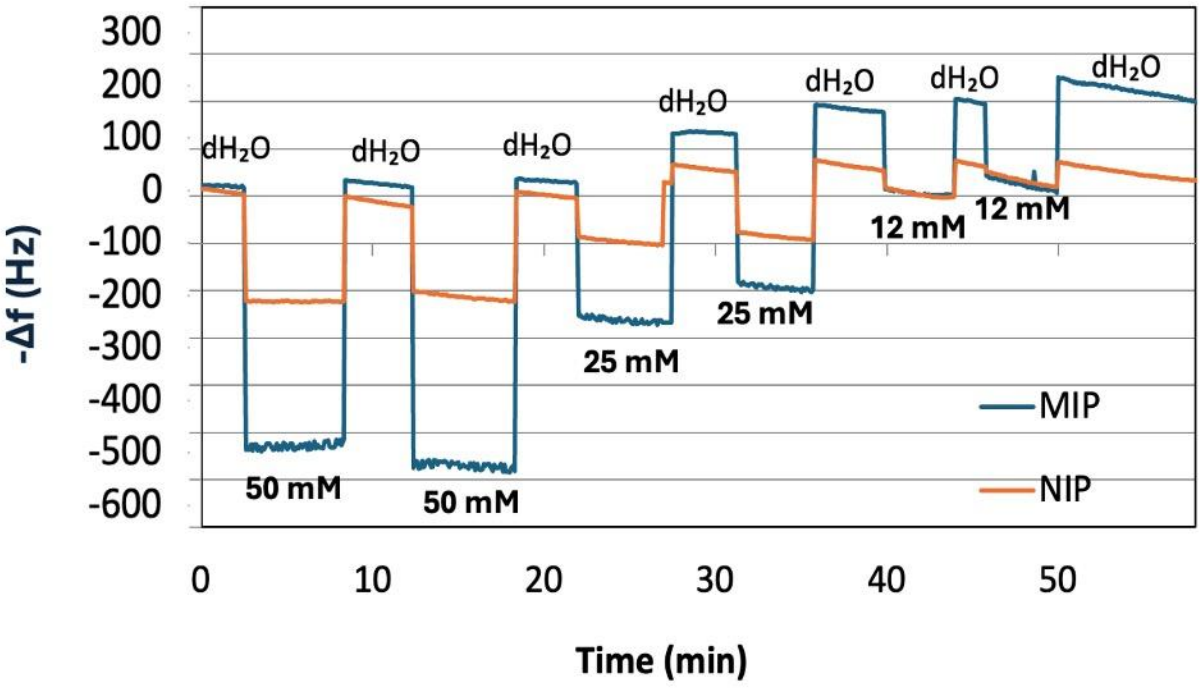

Figure 40: QCM responses of Pen V MIP and NIP NPs extracted with AcOH:MeOH (2:8) at 50, 25, 12 mM.

This suggests that AcOH:MeOH more efficiently removes the template. Based on these findings, the extraction protocol was further optimized by increasing the content of acetic acid from 10% to 20% and incorporating an additional 30-minute sonication step following stirring. This lead to enhanced sensor responses, likely due to more effective template removal and the creation of more accessible and active binding sites within the MIP structure.

Table 7 summarizes the extraction methods of Pen V MIPs using different protic solvents, as described in section 4.1.3. The table presents the sensor responses to 50 mM Pen VK, showing that the highest response was obtained using the extraction method with AcOH:MeOH (2:8) under stirring and sonication for 24 hours and 30 minutes, respectively. Furthermore, the polymer thickness ranged between 270–310 nm and since the values were close, the influence of thickness was negligible.

Table 7: Comparison of template extraction methods for Pen V MIP NPs based on QCM response (–Δf) to Pen VK 50 mM.

Solvent (v/v)	**Method**	**Time (hour)**	**-Δf (MIP-NIP) (Hz)**
EtOH	Soxhlet extraction	24	150 ± 40
MeOH, 10% AcOH	Soxhlet extraction	24	210 ± 50
EtOH	Stirring	48	200 ± 80
AcOH:MeOH (1:9)	Stirring	48	300 ± 80
AcOH:MeOH (2:8)	Stirring, sonication	24, then for 30 min	380 ± 70

Selectivity

Selectivity is a crucial property of any sensor, as it demonstrates that the recognition cavities indeed selectively bind the template species. To evaluate selectivity, compounds with similar chemical structures to the target analyte were chosen. The responses from both MIP and NIP sensors to Pen GK and Amo Na as compatible compounds were compared to the response results of the target, Pen VK. Figure 41 displays the chemical structures of three Penicillins used in the selectivity measurements.

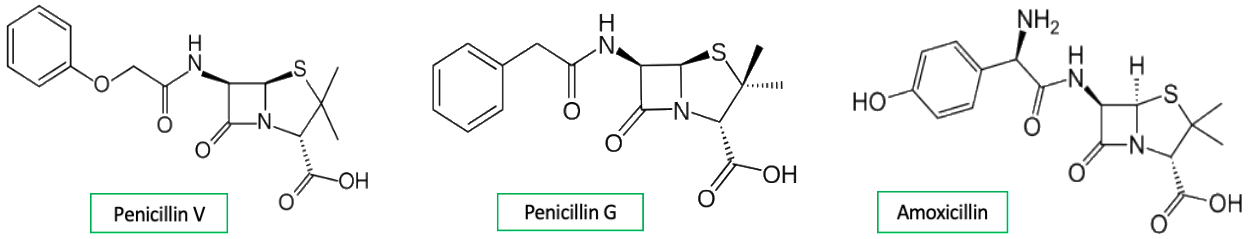

Figure 41: Chemical structure of Pen V, Pen G and Amo.

The results in Figure 42 show QCM responses of MIP and NIP sensors to Pen VK, Pen GK and Amo Na (50 mM). MIP exhibited the highest frequency shift for Pen VK (–500 Hz), indicating strong binding. Moderate response to Pen GK (–250 Hz) and low response to Amo Na (~–100 Hz) confirm selectivity. NIP showed minimal responses to all compounds, lacking specific binding sites. Each injection was repeated twice, showing consistent and reproducible signals. Overall, the MIP sensor demonstrates strong selectivity for Pen VK over similar structures.

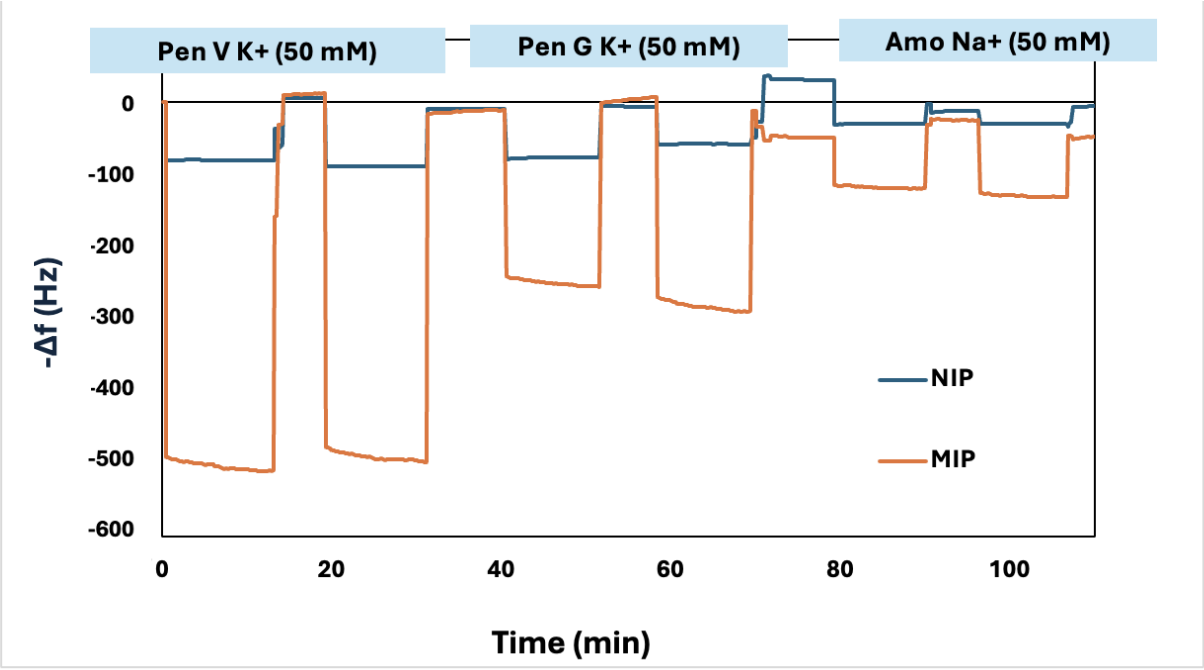

Figure 42: Selectivity results of (MAA:TRIM) MIP and NIP towards Pen VK, Pen GK and Amo NA at 50 mM of each.

FBAR measurements

For the FBAR array developed within the AquaNOSE project, the pixels were coated with MIP and NIP nanoparticles, as previously described in section 3.1.6. Figure 43 displays the frequency responses of the activated pixels coated with (MAA-co-TRIM) MIP upon exposure to 50 mM Pen VK in a dH_2O background.

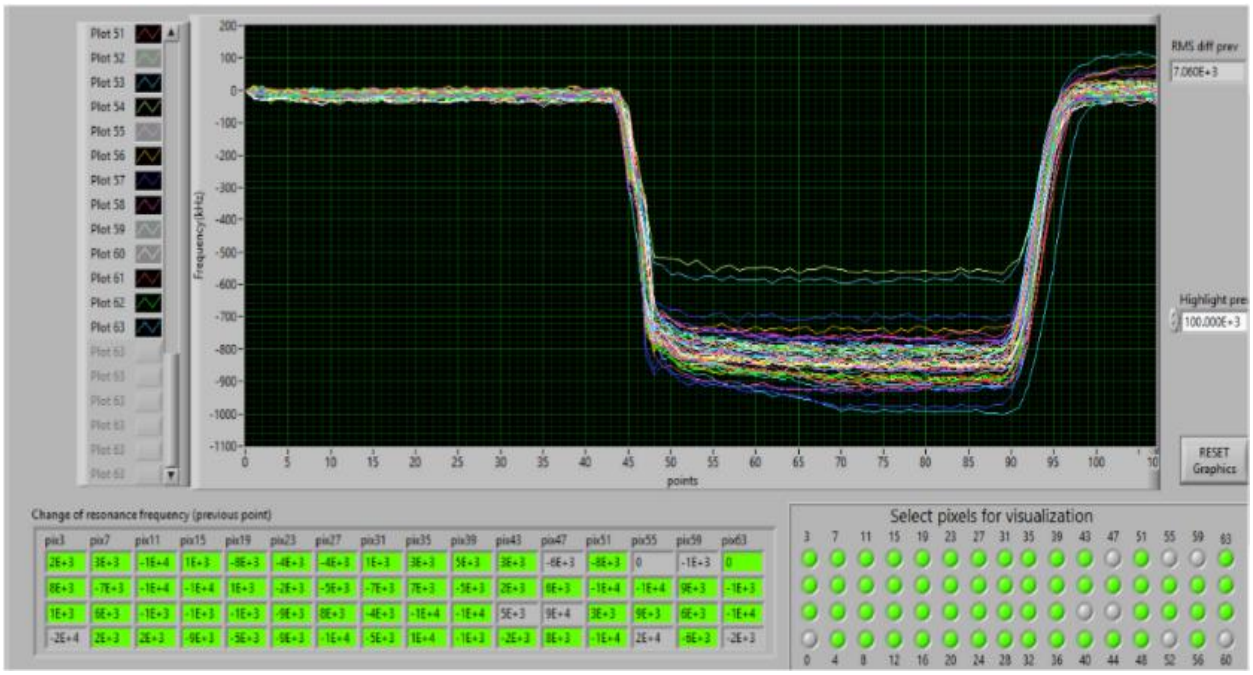

Figure 43: The frequency response of 64 pixels on a single FBAR device coated with poly (MAA-co-TRIM) MIP after exposure to 50 mM Pen VK.

Most signals show consistent and comparable frequency shifts, indicating uniform sensor behavior and reproducible binding to Pen VK. A few outlier signals, which show slightly higher shifts in both response and baseline after washing, are likely due to system-related fluctuations rather than differences in polymer performance.

Figure 44 shows the responses of an FBAR chip coated with MIP NPs on one half (32 pixels) and NIP NPs on the other half when exposed to various concentrations of Pen VK in dH_2O. The MIP-

coated side exhibited strong, concentration-dependent frequency shifts, approximately –450 kHz for 50 mM, –280 kHz for 25 mM, –220 kHz for 12 mM and –150 kHz for 6 mM Pen VK. In contrast, the NIP-coated side showed inverse responses, indicating non-specific interactions or physical adsorption effects rather than selective binding. These results demonstrate the sensor's sensitive recognition of the target analyte.

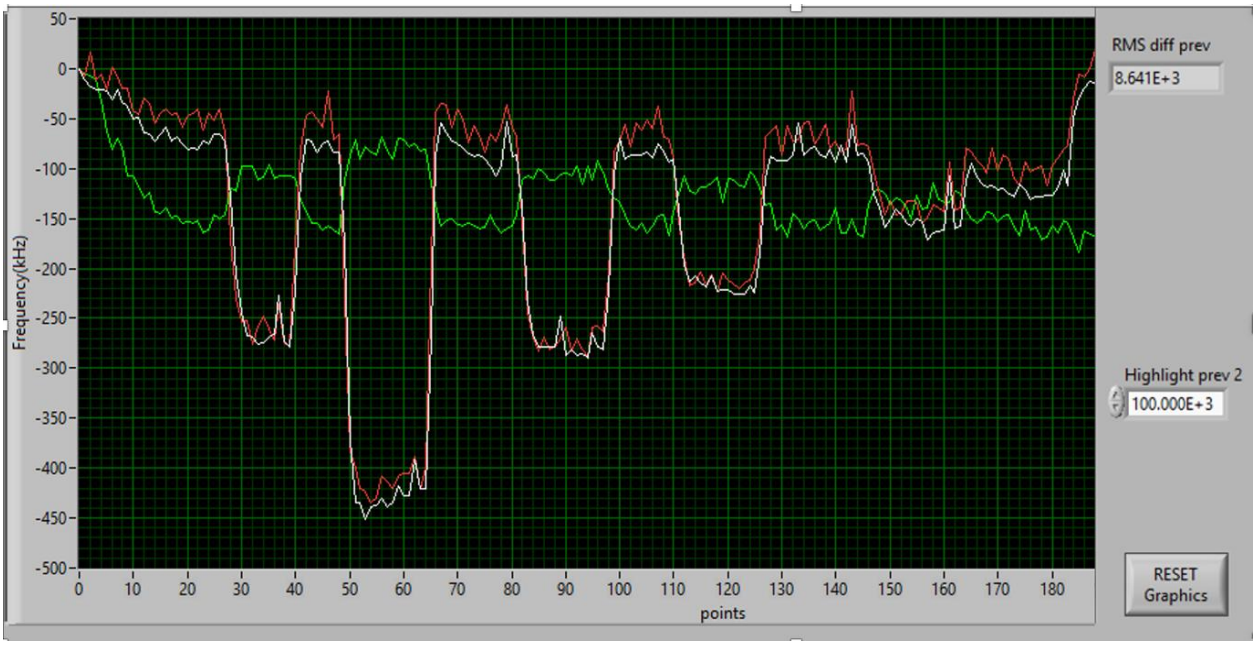

Figure 44: The frequency response of selected pixels of a single FBAR chip. The red and white curves represent the responses of surfaces coated with MIP NPs, while the green curve corresponds to the surface coated with NIP NPs.

Figure 45 presents the results of MIP nanoparticles exposed to Pen VK at three concentrations (50, 25 and 12.5 mM), with two repetitions per concentration to assess reproducibility. This is followed by selectivity measurements using 50 mM solutions of Pen GK and Amo Na. The responses are consistent with those observed during QCM measurements, confirming a higher and selective response toward Pen VK. In this setup, the selectivity factor (SF) of Pen VK relative to both Pen GK and Amo Na was approximately 1.28, indicating modest preference.

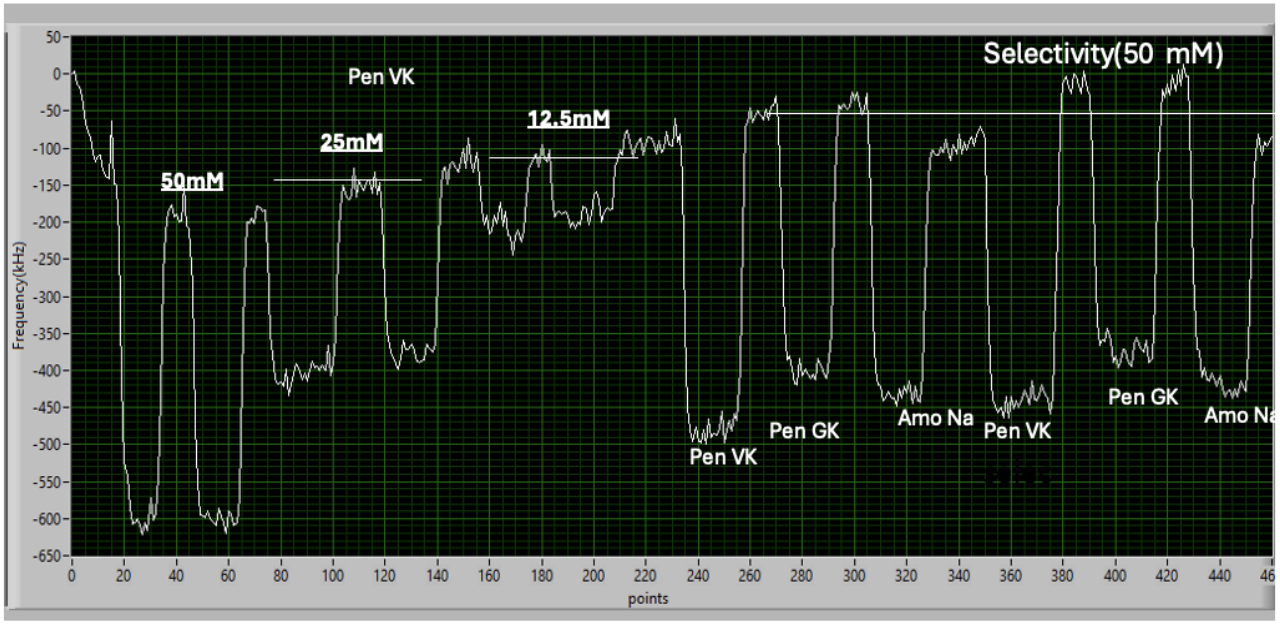

Figure 45: The sensitivity and selectivity of poly (MAA:TRIM) MIP nanoparticles towards various concentrations of Pen VK (50, 25, 12.5 mM) and selectivity assessment using Pen GK and Amo Na (both at 50 mM).

However, in the previous QCM measurements, the SFs were more pronounced: 2.0 for Pen VK vs. Pen GK and 5.0 for Pen VK vs. Amo Na, highlighting that selectivity depends not only on binding interactions but also on the sensing platform and transduction mechanism. Whereas FBAR, though more sensitive in theory, can be more affected by non-binding-related influences, making its selectivity appear lower.

4.2.4. Optimization of Binding Affinity of Pen V MIP NPs

To improve the binding affinity of Pen V MIP NPs, co-monomer and co-cross-linker systems were employed. The sensitivity and selectivity of a series of MIP and NIP NPs were evaluated and compared to investigating the influence of monomer type, cross-linker composition and their

respective ratios on the binding performance. MAA and AA were selected as compatible acrylic monomers, differing only by a methyl group, as shown in Figure 46. Two different MAA:AA ratios were tested 0.9:0.1 and 0.7:0.3, as detailed in the synthesis on page 48, Table 6.

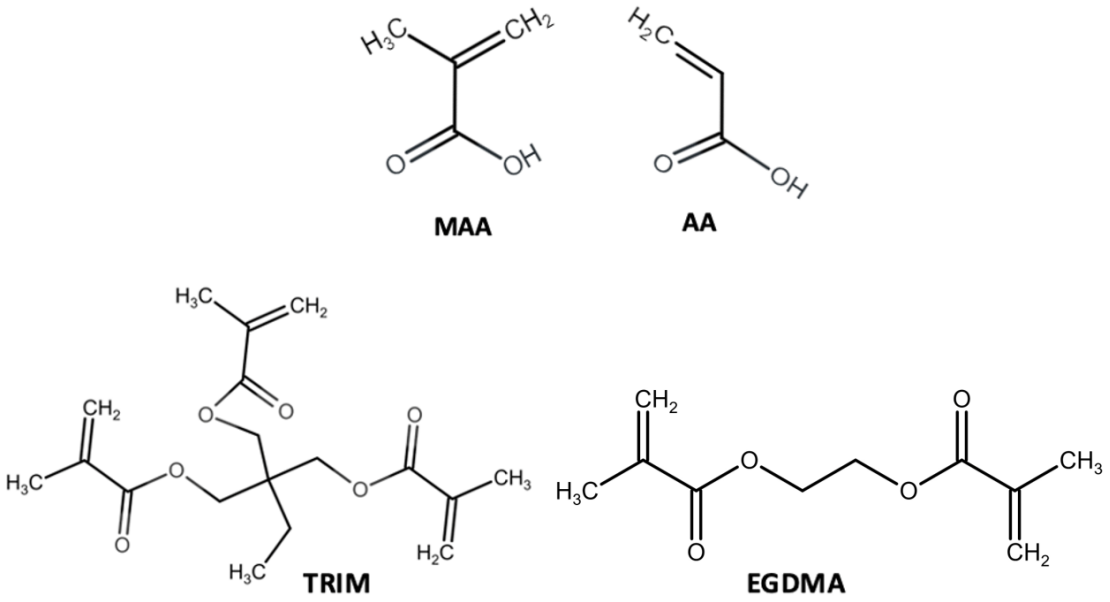

Figure 46: Chemical structures of used monomers MAA and AA and two type cross-linkers: TRIM and EGDMA.

Figure 47 illustrates the sensor characteristics of the corresponding MIPs and their respective NIPs towards Pen VK. The results indicate that MIP 3 (Table 6, page 48) with MAA:AA of 0.7:0.3 showed the highest response at approximately –3500 Hz, followed by MIP 2 (MAA:AA, 0.9:0.1) with –2500 Hz. These findings suggest that increasing the AA content in the polymer matrix enhances the binding affinity of the MIP towards the analyte, likely due to improved interaction within the imprinted cavities. This improvement can be attributed to the increased hydrophilicity and higher functional group density introduced by the elevated AA content. Furthermore, a more hydrophilic polymer network facilitates better analyte diffusion in aqueous environments, improving accessibility to the binding sites and thereby significantly enhancing the sensitivity and performance of MIPs.

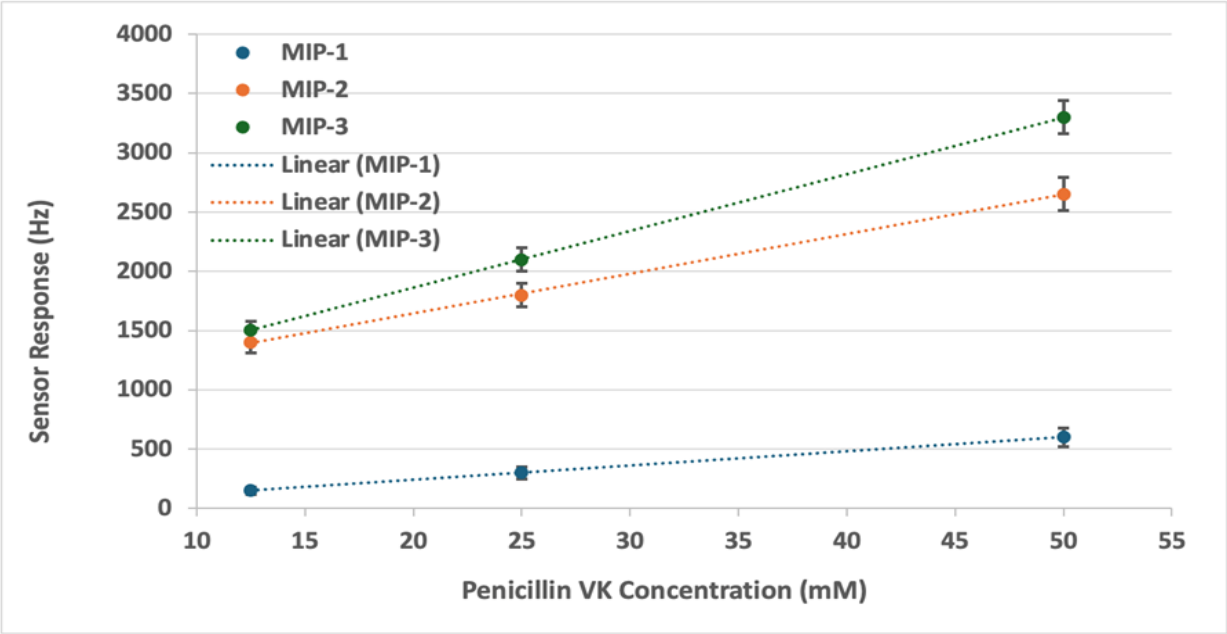

Figure 47: Sensor characteristics of MIP 1, MIP 2 and MIP 3.

Following the improvements in binding performance, a co-cross-linker system combining TRIM and EGDMA was synthesized, as previously described in Table 6. These two cross-linkers differ in their chemical structure, as illustrated in Figure 48, and are expected to impact on the mechanical properties of the polymer matrix differently. Specifically, the combination of TRIM and EGDMA can influence the rigidity and flexibility of the polymer network, potentially affecting the stability of the imprinted cavities, thereby enhancing binding affinity.

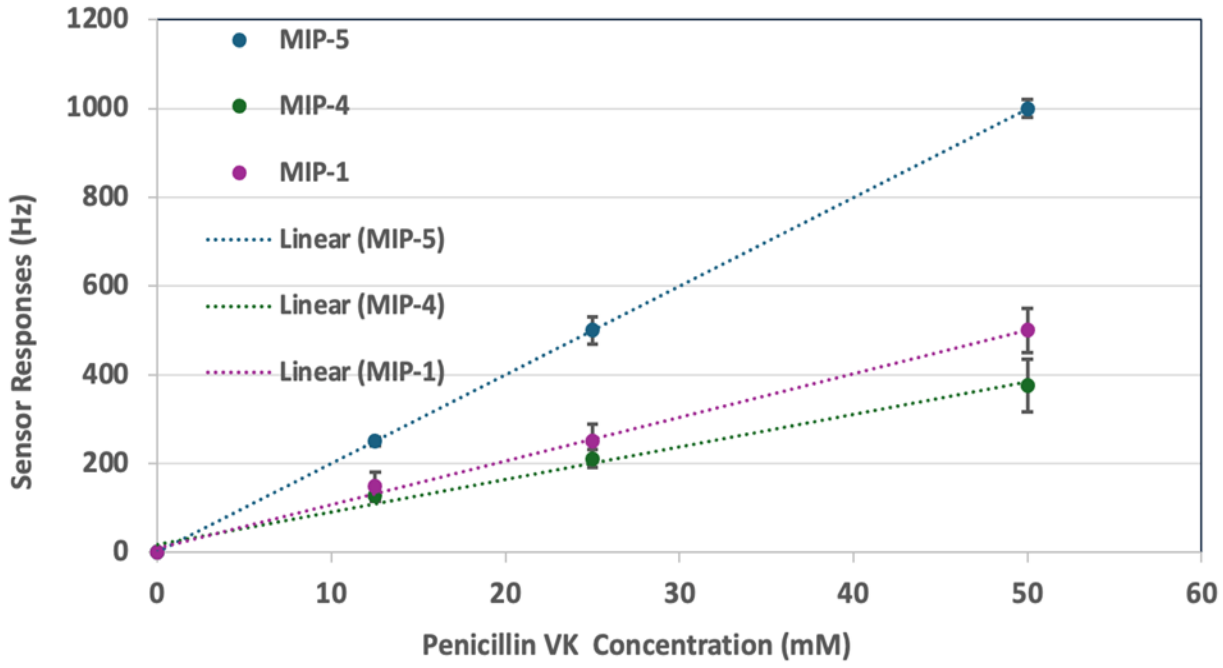

Figure 48: Sensitivity results of MIP 1, MIP 4 and MIP 5 toward Pen VK.

The MIP synthesized with both TRIM and EGDMA exhibited a significantly higher frequency shift of approximately –1000 Hz in response to 50 mM Pen VK, compared to MIP 1 and MIP 5, which were synthesized using only a single type of cross-linker. This suggests that using a mixed crosslinker system may better support the formation of stable and accessible binding sites within the MIP structure [126].

Selectivity

Table 8 summarizes the differences in frequency shifts between MIP and NIP for MIP 1 to MIP 5, alongside a comparison of their selectivity factors (SF). The highest selectivity was observed in MIP 1, with a value of 2.0 and 4.0 against Pen GK and Amo Na, respectively. Although increasing the AA content in the MIP system enhances the overall binding strength, it also introduces non-

specific interactions, which may reduce the selectivity of the MIP toward structurally similar interferents.

The influence of different cross-linkers was evaluated using three MIP/NIP pairs: MIP 1 with TRIM, MIP 4 with EGDMA and MIP 5 with a 0.5:0.5 mixture of TRIM and EGDMA. MIP 1 and MIP 5, both incorporating TRIM, exhibited higher selectivity factors, with α(Pen VK/Pen GK) values of 2.0 and 1.62, respectively. In contrast, MIP 4, crosslinked only with EGDMA, results in a less rigid polymer network and less defined binding cavities. Additionally, MIP 4 exhibited the lowest binding affinity, suggesting that MAA:EGDMA-based nanoparticles have weaker interactions with Pen VK compared to TRIM-based systems. This highlights the importance of cross-linker selection in optimizing both binding strength and molecular recognition specificity in MIP design.

Table 8: Difference of frequency (-Δf) resulted of MIP-NIP (Hz) for MIP3-7 sensors to Pen VK (50 mM) and respective LoD, IF and selectivity factor (α).

	-Δf (MIP-NIP) (Hz)					
	Pen VK	**Pen GK**	**Amo Na**	**LoD (mM)**	**α(Pen VK/Pen GK)**	**α(Pen VK/Amo Na)**
MIP 1	800	400	200	1.53	2	4
MIP 2	2500	1700	1500	0.51	1.47	1.66
MIP 3	3500	2600	2200	0.38	1.34	1.59
MIP 4	400	280	200	3	1.42	2
MIP 5	1300	800	400	0.83	1.62	3.25

4.2.5. Cyclic Voltammetry

Cyclic voltammetry (CV) study of the Pen VK sensors was carried out using QCMs individually coated with MIP and NIP, across a range of analyte concentrations. Figure 49 presents the cyclic voltammograms of both MIP and NIP systems, highlighting their electrochemical behaviors in the presence of Pen VK at different concentrations (2, 3.5 and 5 mM) applying a Fe^{3+}/Fe^{2+} redox indicator, as previously discussed in section 4.1.6. When coating the working electrode with MIP particles, the peak current progressively decreases with increasing Pen VK concentration. This trend indicates successful binding of the analyte (Pen VK) to the imprinted polymer, where the resulting decrease in current suggests that the polymer layer acts as a partial barrier to the redox reaction. In contrast, the NIP system exhibits only minimal changes in peak current across the same concentration range. This lack of significant variation confirms limited non-specific binding and reinforces the absence of selective recognition sites in the non-imprinted polymer.

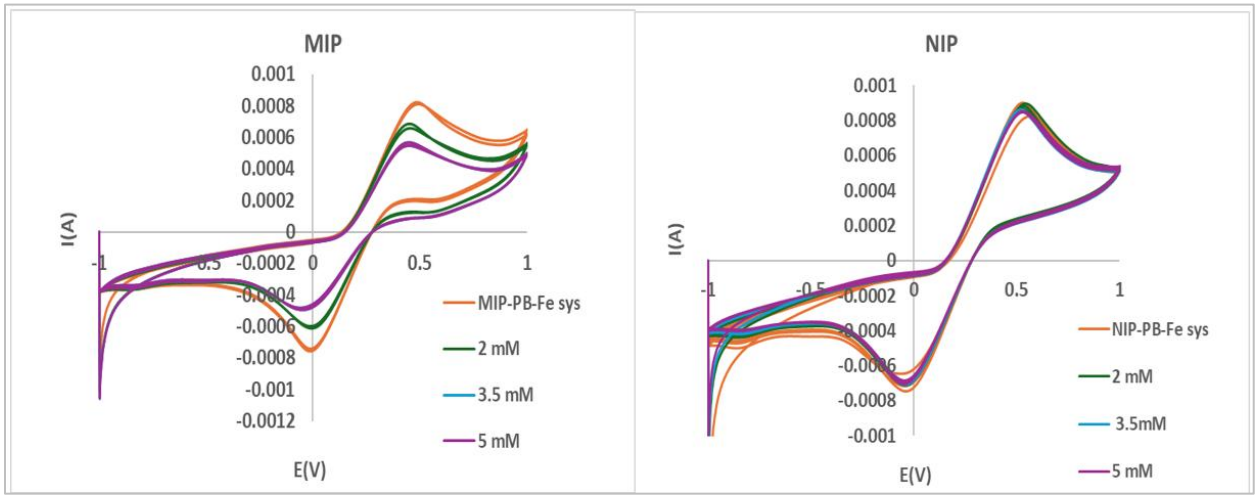

Figure 49: Cyclic voltammograms of Pen VK-MIP (left) and corresponding NIP (right) at three different concentrations (5, 3.5 and 2 mM) in PBS solution (pH 7.4), using the Fe^{3+}/Fe^{2+} as the redox indicator.

Figure 50 (A) shows the linear plot of the MIP sensitivity toward Pen VK, clearly distinguishing it from the NIP. The MIP shows a notable decrease in current with increasing analyte concentration

(R^2 = 0.8602), indicating specific binding to the imprinted polymer. In contrast, the NIP displays minimal variation (R^2 = 0.9166), reflecting non-specific interactions. Although, closer inspection reveals that the decrease in current does not follow a perfectly linear trend with increasing Pen VK concentration. This deviation may be attributed to partial removal of the gold coating on the quartz surface during the oxidation process, which could also lead to subsequent polymer layer detachment, as depicted in Figure 50 (B).

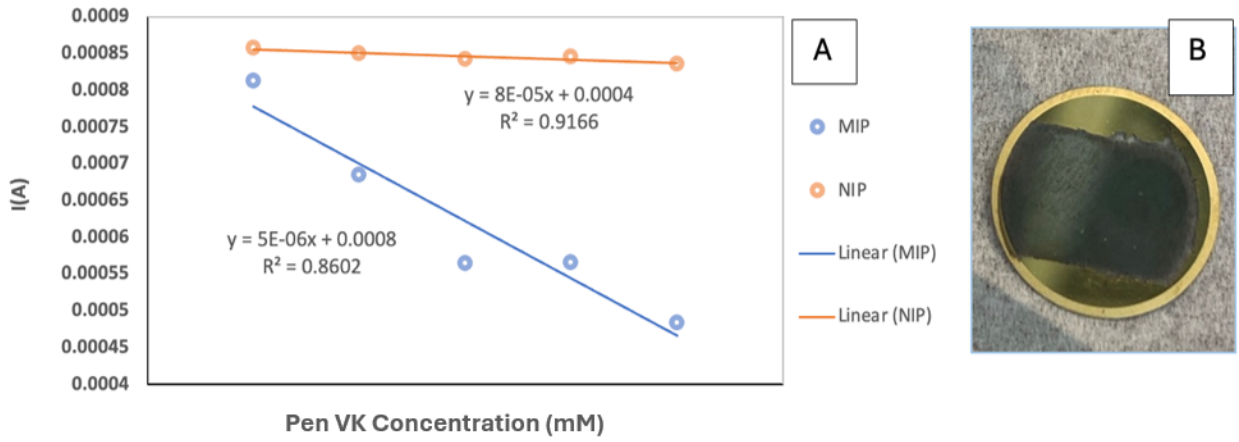

Figure 50: (A) Linear relationship between Pen VK concentration and peak current (I) for MIP and NIP systems. (B) QCM surface after removal of the gold coating on the quartz during the oxidation process.

This observation highlights the potential limitations in the reproducibility and stability of the electrode surface during extended electrochemical cycles, which should be considered when interpreting sensitivity trends in MIP-based sensors.

4.3. Summary and Conclusion

In summary, at the first level the MIP and corresponding NIP NPs are synthesized using MAA as the functional monomer and TRIM as the cross-linker, with Pen VK as the template molecule, via precipitation polymerization. Despite initial challenges with Pen VK solubility and nanoparticle dispersion in protic solvents, the successful conversion of Pen VK to its free acid form and the use of acetonitrile as a solvent significantly improve the homogeneity and morphology of the synthesized MIP nanoparticles. Final particle sizes, achieved under optimized synthesis conditions, range between 178–222 nm, with improved dispersion confirmed through SEM and DLS analyses.

Template extraction emerges as a critical step in enhancing the performance of MIP NPs. Among various strategies tested, extraction using a 2:8 (v/v) mixture of acetic acid and methanol significantly improves sensor sensitivity. At a Pen VK concentration of 50 mM, MIP responses increase up to 600 Hz with an IF of 4.

QCM results reveal a concentration-dependent response of MIP-coated sensors to Pen VK, with frequency shifts increasing proportionally with analyte concentration and an LoD of 1.53 mM. Selectivity tests show high selectivity for Pen VK, with selectivity factors α(Pen VK/Pen GK) = 2.0 and α(Pen VK/Amo Na) = 4.0.

Further optimization of binding affinity is achieved by incorporating co-monomer systems (AA and MAA) and co-cross-linkers (EGDMA and TRIM). Among the tested formulations, the MIP with a MAA:AA ratio of 0.7:0.3 shows the highest sensitivity, achieving a response of 3500 Hz at 50 mM Pen VK and an LoD of 0.35 mM. MIP 1 and MIP 5, both using TRIM as the cross-linker, also exhibit high selectivity, with α(Pen VK/Pen GK) values of 2.0 and 1.62, respectively.

Although increasing AA content enhances binding affinity, it also introduces a degree of non-specific interaction. Therefore, achieving an optimal balance between monomer composition and cross-linker rigidity is essential for maximizing both sensitivity and selectivity.

FBAR sensor platforms further validate Pen VK sensor responses. However, selectivity in the FBAR system decreases compared to the QCM sensors, with the selectivity factor α(Pen VK/Pen GK) dropping from 2.0 to 1.28. This reduction can be attributed to the fact that although FBAR is theoretically more sensitive, it is also more susceptible to non-specific influences, which may affect apparent selectivity.

Cyclic voltammetry provides additional insight into the electrochemical behavior of the MIP and NIP systems. MIP-coated electrodes show a clear decrease in peak current with increasing Pen VK concentration. While an initially linear trend is observed in the MIP current response ($R^2 = 0.8602$), slight deviations occur due to the gradual removal of the gold coating from the quartz surface during extended oxidation cycles.

In conclusion, this work successfully demonstrates the synthesis and application of Pen VK MIP NPs with high sensitivity, selectivity and reproducibility. The integration of optimized polymer chemistry, extraction methods and transduction platforms leads to the development of a highly effective sensing system for Pen VK. These findings not only validate the potential of MIPs for specific antibiotic detection but also lay the groundwork for extending this technology to a broader range of pharmaceutical and environmental targets.

5. Gold Nanoparticles Sensors

This section focuses on designing gold nanoparticles (Au NP) based sensors using commercial Au NPs in size 75 nm purchased from nanoComposix. Au NPs are widely used in sensor development due to their unique physical and chemical properties. They are easy to synthesize, stable and offer a high surface-to-volume ratio with excellent biocompatibility [127]. Their surface can be easily functionalized with a variety of ligands, making them ideal for selective binding and detection of target molecules. The size, shape and surrounding environment of Au NPs can be tuned to optimize sensor performance. These features contribute to the development of highly sensitive, selective and multifunctional chemical and biological sensors [128].

5.1. Experimental

5.1.1. In-Situ Polymerization of Au NPs on QCM Chips

The Au NP are capped with Polyvinylpyrrolidone (PVP) layer as the stabilizer in Milli-Q water. In-situ polymerization was employed as the primary method, utilizing an acrylic polymer system. Polymerization was carried out in-situ on QCM substrates, using MAA as the monomer and TRIM as the cross-linker. Tetrahydrofuran (THF) was employed as the solvent to facilitate the formation of the polymer network.

The approach relies on successful initiation directly near the surface and applying reversible addition-fragmentation chain transfer (SI-RAFT) polymerization aiming at achieving homogeneous surfaces by controlled polymerization. This study relied on 4-Cyano-4-(phenylcarbonothioylthio) pentanoic acid (CPA) as the RAFT agent to effectively mediate the polymerization process, ensuring the formation of well-defined polymer chains. 2,2'-Azobis(2-amidinopropane) dihydrochloride (AAPH) was used as the photo initiator (Figure 51).

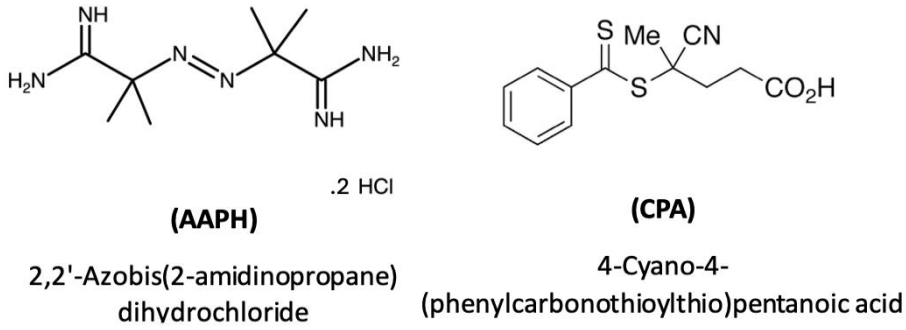

Figure 51: The chemical structures of AAPH and CPA.

Figure 52 sketches 16-mercaptohexadecanoic acid (16-MHDA) immobilization on the QCM surface. To immobilize AAPH on the gold surface of the QCM, the sensor was first washed with acetone and sonicated for 5 minutes. This was followed by treating it with a Diener Zepto-One oxygen plasma cleaner at a pressure of 1.3×10^{-3} mbar for approximately 15 minutes.

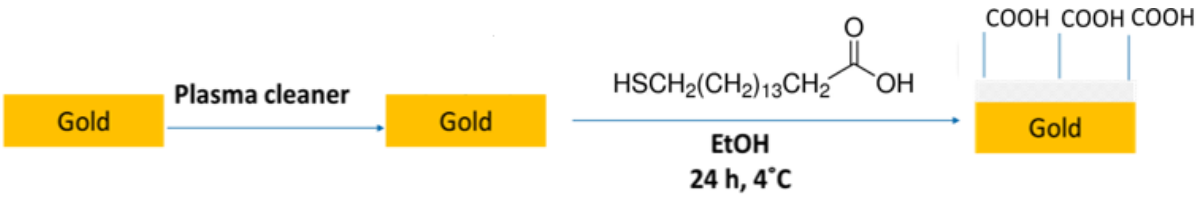

Figure 52: Treatment/functionalization of QCM surfaces for AAPH immobilization.

The cleaned QCM was then placed in a petri dish and immersed in MHDA solution (3 mg in 10 mL ethanol) overnight at 4°C. Afterward, the QCMs were washed three times with 5 mL of ethanol and dH_2O to remove any unbound MHDA.

Figure 53 (A) shows the schematic of AAPH immobilization on the QCM surface. The dried QCMs were then immediately immersed in a vial containing N-hydroxysuccinimide (NHS, 0.1 g, 0.8 mmol), 1-ethyl-3-(3-dimethylaminopropyl) carbodiimide (EDC, 0.116 g, 0.6 mmol) and AAPH

(0.542 g, 2 mmol) dissolved in 10 mL of PBS buffer (pH 7.4) for 3 hours at room temperature to covalently link AAPH to the MHDA layer [129]. Finally, the QCMs were washed with 10 mL of deionized water and ethanol and then used for polymerization.

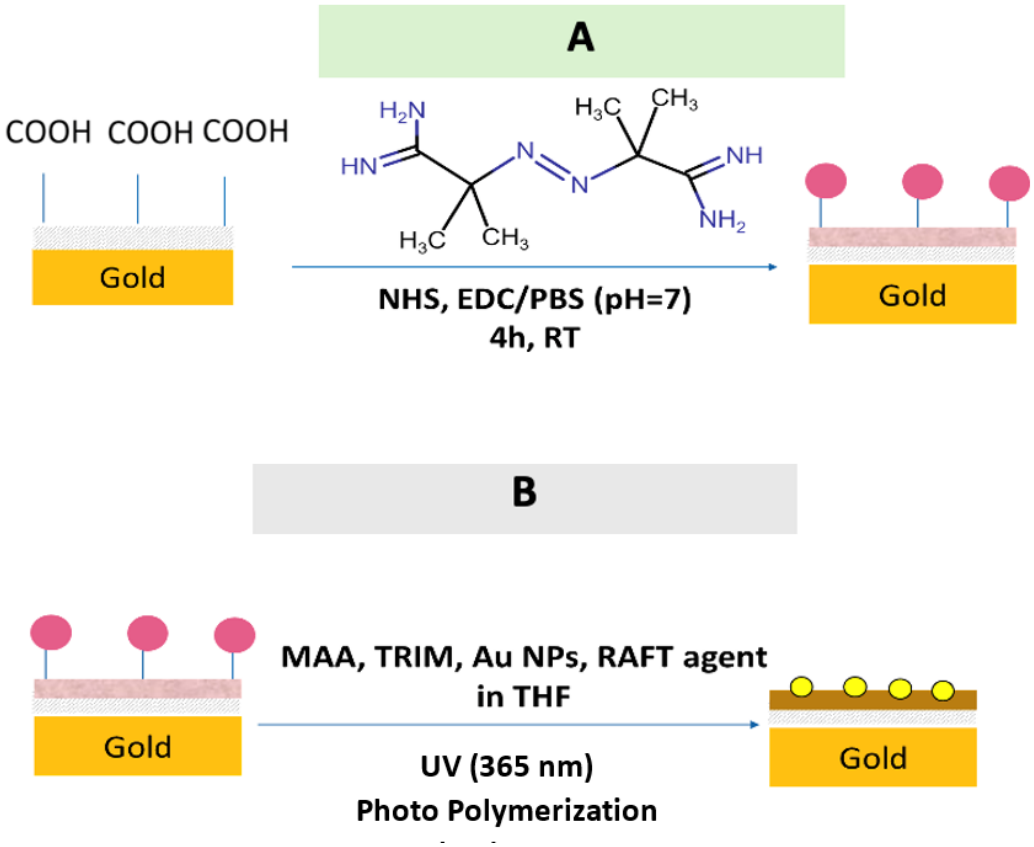

Figure 53: (A) Surface immobilization of AAPH (depicted by pink spheres), (B) In-situ polymerization of Au NPs (yellow spheres) into the MIP matrix.

Figure 53 (B) illustrates the steps for in-situ polymerization of Au NPs. The QCM surfaces were first modified with AAPH which is represented as pink spheres and then placed into 10 mL vials (ND28, TH.GEYER). Each vial contained 6 mL of THF. Subsequently, the polymerization mixture was prepared by adding MAA (86.6 µL, 1 mmol), TRIM (338.6 µL, 1 mmol) and CPA (5 mg,

0.017 mmol). In the MIP sample, Au NPs (100 µL, 1.1×10^{12} particles/mL) were included, whereas the NIP sample was synthesized without Au NPs. All vials were purged with argon for approximately 10 minutes to eliminate dissolved oxygen. Polymerization took place under UV light (365 nm) for 3.5 hours as shown in Figure 54.

After polymerization, the QCM sensors were sequentially washed with 20 mL THF and deionized water (15 minutes each), followed by drying at 85°C overnight. For in-situ polymerization of capped Au NPs with 11-mercapto-1-undecanol (11-MUD), 16-mercapto hexadecanoic acid (16-MHDA), DMSO was used instead of THF, following the same recipe and quantities. Section 5.1.3 describes the detailed procedure of modifying Au NPs.

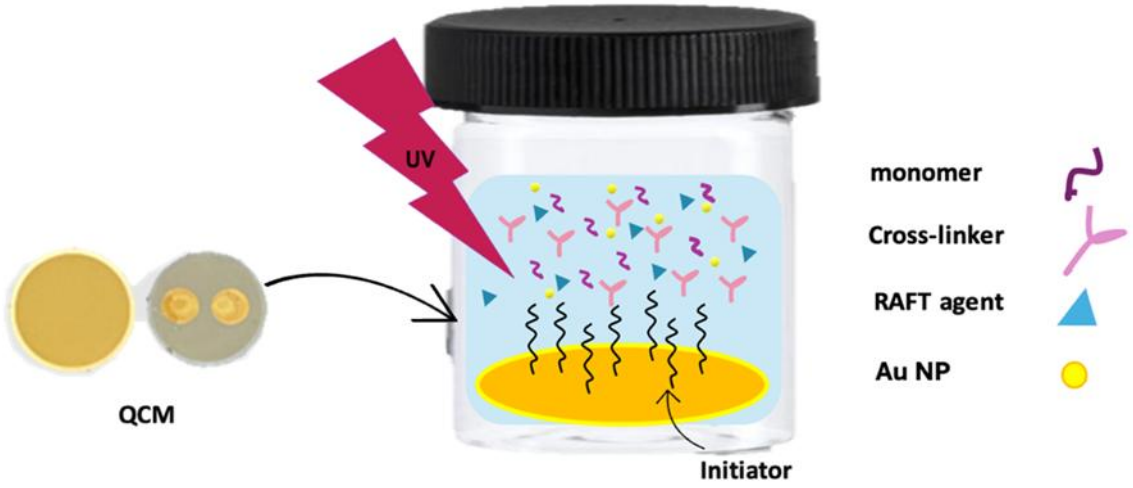

Figure 54: Schematic of in-situ polymerization of MIP.

5.1.2. Au NPs Extraction from the Polymer Matrix

In the first attempt, MIP was imprinted with Au@PVP NPs followed by extracting the NPs using various methods, as described in Table 9. For this purpose, MIP-coated QCMs were immersed in different washing solutions and stirred using a magnetic stirrer. Subsequently, the QCMs were

rinsed with 10 mL of deionized water and dried at 80°C overnight. The polymer surfaces were then examined by AFM and SEM to assess Au NP removal.

Table 9: Au NPs removal methods.

Solvent	Method	Time (hours)
SDS 1%, EtOH	stirring	2.5, 3 (each)
AcOH 10%, dH_2O	stirring	2.5 (each)
NaOH (0.05 M), SDS 1%	stirring	4
NaOH (0.05 M), SDS 1%	40˚C, 600 rpm	24
1-octane thiol in toluene	stirring	4

However, none of these methods proved successful. As a result, subsequent efforts focused on modifying the Au NP surfaces using alternative stabilizers. Prior to this modification, the zeta potentials of the polymer and various stabilizers were analyzed to better understand their interactions and potential effectiveness.

5.1.3. Au NPs Surface Modification

The surfaces of 75 nm Au NPs were modified with different thiol group to facilitate the removal of NPs from the polymer matrix as listed in Table 10. The thiol groups selected were 11-MUD, 16-MHDA and 1-dodecanethiol, chosen based on their different degrees of hydrophilicity.

Solutions of 1 mM 11-MUD (2.043 mg in 10 mL EtOH) and 16-MHDA (2.88 mg in 10 mL EtOH) were prepared in 98% ethanol. To these solutions, 200 µL of Au NPs were added, followed by sonication for 30 minutes. The mixtures were then stored at 4°C overnight. After incubation, the modified NPs were washed twice with ethanol and collected by centrifugation.

For the modification with 1-dodecanethiol, a hydrophobic thiol, 1 mM (2.4 µl in 10 mL toluene) solution was prepared in toluene. The modified Au NPs were used directly in the polymerization process after centrifugation.

Table 10: Different reagents to replace PVP for modifying the Au NPs.

Thiol Group	Molecular Formula	Solvent
16-MHDA	$COOH–(CH_2)_{14}–SH$	EtOH 98%
11-MUD	$HO–(CH_2)_{11}–SH$	EtOH 98%
1-dodecanethiol	$CH_3–(CH_2)_{11}–SH$	Toluene

The different capping of Au NPs with stabilizers results in differences in particle size and zeta potential. To confirm the immobilization of Au NPs coated with different thiol groups, particle size and zeta potential were measured across a range of pH values.

5.1.4. Zeta Potential Measurements

The measurement of the solid surface zeta potentials of in-situ synthesized poly(MAA:TRIM) thin films was previously described in section 3.2.5, page 43.

Au NPs Zeta Potential

Zeta potentials (ζ) of capped Au NPs with PVP and three different stabilizers as listed in Table 10 were measured across a pH range of 3–10, using phosphate buffer (PB) prepared with Milli-Q water and reported as the mean of three measurements by using Zeta cell. The size of the Au NPs for each sample was measured using the same solution in single-use cuvettes.

5.2. Results and Discussion

5.2.1. Optimizing In-Situ Polymerization

For the initial attempt at imprinting Au@PVP NPs via in-situ polymerization, the choice of solvent played a crucial role, significantly affecting the distribution of nanoparticles on the polymer surface. THF is ideal for dispersing Au@PVP NPs because it dissolves PVP efficiently, provides a balanced polarity and promotes stable, uniform nanoparticle distribution without aggregation [130]. To study the dispersion of Au@PVP NPs in THF, different concentrations of the nanoparticle solution were prepared: 100 µL, 150 µL and 200 µL of Au@PVP NPs (5.27 mg/mL) in 6 mL of THF. Then, 5 µL of each solution was drop-coated onto glass slides and analyzed by AFM to determine the optimal nanoparticle concentration for polymerization. Figure 55 shows that nanoparticle aggregation is more pronounced at 200 µL (0.175 mg/mL) and slightly visible at 150 µL (0.137 mg/mL), indicating better dispersion at lower concentrations. Figure 55 (C) shows a uniform and homogeneous distribution of nanoparticles without significant aggregation, indicating that 100 µL (0.0875 mg/mL) is the optimal volume of Au NPs for polymerization. Based on this result, 100 µL of Au NPs was selected for the polymerization recipe.

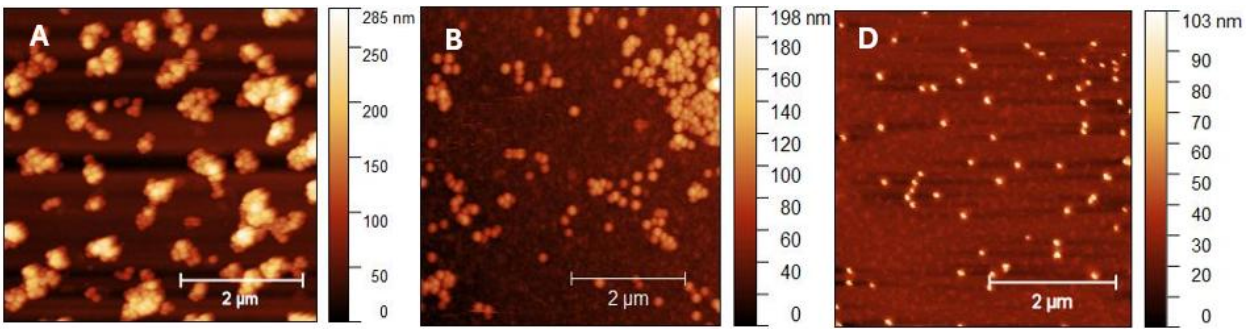

Figure 55: AFM images in tapping mode of Au@PVP NPs in THF using contact mode at a concentration: (A) 200 µL, (B) 150 µL and (C) 100 µL dispersed on glass slides.

To determine the optimum monomer to cross-linker ratio, NIP was synthesized. Initially, ratios of 1:2 and 1:3 (MAA:TRIM) were tested in 6 mL of THF with 5 mg CPA. Figure 56 shows that this results in solid bulk polymers rather than a polymer layer on the QCM surface. Therefore, the cross-linker amount was reduced to a 1:1 monomer to cross-linker ratio (MAA:TRIM).

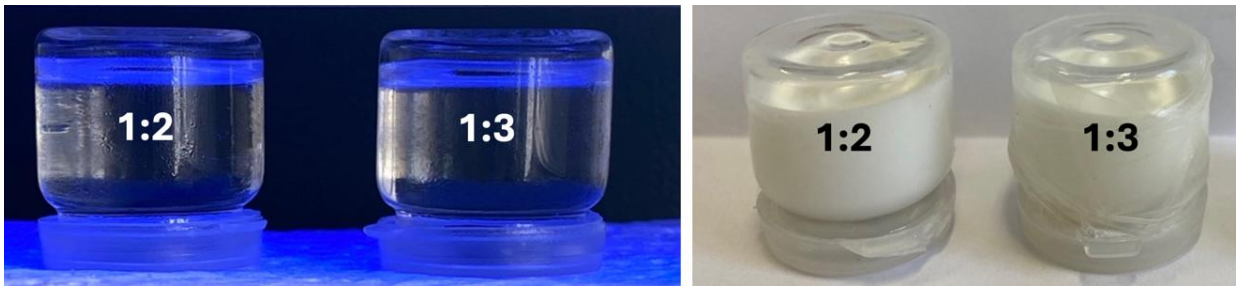

Figure 56: Left: Vials under UV lamp during NIP polymerization using ratios of 1:2 and 1:3 (MAA:TRIM). Right: Resulting NIP polymers after 6 hours of polymerization.

5.2.2. Polymer Thickness

Polymer thickness is another critical parameter which directly affects the coverage of nanoparticles. Lower coverage is desirable to facilitate better removal of Au NPs. To reach the desired polymer layer height, a series of NIP-coated QCMs were prepared with different polymerization times ranging from 1 to 6 hours, in one-hour intervals. The polymer thickness was then estimated using a network analyzer (E5062A ENA Series, Agilent Technologies) by measuring the frequency shift before and after polymerization as shown in Figure 57 for NIP in 4 hours of polymerization time. For each time point, three QCMs were prepared to ensure reproducibility. The results reveal that adjusting the polymerization time allows for tuning the polymer thickness, ensuring consistent and reliable results for sensing applications.

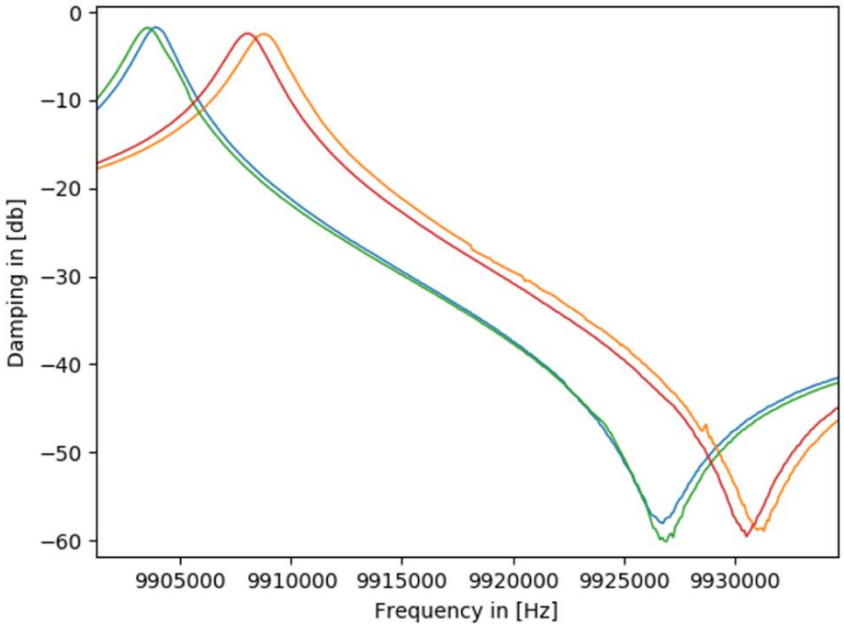

Figure 57: NIP thickness measurement using a network analyzer on both electrodes of a single QCM before and after polymerization. The data show a thickness of 16 nm on the left electrode (green–blue curve) and 20 nm on the right electrode (orange–red curve).

Figure 58 clearly demonstrates a time-dependent increase in polymer thickness, ranging from approximately 5 nm at 1 hour to over 90 nm at 6 hours. This indicates that polymerization proceeds at a relatively constant rate at the selected conditions. Based on these findings, a polymer thickness in the range of 15–20 nm achieved at approximately 3.5 hours of polymerization was selected as the optimal thickness for both MIP and NIP syntheses.

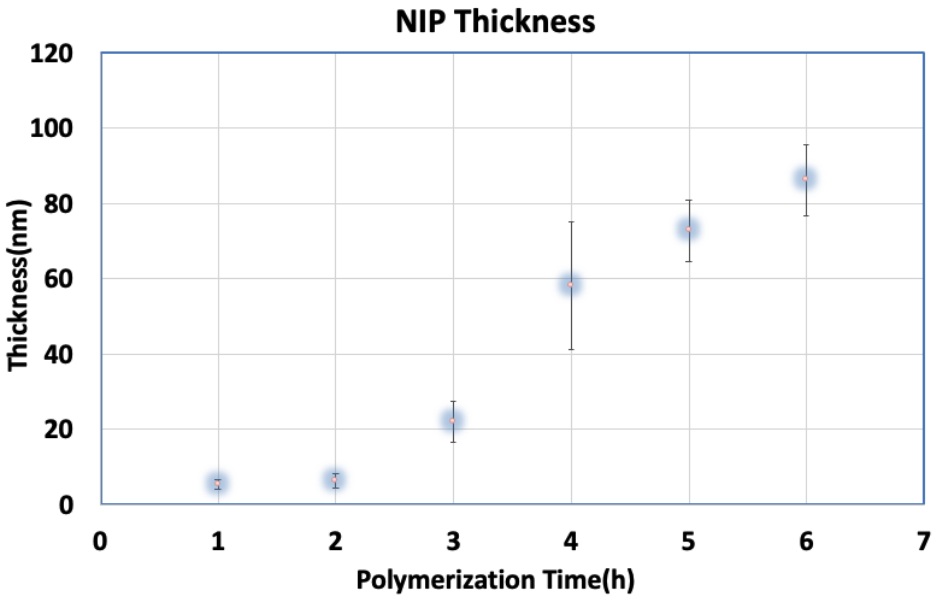

Figure 58: NIP thickness at different polymerization times (1–6 hours).

The MIPs were synthesized as described earlier in section 5.1.1, using Au@PVP NPs and a polymerization time of 3.5 hours to achieve the optimal polymer thickness, i.e. lower than the particle radius. AFM imaging of the MIP surface (Figure 59) confirms successful nanoparticle imprinting, with the polymer and nanoparticle heights clearly distinguishable. Height profile analysis reveals a polymer thickness of approximately 13 nm, while the uncovered area of the nanoparticles extends 59 nm above the polymer surface. This indicates a total nanoparticle size of around 72 nm, which aligns well with the expected dimensions of the Au@PVP NPs and sufficient polymer height with THF in 3.5 hours.

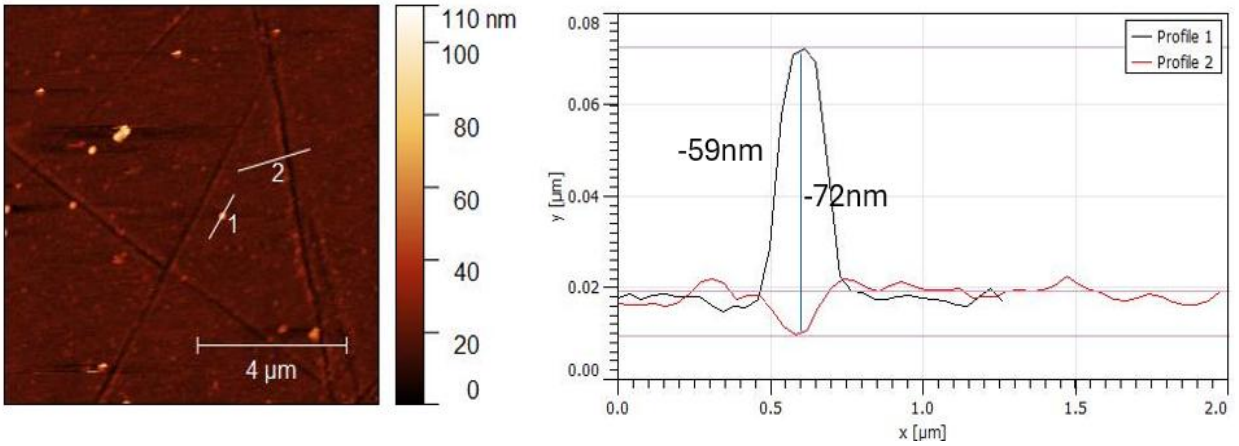

Figure 59: Left: AFM image of the MIP surface immediately after polymerization; Right: Height profile showing two selected features: (1) Au@PVP NPs and (2) a scratched line through the polymer layer indicating polymer depth.

5.2.3. Template Extraction

Following successful incorporation of Au NPs into the polymer, the MIP-coated QCMs were prepared for extraction to remove the nanoparticles. To identify the most effective extraction solution, it was necessary to investigate the interaction between the polymer and the Au NPs. Therefore, the zeta potential (ζ) of PMMA was determined, as previously described in section 5.1.4. Figure 60 shows that the zeta potential of PMAA becomes increasingly negative as the pH increases from 2 to 10. This leads to following conclusions:

1. Low pH (2-4): At low pH, the zeta potential of PMAA is around -10 mV. This relatively low negative charge suggests that carboxylic acid groups (–COOH) on PMAA are mostly protonated, meaning the polymer carries fewer negative charges and remains less ionized.
2. Mid pH (5-6): The zeta potential becomes slightly more negative (still around -10 mV), indicating the onset of deprotonation of carboxyl groups into $–COO^-$, increasing the negative surface charge.

3. Higher pH (7-10): A sharp drop in zeta potential occurs, reaching about -30 mV. This reflects significant deprotonation of the PMAA chains, leading to increased electrostatic repulsion and higher colloidal stability due to stronger negative surface charge.

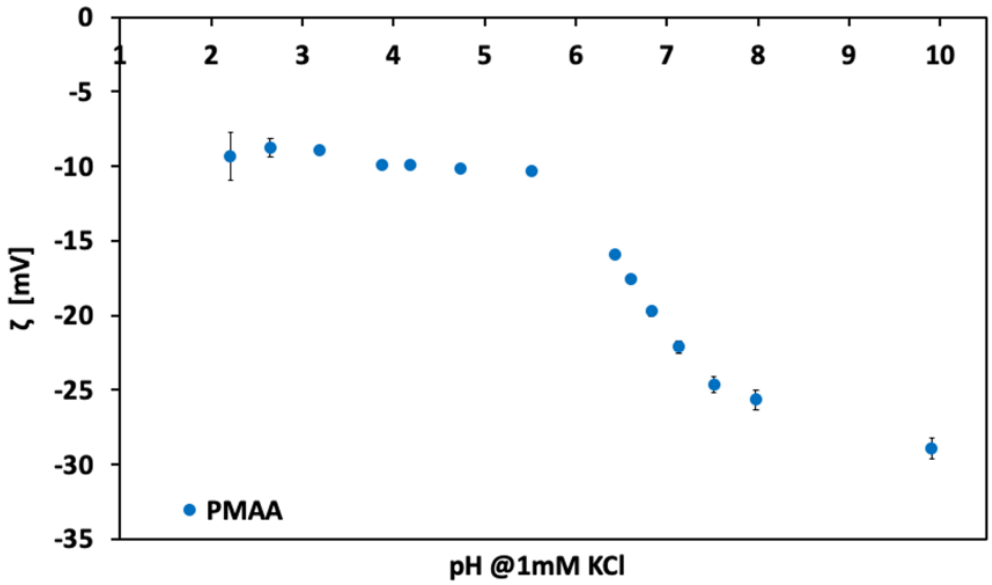

Figure 60: Zeta potential of PMAA in 1 mM KCl across pH 2–10.

Evidently, PMAA exhibits predominantly negative zeta potential. Au@PVP also shows a zeta potential of –28.3 mV at neutral pH. This suggests that one strategy to facilitate particle detachment is to adjust pH. By increasing the pH to 9–10, PMAA becomes fully deprotonated (–COOH → $–COO^-$), thereby enhancing electrostatic repulsion of the already negatively charged Au@PVP NPs. This increased repulsion, along with weakened hydrogen bonding, is expected to facilitate nanoparticle removal. Hence Table 9 (page 78) presents various solutions employed for the removal of particles from MIP-coated QCMs.

AFM images served to evaluate the effectiveness of each washing method. AcOH (10%) was used to lower the pH below 3 to protonate PMAA, thereby reducing electrostatic repulsion and promoting bonding. SDS (1%) and ethanol were applied as a washing solution combining surfactant and swelling solvent properties to disrupt hydrogen bonds. Additionally, 1-octanethiol

was used to remove nanoparticles by replacing the PVP shell of the Au NPs. Physical treatments such as sonication and heating at 40°C were also tested. However, the results showed that none of these methods successfully removed the Au NPs. One possible explanation is the high density of gold (approximately 20.6 g/cm³), which makes particles very heavy and, thus, probably difficult to remove by applying shear forces.

5.2.4. Au NPs Surface Modification

As shown in Figure 61, the surface charge of Au NPs depends on the functional groups of their stabilizing ligands at neutral pH. For 1-dodecanethiol and PVP, which are hydrophobic, the zeta potential remains slightly negative. In contrast, polar functional groups, such as the –OH group in 11-MUD [131] and the –COOH group in 16-MHDA [132], lead to more negative surface charge.

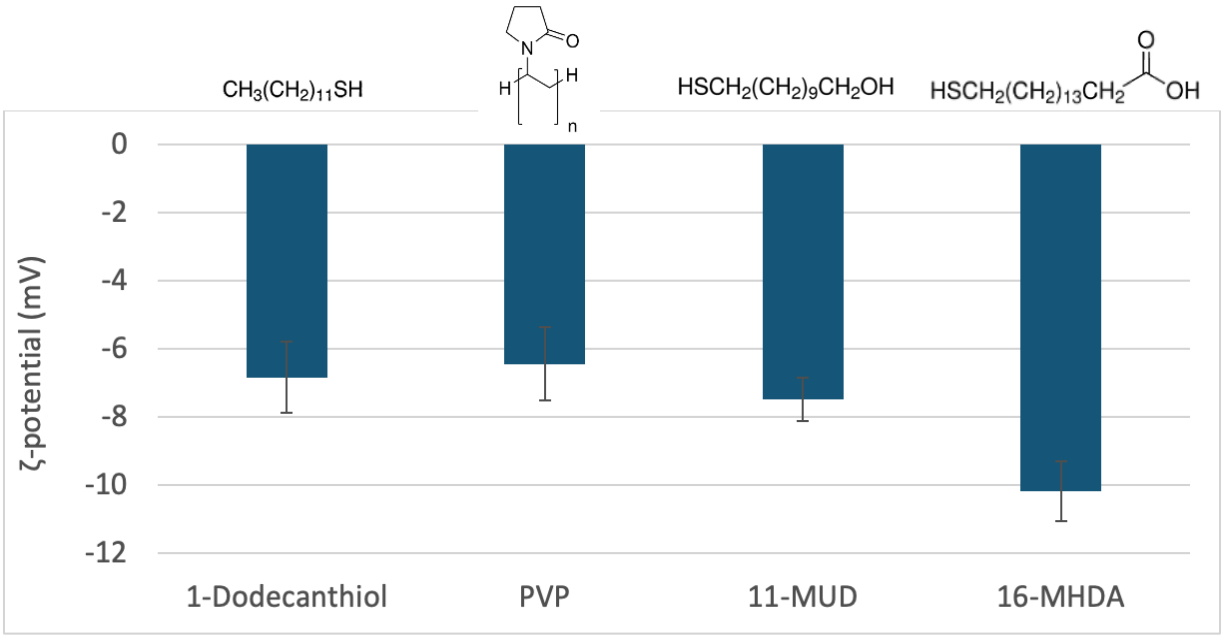

Figure 61: Zeta potential of Au NPs coated with different stabilizers at neutral pH.

The coated layer of Au NPs not only affects the surface charge but also influences the particle size and dispersion behavior of NPs. Figure 62 shows the hydrodynamic diameters of coated Au NPs measured at a pH of 7.4 as described earlier in section 5.1.4.

The hydrodynamic diameter of Au NPs varies significantly with surface coating: at neutral pH, the results show that PVP gives the smallest and most uniform particles (~115 nm), while 16-MHDA yields the largest (~675 nm), likely due to extended chains and/or aggregation.

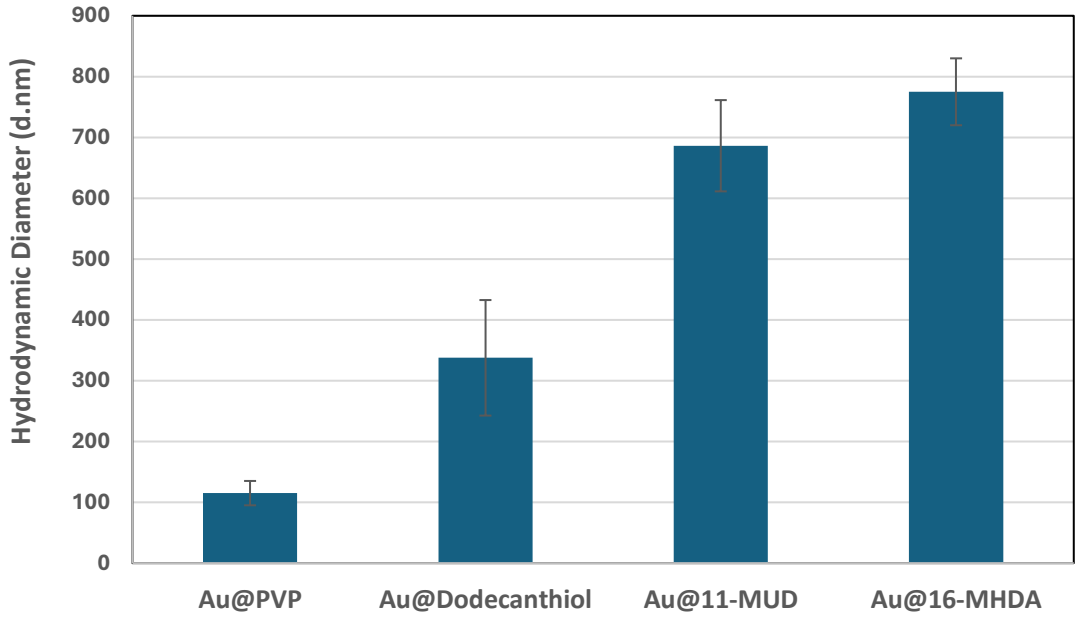

Figure 62: Hydrodynamic diameter of Au NPs with different coating layers in PBS (pH 7.4).

Surprisingly, 11-MUD NPs are slightly smaller than 16-MHDA despite shorter chains, possibly due to weaker surface charge and more hydration. Dodecanethiol-coated NPs show high size variation, indicating instability in aqueous media [133]. Intensity-based size distribution as shown in Figure 63 confirms PVP being the most monodisperse and 16-MHDA and 1-dodecanethiol showing broader distributions.

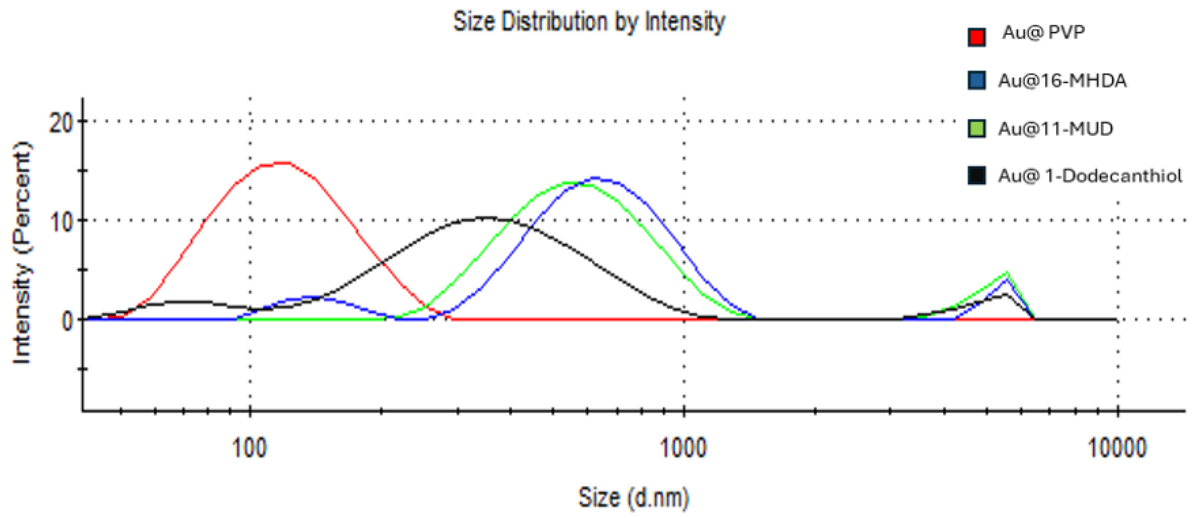

Figure 63: Intensity distributions of Au NPs coated with 11-MUD, 16-MHDA, 1-dodecanthiol, PVP, respectively.

Figure 64 shows the dispersion and aggregation behavior of Au NPs functionalized with the different ligands. 11-MUD displays significant aggregation, indicating poor colloidal stability in THF. 1-dodecanethiol shows a slight distribution of NPs in THF, suggesting poor dispersion and possible precipitation. In contrast, 16-MHDA exhibits better particle distribution and lower aggregation, likely due to its long hydrophobic chain providing better compatibility with THF. PVP-coated NPs also show relatively good dispersion, supported by steric stabilization from the polymer shell.

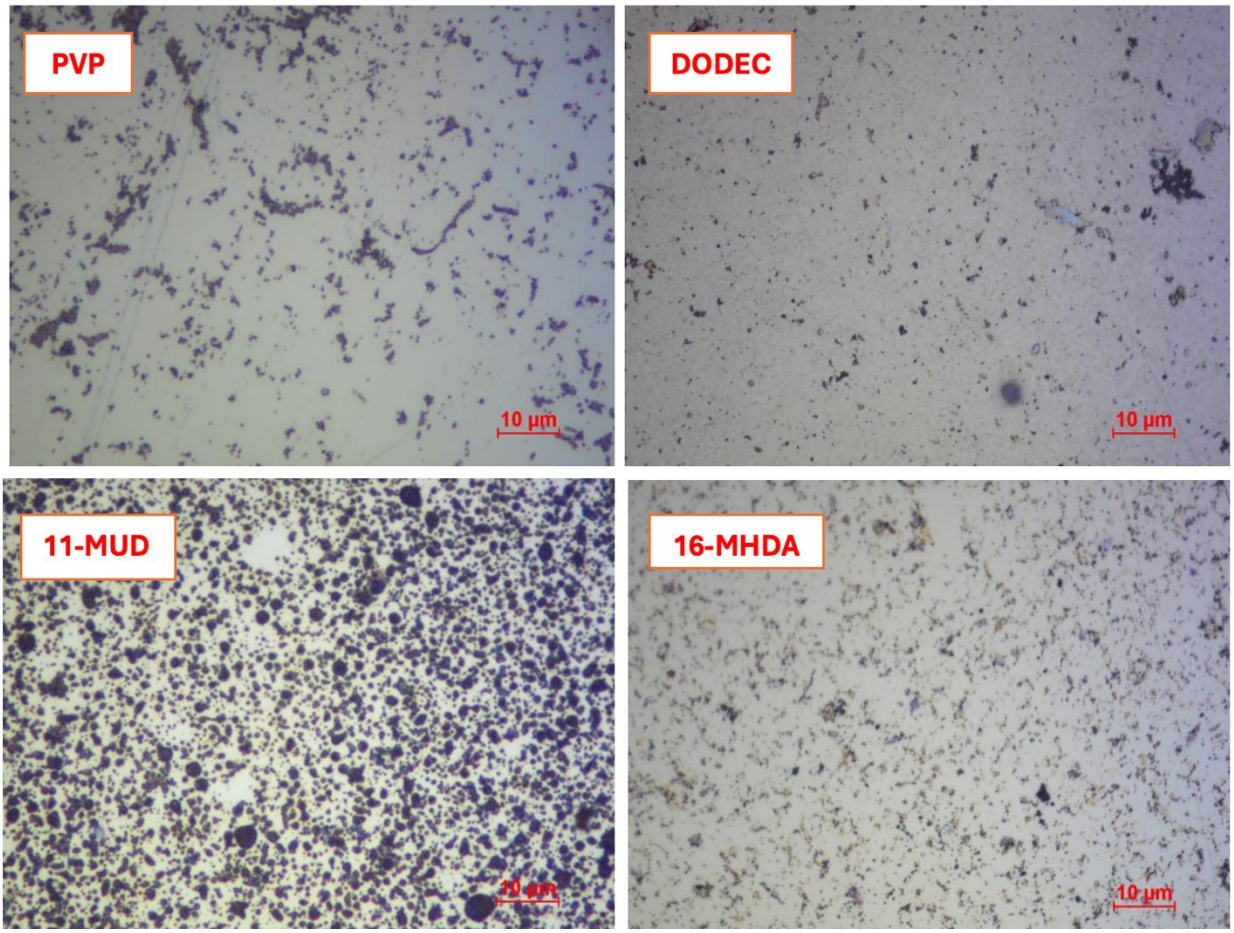

Figure 64: Light microscopy images (scale bar: 10 µm) of Au NPs capped with different ligands (PVP, 1-dodecanethiol, 11-MUD, 16-MHDA) dispersed in THF (2 mg/mL).

In conclusion, replacing the PVP layer with 16-MHDA on Au NPs, combined with the change in polymerization solvent from THF to DMSO, results in the successful imprinting of a monolayer of NPs through in-situ polymerization [134]. The use of DMSO as the solvent contributes to a more resistant and adherent polymer on the QCM substrate, as SEM and AFM analyses revealed. Notably, this facilitated template removal, especially for 16-MHDA capped Au NPs, attributed to increased repulsion between the MAA:TRIM polymer (ζ = -20 mV) and capped Au NPs (ζ = - 10 mV). Overall, these modifications enhanced the polymer characteristics and template removal efficiency in comparison to the PVP-capped counterparts. Figure 65 illustrates MIP

surface characterization incorporating Au NPs coated with 16-MHDA. The image shows even nanoparticle distribution and a homogeneous polymer surface, confirming successful imprinting of Au@16-MHDA within the MAA:TRIM polymer matrix.

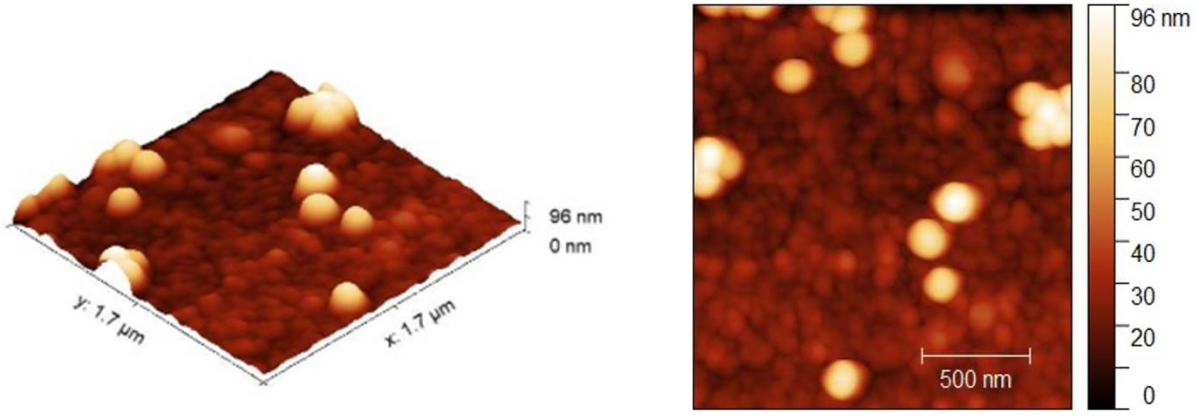

Figure 65: AFM images (contact mode) from MAA:TRIM MIP with Au@16-MHDA NPs in DMSO.

After polymerization, the MIP and NIP QCMs were washed with DMSO by stirring in a petri dish for 20 minutes, directly before drying and hardening, to enhance removal of both nanoparticles and unreacted components. For the second step, template extraction, the QCMs were dried at 80°C and then sonicated first in EtOH for 20 minutes, followed by 20 minutes in DMSO and finally stirred in dH_2O for 5 minutes.

Figure 66 shows that most of the nanoparticles have been removed. However, there is also a significant portion of the polymer layer detached from the QCM surface. To address this issue, the NHS:EDC ratio used during EDC/NHS coupling was modified from 4:6 to 8:6, resulting in improved initiator binding to the substrate and a more stable polymer layer [135-137].

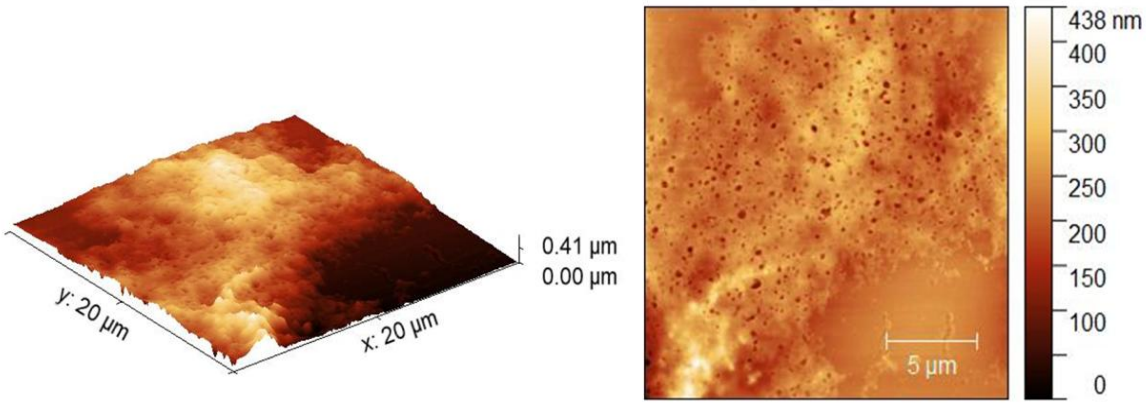

Figure 66: Polymer coverage on the QCM surface after sonication in EtOH and DMSO.

Figure 67 demonstrates SEM surface scans from different spots on the QCM confirming the remaining cavities on the MIP surface after extraction. Furthermore, it clearly shows that washing indeed removes most of the Au NPs. The cavities on MIP match the shape and size of the Au NPs used as the template.

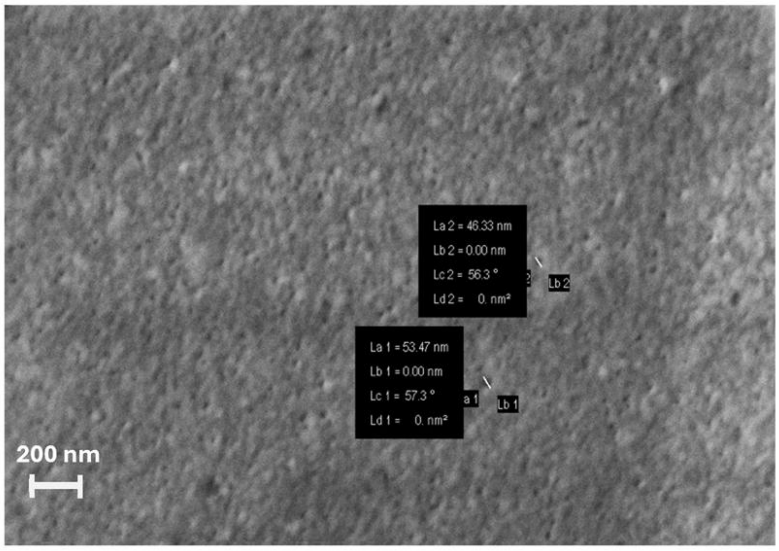

Figure 67: SEM image of the Au@16-MHDA MIP surface after nanoparticle extraction. The estimated cavity sizes range from 46 to 53 nm, which aligns well with the original size of the imprinted Au NPs.

5.2.5. Sensor Measurements

The MIP sensors prepared with Au@16-MHDA nanoparticles and their corresponding NIP were exposed to three concentrations (25, 50 and 100 µg/mL) of Au@16-MHDA in PBS (pH 7.4) as the background.

Figure 68 shows the QCM results of Au@16-MHDA nanoparticles (75 nm in size) on the MIP sensor. After the first injection of an analyte solution at c = 25 µg/mL, the frequency decreased by approximately 25 Hz and rinsing the MIPs with PBS partially brings signal back toward the baseline. Upon injecting c = 50 µg/mL of Au@16-MHDA NPs, the frequency shifted by 75 Hz. Injection of 100 µg/mL caused the frequency to shift slightly further to 100 Hz, which may indicate that the MIP sensors were already approaching saturation. This last concentration was tested twice at 100 µg/mL; during the second injection no further frequency change was observed.

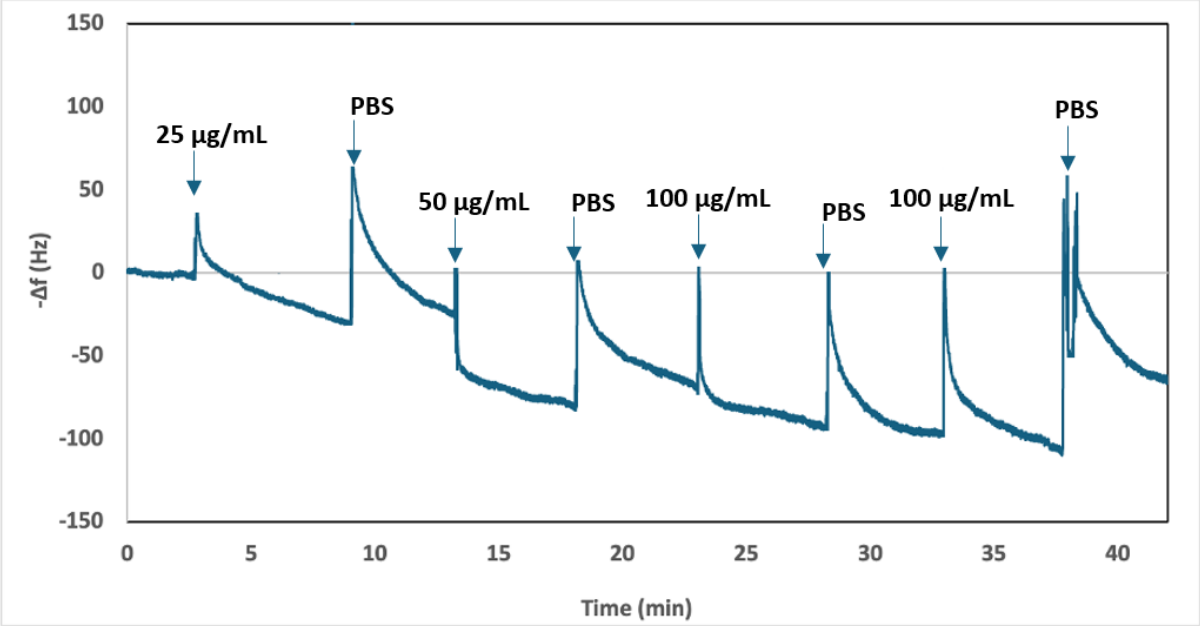

Figure 68: QCM sensor response of MIP on QCM towards c= 25, 50 and 100 µg/mL of Au@16-MHDA in solution in PBS (pH 7.4).

Figure 69 shows the responses of the NIP sensor to Au@16-MHDA at concentrations of 25, 50 and 100 µg/mL in PBS (pH 7.4). Each injection was repeated twice to ensure the reproducibility of the responses. None of the concentrations produced a notable response, which can be explained by the lack of affinity between the NIP surface and the nanoparticles.

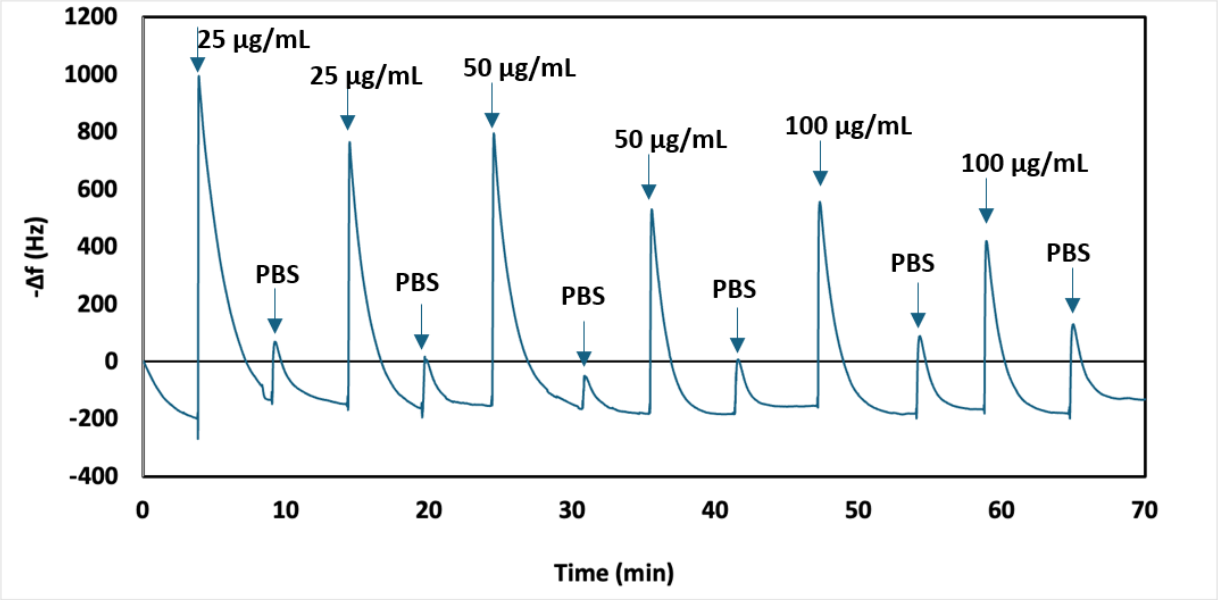

Figure 69: QCM sensor response of exposing NIP surfaces to 25, 50 and 100 µg/mL of Au@16-MHDA in PBS (pH 7.4).

Figure 70 shows AFM images of the MIP surface after QCM measurement, showing binding of Au@16-MHDA NPs within the imprinted cavities. The cavity profile confirms alignment with the nanoparticle size (~50 nm) and indicates a polymer film thickness of approximately 10 nm.

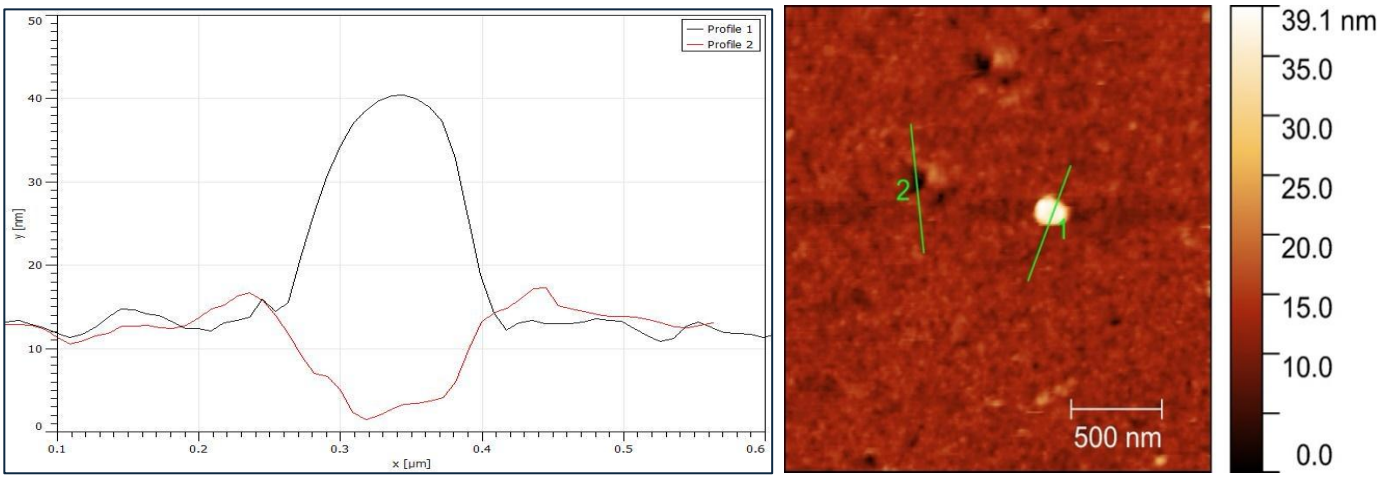

Figure 70: AFM image of MIP surface after rebinding of Au@16-MHDA NPs (right), profile of an empty cavity and Au@16-MHDA NPs binding into the respective cavity (left).

Figure 71 shows SEM images demonstrating clear binding of Au@16-MHDA NPs in the cavities on the MIP surface, while the NIP surface exhibits only a few nanoparticles, likely due to non-specific interactions. Some residual nanoparticles are still visible on the MIP surface prior to rebinding, possibly due to incomplete removal during the template extraction process. However, the number is not significant.

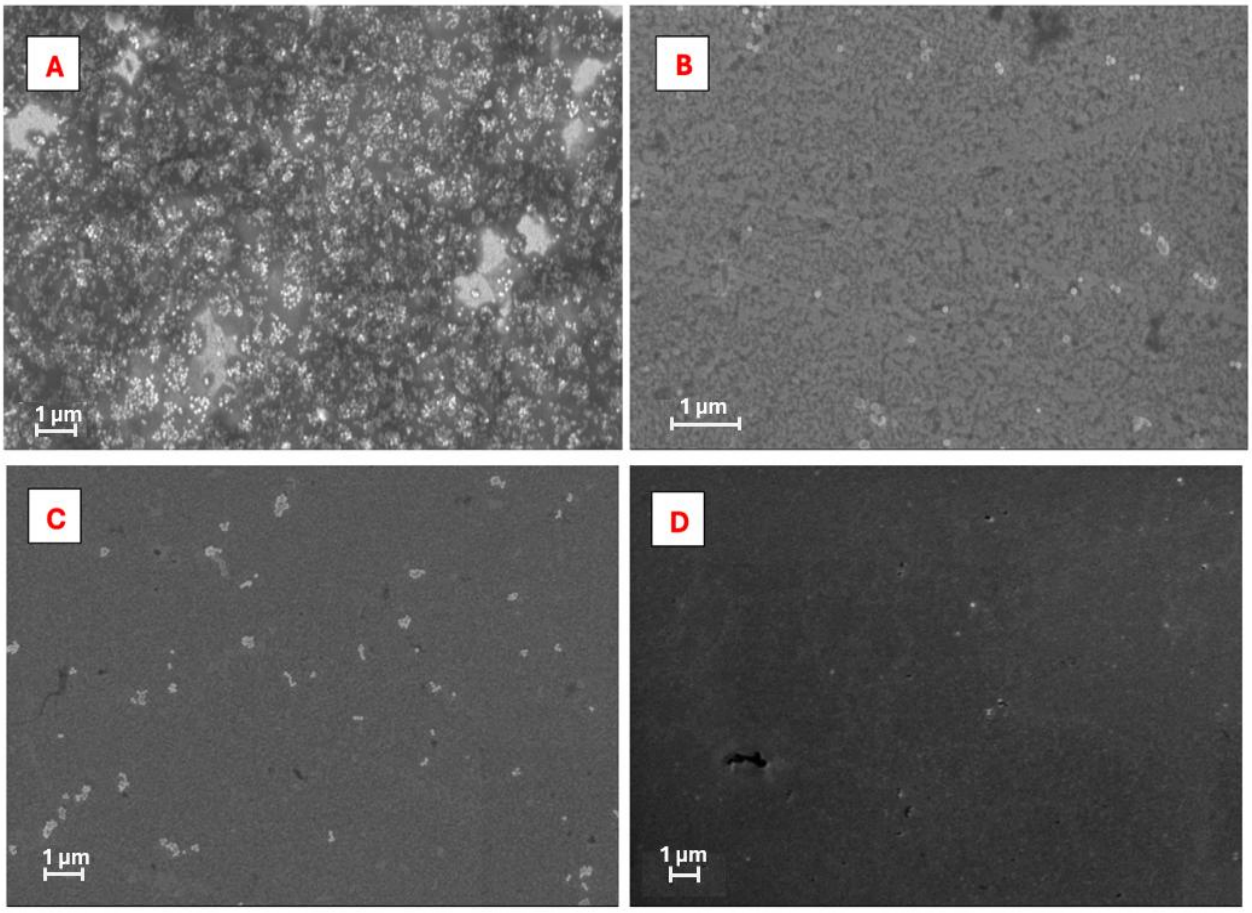

Figure 71: SEM images of MIP and NIP surfaces before and after exposure to Au@16-MHDA NPs. (A) MIP surface after rebinding Au@16-MHDA NPs. (B) MIP surface with cavities before rebinding. (C) NIP surface after injection of Au@16-MHDA NPs. (D) NIP surface before nanoparticle injection.

To test selectivity, the MIP QCM responses were evaluated using Au@PVP NPs at the same concentrations (25, 50, 100 µg/mL) as used for Au@16-MHDA in PBS (pH 7.4). As shown in Figure 72, each injection of Au@PVP NPs results in an inverse frequency shift, due to the non-specific interactions between the particles and the polymer surface. However, no stable binding is observed between the Au@PVP NPs and the imprinted cavities, thus confirming the selectivity of the MIP toward the originally imprinted Au@16-MHDA NPs.

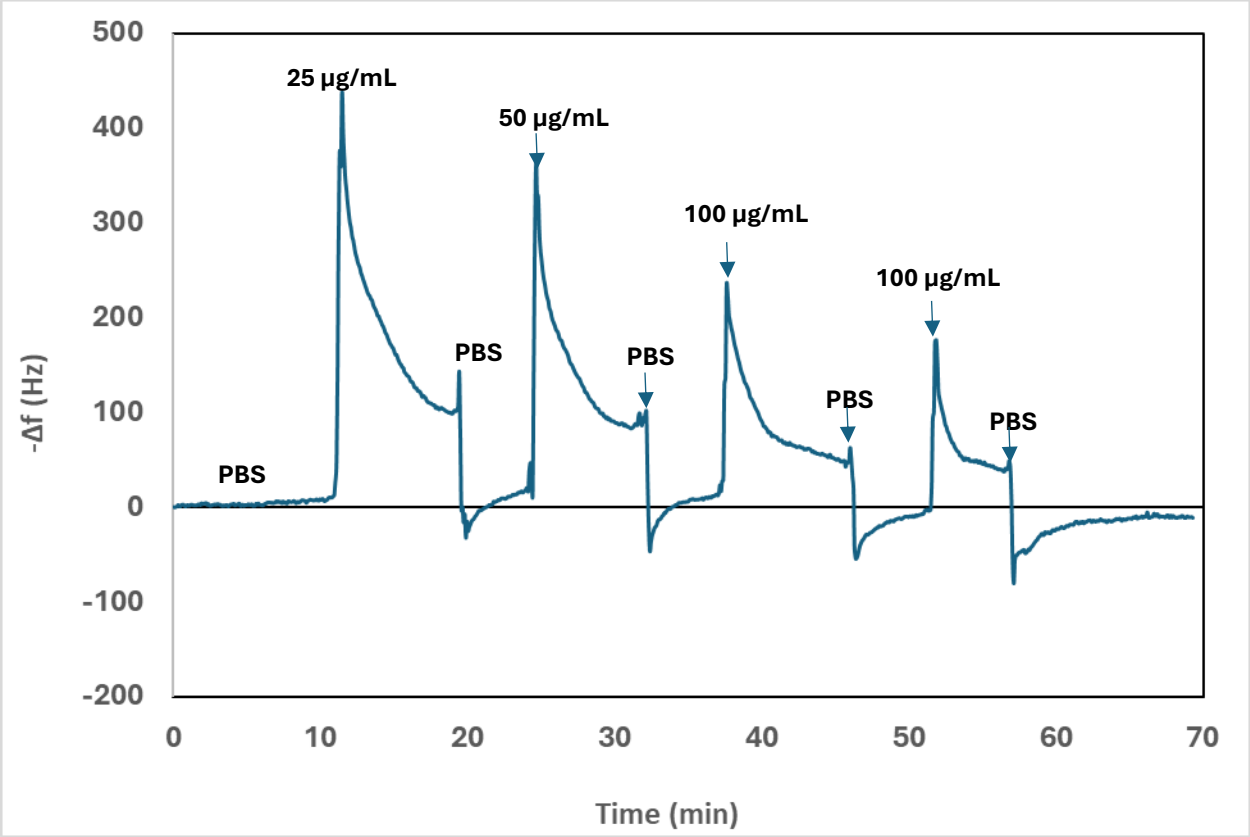

Figure 72: QCM responses of the MIP sensor exposed to Au@PVP NPs at concentrations of 25, 50 and 100 µg/mL.

Sensor Characterization in EtOH

As described earlier, the sensing measurements were initially performed in PBS (pH 7.4) as the background. However, the results did not show high sensitivity toward the analyte concentration. This might be due to poor dispersion of 16-MHDA-capped Au NPs in the buffer. To address this issue, the measurements were repeated with the same analyte concentrations (25, 50 and 100 µg/mL) in EtOH.

Figure 73 shows the binding affinity of MIP to Au@16-MHDA NPs dispersed in EtOH at different concentrations (25, 50 and 100 µg/mL). Upon analyte injection, the signal exhibited a large drift and then shifted toward more positive values. For example, at 25 µg/mL, the frequency first shifted to approximately –200 Hz, then stabilized at –50 Hz. At 100 µg/mL, the response reached

around –240 Hz. Washing the QCM with EtOH after each analyte injection did not result in any frequency shift toward more positive values, indicating highly binding of Au NPs to the MIP.

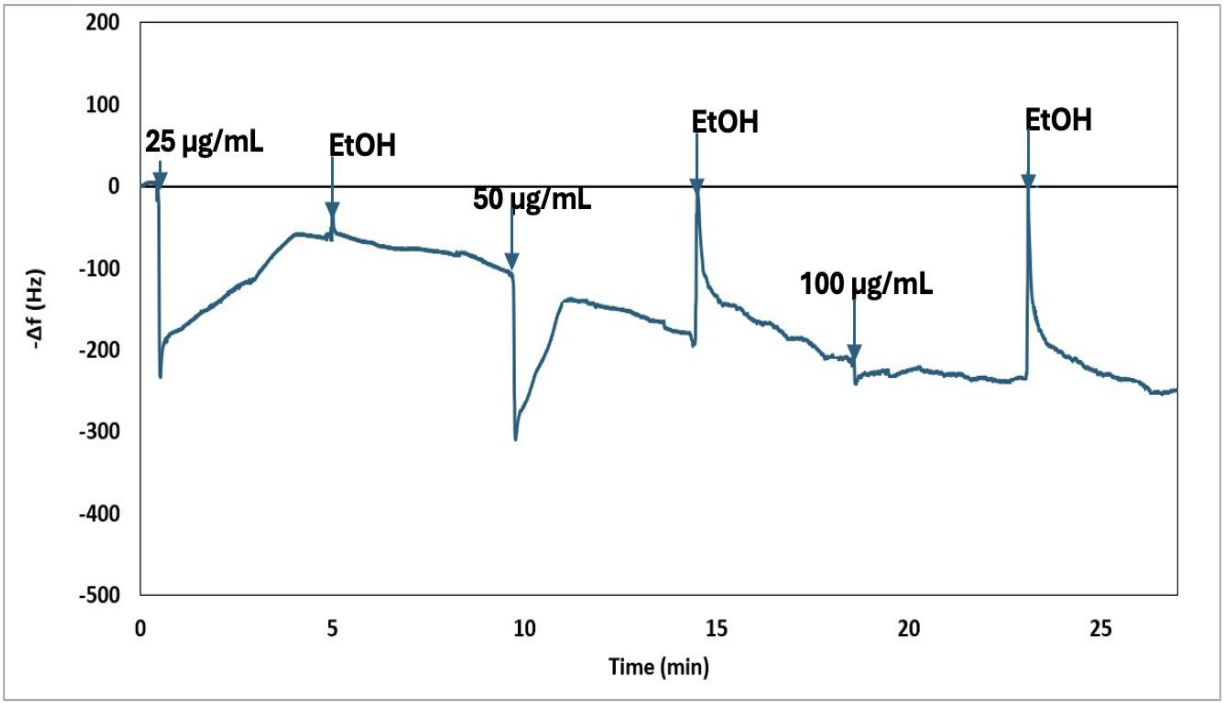

Figure 73: QCM MIP sensor responses to c= 25, 50 and 100 µg/mL 0f Au@16-MHDA in EtOH.

Figure 74 displays the outcomes of exposing NIP to concentrations of 25, 50 and 100 µg/mL of Au@16-MHDA solution in EtOH. Although frequency shifts were observed after injecting 50 µg/mL (–50 Hz) and 100 µg/mL (–20 Hz), the signal returned to the baseline after washing with EtOH, resulting in a final frequency change of zero. This indicates no specific binding affinity of Au NPs toward the NIP.

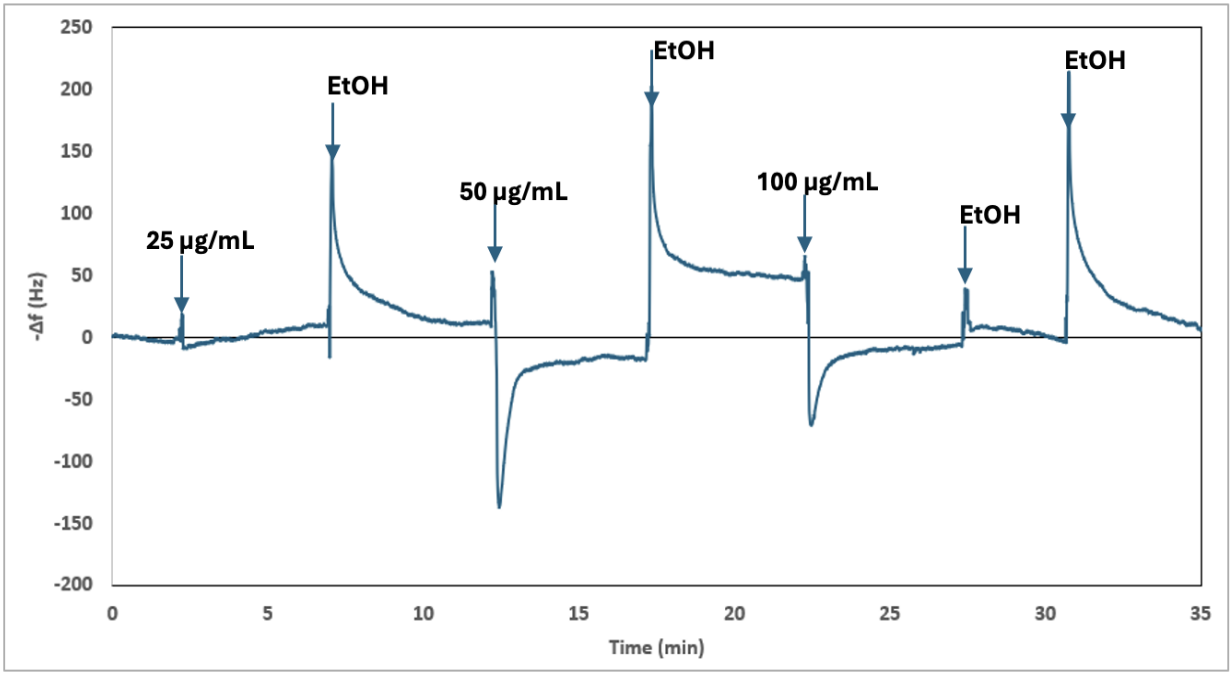

Figure 74: QCM sensor response of NIP on QCM towards c= 25, 50 and 100 µg/mL 0f Au@16-MHDA in EtOH.

As Figure 75 illustrates the responses of sensing measurements with Au NPs dispersed in EtOH compared to PBS. At 25 and 50 µg/mL, the responses in EtOH are almost twice as high as those in PBS. At 100 µg/mL, the MIP response in EtOH reaches –240 Hz, whereas in PBS, after washing, the signal shifts from –110 Hz to –70 Hz. Overall, comparing the responses of MIP toward Au@16-MHDA NPs in different media (PBS and EtOH) highlights the significant influence of nanoparticle dispersion on the sensor response.

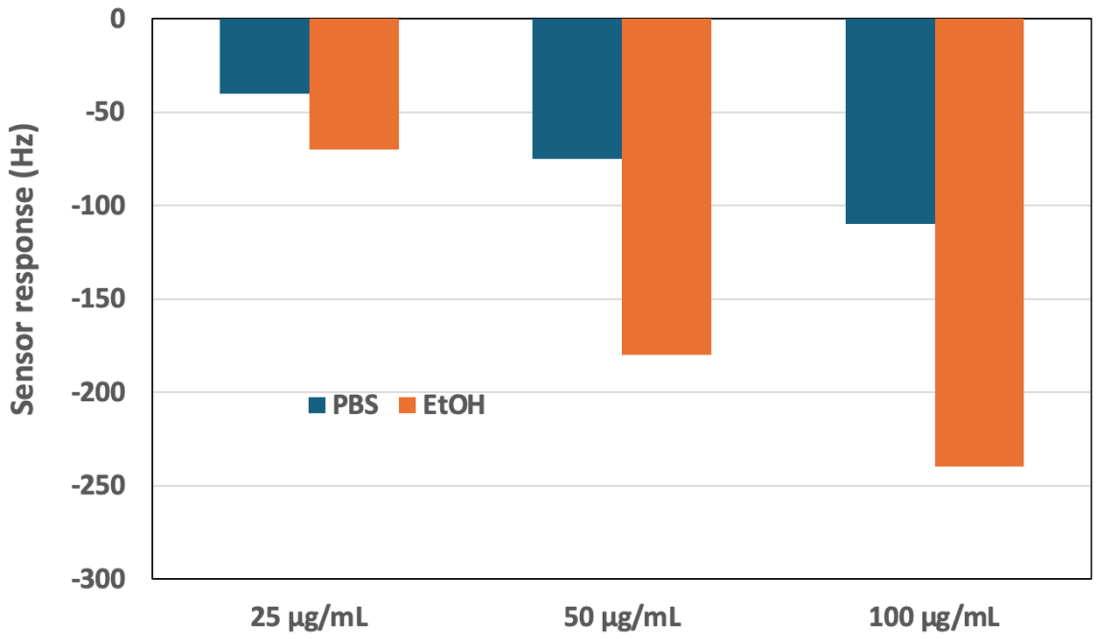

Figure 75: Sensitivity assessment of the MIP against Au@16-MHDA NPs in PBS and EtOH at three concentrations (25, 50 and 100 µg/mL).

The selectivity of the MIP toward different stabilizers, 16-MHDA versus PVP, was studied in EtOH. Figure 76 shows that the MIP sensor responses are significantly lower for PVP-capped Au NPs compared to the imprinted 16-MHDA-capped Au NPs. For all tested concentrations of PVP@Au NPs (25, 50 and 100 µg/mL), the responses remained around –50 Hz. After washing with EtOH following the last injection, the frequency almost returned to the baseline, with a total change of approximately –20 Hz. Importantly, the calculated SF of 20 indicates the excellent selectivity of MIP, which clearly distinguishes between its specific affinity for 16-MHDA and negligible non-specific interactions with PVP, thus confirming the high detection capability of the sensor in the comparative assay.

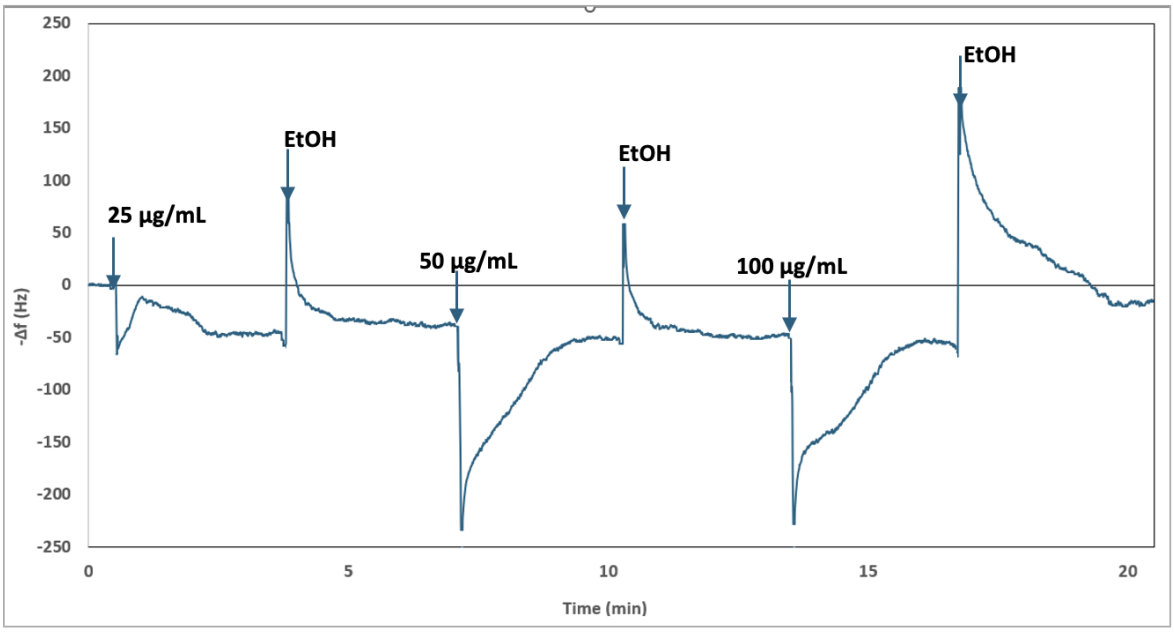

Figure 76: QCM MIP sensor responses to c= 25, 50 and 100 µg/mL 0f Au@PVP NPs in EtOH.

When comparing PBS and EtOH as backgrounds in terms of selectivity, it was observed that in PBS, the responses toward the PVP stabilizer were inverse, as shown in the previous Figure 72. However, in both solvents there is no specific binding between MIP and PVP-coated gold nanoparticles, and MIP shows selectivity towards gold nanoparticles with different outer stabilizing layers.

5.3. Summary and Conclusion

In conclusion, Au NPs (75 nm in size) are successfully imprinted into MIPs using in-situ polymerization. The initial phase of the work involves in-situ polymerization on QCM chips, using MAA as the monomer and TRIM as the cross-linker. The photo-initiator AAPH is covalently immobilized on the QCM surface via surface-initiated RAFT polymerization, ensuring controlled polymer growth and uniform film formation. This process yields an optimal film thickness of 15–20 nm, sufficient for embedding and stabilizing Au NPs while allowing efficient removal.

Even with a reduction in polymer thickness, extraction of Au@PVP nanoparticles from the resulting polymer matrix is initially unsuccessful. Therefore, various thiol-functionalized ligands 11-MUD, 16-MHDA and 1-dodecanethiol with different degrees of hydrophilicity are used to replace the PVP coating. Zeta potential, hydrodynamic size analyses and UV-vis absorption measurements of the nanoparticles confirm the successful replacement of PVP with the new stabilizers. Among these, 16-MHDA proves to be the most effective for nanoparticle removal, producing a more negative surface charge compared to the other capped nanoparticles. This increased negative surface charge enhances repulsion from the deprotonated poly (MAA:TRIM) matrix, which exhibits a predominantly negative zeta potential of around –20 mV at neutral and basic pH.

Sensor performance tests of MIP- and NIP-coated QCMs with varying concentrations of Au@16-MHDA (25, 50 and 100 µg/mL in PBS) show concentration-dependent frequency shifts (up to ~–100 Hz in total) with minimal reversibility. However, this response does not indicate strong binding, likely due to aggregation of the 16-MHDA-capped particles in water. In contrast, the NIP sensors exhibit non-significant frequency shifts, suggesting no specific interactions.

AFM and SEM analyses provide visual confirmation of successful imprinting and extraction. Further AFM imaging reveals that nanoparticle rebinding occurs specifically within the imprinted cavities, demonstrating the selective recognition capability of the MIP sensors.

Selectivity is further confirmed through testing with competitive nanoparticles (Au@PVP). These particles produce inconsistent and reversible frequency shifts, indicating that they do not fit the imprinted cavities. This strongly supports the sensor's ability to distinguish between similarly sized but chemically distinct nanoparticle targets.

Moreover, changing the solution from PBS to EtOH causes a significant difference in the sensitivity of the MIP due to the different distribution behavior of Au@16-MHDA resulting from the distinct hydrophilicity of the solvents. The responses increase from –110 Hz in PBS to –240 Hz in EtOH at 100 µg/mL of analyte.

This study presents several important findings. First, it confirms that molecular imprinting on metal nanoparticles using surface-initiated polymerization is not only possible but also adjustable through controlled chemical and physical conditions. Second, the surface properties of the nanoparticles significantly influence both template removal and overall sensor performance. The type of stabilizer used plays a critical role in particle and polymer interactions, dispersion stability and the fidelity of the imprinted cavities. Third, fine-tuning polymer thickness, initiator attachment methods and template removal processes are essential to achieve consistent and sensitive sensor responses.

Overall, this work introduces a novel approach for creating MIP-based sensors using Au NPs as templates. While the resulting system does not exhibit strong selectivity, it demonstrates measurable sensitivity toward the target analyte, providing a solid foundation for future sensor development in medical and environmental applications.

6. Conclusions and Outlook

This thesis has developed molecularly imprinted polymer (MIP) sensors for two distinct targets: Penicillin V potassium (Pen VK) and gold nanoparticles (Au NPs), each requiring specific imprinting strategies and posing unique challenges. In this study, acrylic-based polymers are employed, primarily using acrylic acid (AA) and methacrylic acid (MAA) as functional monomers, with trimethylolpropane trimethacrylate (TRIM) as the main cross-linker. At certain stages, ethylene glycol dimethacrylate (EGDMA) is introduced as a compatible co-cross-linker to optimize polymer properties.

For the detection of Pen VK, precipitation polymerization produces polymer nanoparticles, which are subsequently applied to QCM and acoustic sensors for testing. Optimized template removal improves the accessibility of recognition sites. Sensor measurements reveal a clear, concentration-dependent and reversible response, with MIP compared to corresponding NIP. Incorporating a co-monomer and co-cross-linker system further enhances binding performance but makes precise nanoparticle size control more challenging. Size control strongly depends on polymerization conditions and consistent particle dimensions are essential for compatibility with commercial sensor chips, where strict size specifications must be met to satisfy market demand. This remains a key challenge and future work should focus on refining the synthesis process to achieve both high performance and dimensional uniformity.

In the second part of the work, surface imprinting techniques are employed to fabricate thin, selective recognition layers directly on sensor surfaces for Au NP detection. Morphological characterization by atomic force microscopy (AFM) and scanning electron microscopy (SEM) confirms the presence of well-defined imprinted cavities. However, the high affinity of Au NPs for the polymer surface complicates template removal. To address this, different capping layers are tested; however, these changes cause pronounced aggregation of the nanoparticles during measurement. This aggregation hinders diffusion into the imprinted sites, reduces reproducibility and limits overall sensing performance. Future work should focus on finding stabilizing strategies

that allow both efficient template removal and long-term colloidal stability, as well as optimizing imprinting conditions to prevent aggregation during sensing.

Taken together, the results of this thesis demonstrate both the versatility and the challenges of MIP-based sensing for chemically and physically diverse targets. While the Pen VK sensors highlight the potential for achieving high sensitivity and selectivity in pharmaceutical detection, the Au NP system emphasizes the importance of surface chemistry control in nanoparticle-based analyte sensing. With continued advances in polymer chemistry, nano structuring techniques and template removal strategies, MIP sensors can become a viable platform for a wide range of analytical applications, from environmental monitoring to biomedical diagnostics. The insights gained here provide a strong foundation for such future developments, paving the way toward robust, reproducible and application-ready sensing devices.

Abstract

This thesis presents the synthesis and characterization of molecularly imprinted polymers (MIPs) designed for selective detection of analytes, with binding affinities evaluated using quartz crystal microbalance (QCM) measurements. Acrylic-based MIPs were prepared using methacrylic acid (MAA) as the functional monomer and ethylene glycol dimethacrylate (EGDMA) or trimethylolpropane trimethacrylate (TRIM) as cross-linkers. The first target analyte was penicillin VK, investigated within the FFG-funded AquaNose project, aiming to develop an MIP sensor for its detection in wastewater. This section focuses on the morphology and size distribution of polymeric nanoparticles. Binding affinity was optimized by testing different monomers and cross-linkers. Results showed that introducing a co-monomer improved the limit of detection (LoD) from 1.53 mM for MAA to 0.38 mM for MAA:AA (0.7:0.3). Moreover, TRIM not only yielded more uniform nanoparticles but also enhanced selectivity, with factors of 2 against penicillin GK and 4 against Amo Na.

The second part of the thesis focuses on in-situ polymerization by immobilizing the initiator AAPH onto the QCM gold surface. Homogeneous and uniform polymer films were further achieved using RAFT-controlled radical polymerization. Gold nanoparticle (Au NP) removal efficiency was improved by varying surface functionalization, with 16-MHDA showing the best performance. QCM measurements demonstrated selective recognition of MIPs toward PVP-functionalized Au NPs differently functionalized surfaces, achieving a selectivity factor of 20 for PVP-functionalized Au NPs.

All materials were characterized using light microscopy, atomic force microscopy (AFM, tapping and contact mode), scanning electron microscopy (SEM) and attenuated total reflection infrared spectroscopy (ATR-IR).

Zusammenfassung

Diese Dissertation beschreibt die Synthese und Charakterisierung molekular geprägter Polymere (MIPs), die für die selektive Detektion von Analyten entwickelt wurden. Die Bindungsaffinitäten wurden mittels Quarzkristallmikrowaage (QCM) untersucht. Acrylbasierte MIPs wurden unter Verwendung von Methacrylsäure (MAA) als funktionellem Monomer sowie Ethylenglycoldimethacrylat (EGDMA) oder Trimethylolpropantrimethacrylat (TRIM) als Vernetzer hergestellt. Der erste Zielanalyt war Penicillin VK, untersucht im Rahmen des FFG-geförderten *AquaNose*-Projekts, mit dem Ziel, einen MIP-Sensor zur Erkennung von Penicillin VK in Abwasser zu entwickeln. Dieser Teil konzentriert sich auf die Morphologie und Größenverteilung der polymeren Nanopartikel. Die Bindungsaffinität wurde durch den Einsatz verschiedener Monomere und Vernetzer optimiert. Die Ergebnisse zeigen, dass die Einführung eines Co-Monomers die Nachweisgrenze (LoD) von 1,53 mM (MAA) auf 0,38 mM (MAA:AA, 0,7:0,3) verbessern konnte. Zudem führte der Einsatz von TRIM nicht nur zu regelmäßigeren Nanopartikelstrukturen, sondern auch zu einer erhöhten Selektivität, mit Faktoren von 2 gegenüber Penicillin GK und 4 gegenüber Amo Na.

Der zweite Teil der Arbeit befasste sich mit der in-situ-Polymerisation durch Immobilisierung des Initiators AAPH auf der Goldoberfläche des QCM. Homogene und gleichmäßige Polymerfilme konnten zusätzlich durch RAFT-kontrollierte radikalische Polymerisation erzeugt werden. Die Effizienz der Entfernung von Goldnanopartikeln (Au NPs) wurde durch unterschiedliche Oberflächenfunktionalisierungen verbessert, wobei 16-MHDA die besten Ergebnisse erzielte. QCM-Messungen zeigten eine spezifische Erkennung der MIPs gegenüber verschieden funktionalisierten Oberflächen, mit einem Selektivitätsfaktor von 20 für PVP-funktionalisierte Au NPs.

Die Charakterisierung erfolgte mittels Lichtmikroskopie, Rasterkraftmikroskopie (AFM, Tapping- und Kontaktmodus), Rasterelektronenmikroskopie (REM) sowie Infrarotspektroskopie mit abgeschwächter Totalreflexion (ATR-IR).

75 nm PVP Econix Gold

Lot Number: IXW0067

Diameter (TEM):	76.31 ± 12.61 nm	**Hydrodynamic Diameter:**	107.7 nm
Coefficient of Variation:	16.5 %	**Zeta Potential:**	-28.3 mV
Surface Area (TEM):	3.87 m^2/g	**pH of Solution:**	6.4
Mass Concentration (Au):	5.27 mg/mL	**Particle Surface:**	PVP
Particle Concentration:	1.1E+12 particles/mL	**Solvent:**	Milli-Q Water

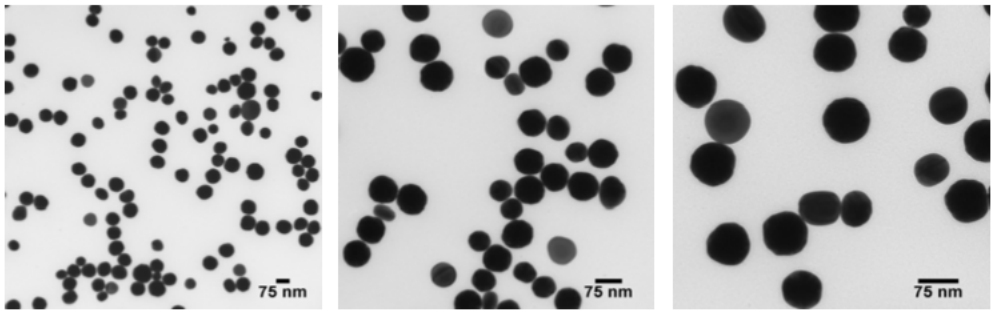

Size Distribution

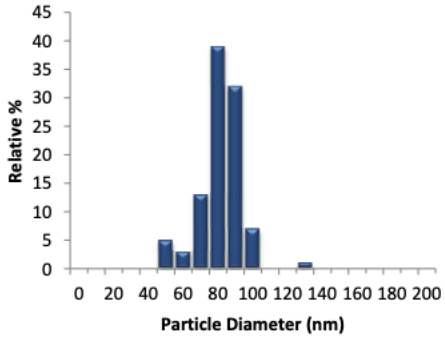

Optical Properties

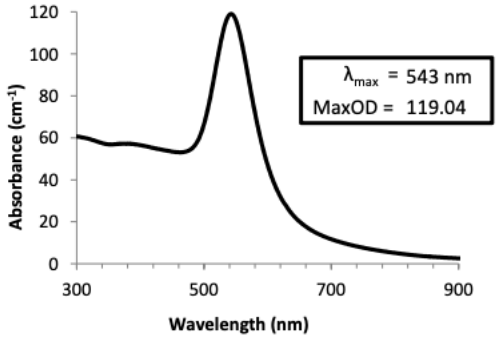

Characterization Instrumentation

Diameter and Size Statistics:	JEOL 1010 Transmission Electron Microscope
Mass Concentration:	Thermo Fisher X Series 2 ICP-MS
Spectral Properties:	Agilent 8453 UV-Visible Spectrometer
Hydrodynamic Diameter/Zeta Potential:	Malvern Zetasizer Nano ZS.

Storage and Handling: 4 °C away from light. DO NOT FREEZE.

nanoComposix, Inc
4878 Ronson Ct. Suite K
San Diego, CA 92111

For more information visit: www.nanocomposix.com

support@nanocomposix.com
Phone: (858) 565-4227
Fax: (619) 330-2556

References

1 Haghdoust, S., Arshad, U., Mujahid, A., Schranzhofer, L. & Lieberzeit, P. A. Development of a MIP-Based QCM Sensor for Selective Detection of Penicillins in Aqueous Media. *Chemosensors* **9** (2021). https://doi.org:10.3390/chemosensors9120362

2 Lieberzeit, P. A., Jungmann, C. & Schranzhofer, L. Molecular Imprinting on the Nanoscale – Rapid Detection of Ag Nanoparticles by QCM Sensors. *Procedia Engineering* **87**, 236-239 (2014). https://doi.org:10.1016/j.proeng.2014.11.630

3 Hernando, M. D., Mezcua, M., Fernandez-Alba, A. R. & Barcelo, D. Environmental risk assessment of pharmaceutical residues in wastewater effluents, surface waters and sediments. *Talanta* **69**, 334-342 (2006). https://doi.org:10.1016/j.talanta.2005.09.037

4 Kümmerer, K. Pharmaceuticals in the Environment. *Annual Review of Environment and Resources* **35**, 57-75 (2010). https://doi.org:10.1146/annurev-environ-052809-161223

5 Lalchhandama, K. History of penicillin. *WikiJournal of Medicine* **8**, 1-16 (2021).

6 Etebu, E. & Arikekpar, I. Antibiotics: Classification and mechanisms of action with emphasis on molecular perspectives. *Int. J. Appl. Microbiol. Biotechnol. Res* **4**, 90-101 (2016).

7 Barton, M. D. Antibiotic use in animal feed and its impact on human healt. *Nutrition research reviews* **13**, 279-299 (2000). https://doi.org/10.1079/095442200108729106

8 Low, C. X. *et al.* Unveiling the impact of antibiotics and alternative methods for animal husbandry: A review. *Antibiotics* **10**, 578 (2021). https://doi.org/10.3390/antibiotics10050578

9 Lima, L. M., Silva, B., Barbosa, G. & Barreiro, E. J. beta-lactam antibiotics: An overview from a medicinal chemistry perspective. *Eur J Med Chem* **208**, 112829 (2020). https://doi.org:10.1016/j.ejmech.2020.112829

10 Apreja, M. *et al.* Antibiotic residues in environment: antimicrobial resistance development, ecological risks and bioremediation. *Environ Sci Pollut Res Int* **29**, 3355-3371 (2022). https://doi.org:10.1007/s11356-021-17374-w

11 Werkneh, A. A. & Islam, M. A. Post-treatment disinfection technologies for sustainable removal of antibiotic residues and antimicrobial resistance bacteria from hospital wastewater. *Heliyon* **9**, e15360 (2023). https://doi.org:10.1016/j.heliyon.2023.e15360

12 Klein, E. Y. *et al.* Global trends in antibiotic consumption during 2016-2023 and future projections through 2030. *Proc Natl Acad Sci U S A* **121**, e2411919121 (2024). https://doi.org:10.1073/pnas.2411919121

13 Mulchandani, R. *et al.* Global trends in inappropriate use of antibiotics, 2000-2021: scoping review and prevalence estimates. *BMJ Public Health* **3**, e002411 (2025). https://doi.org:10.1136/bmjph-2024-002411

14 Zaman, S. B. *et al.* A Review on Antibiotic Resistance: Alarm Bells are Ringing. *Cureus* **9**, e1403 (2017). https://doi.org:10.7759/cureus.1403

15 Zhang, L. *et al.* Occurrence, removal, emission and environment risk of 32 antibiotics and metabolites in wastewater treatment plants in Wuhu, China. *Sci Total Environ* **899**, 165681 (2023). https://doi.org:10.1016/j.scitotenv.2023.165681

16 Rossmann, J., Schubert, S., Gurke, R., Oertel, R. & Kirch, W. Simultaneous determination of most prescribed antibiotics in multiple urban wastewater by SPE-LC-MS/MS. *J Chromatogr B Analyt Technol Biomed Life Sci* **969**, 162-170 (2014). https://doi.org:10.1016/j.jchromb.2014.08.008

17 Tong, L., Li, P., Wang, Y. & Zhu, K. Analysis of veterinary antibiotic residues in swine wastewater and environmental water samples using optimized SPE-LC/MS/MS. *Chemosphere* **74**, 1090-1097 (2009). https://doi.org:10.1016/j.chemosphere.2008.10.051

18 Yevenes, K. *et al.* Detection of Antimicrobial Residues in Poultry Litter: Monitoring a Risk through a Selective and Sensitive HPLC-MS/MS Method. *Animals (Basel)* **11** (2021). https://doi.org:10.3390/ani11051399
19 Christian, T. *et al.* Determination of Antibiotic Residues in Manure, Soil and Surface Waters. *Acta hydrochimica et hydrobiologica* **31**, 36-44 (2003). https://doi.org:10.1002/aheh.200390014
20 Pennacchio, A. *et al.* A novel fluorescence polarization assay for determination of penicillin G in milk. *Food Chem* **190**, 381-385 (2016). https://doi.org:10.1016/j.foodchem.2015.05.127
21 Pollap, A. & Kochana, J. Electrochemical Immunosensors for Antibiotic Detection. *Biosensors (Basel)* **9** (2019). https://doi.org:10.3390/bios9020061
22 Wang, L., Pagett, M. & Zhang, W. Molecularly imprinted polymer (MIP) based electrochemical sensors and their recent advances in health applications. *Sensors and Actuators Reports* **5** (2023). https://doi.org:10.1016/j.snr.2023.100153
23 Zhang, X. *et al.* in *Trends in Biosensing Research: Advances, Challenges and Applications* (eds Fred Lisdat & Nicolas Plumeré) 107-148 (Springer International Publishing, 2024).
24 Elveny, M., Khan, A., Nakhjiri, A. T. & Albadarin, A. B. A state-of-the-art review on the application of various pharmaceutical nanoparticles as a promising technology in cancer treatment. *Arabian Journal of Chemistry* **14** (2021). https://doi.org:10.1016/j.arabjc.2021.103352
25 Kuppusamy, P. *et al.* In Vitro Anticancer Activity of Au, Ag Nanoparticles Synthesized Using Commelina nudiflora L. Aqueous Extract Against HCT-116 Colon Cancer Cells. *Biol Trace Elem Res* **173**, 297-305 (2016). https://doi.org:10.1007/s12011-016-0666-7
26 Rabiei, M., Kashanian, S., Samavati, S. S., Jamasb, S. & McInnes, S. J. P. Nanomaterial and advanced technologies in transdermal drug delivery. *J Drug Target* **28**, 356-367 (2020). https://doi.org:10.1080/1061186X.2019.1693579
27 Her, S., Jaffray, D. A. & Allen, C. Gold nanoparticles for applications in cancer radiotherapy: Mechanisms and recent advancements. *Adv Drug Deliv Rev* **109**, 84-101 (2017). https://doi.org:10.1016/j.addr.2015.12.012
28 Dubsok, A., Khamdahsag, P. & Kittipongvises, S. Life cycle environmental impact assessment of cyanate removal in mine tailings wastewater by nano-TiO2/FeCl3 photocatalysis. *Journal of Cleaner Production* **366** (2022). https://doi.org:10.1016/j.jclepro.2022.132928
29 Hund-Rinke, K. *et al.* Nanopharmaceuticals (Au-NPs) after use: Experiences with a complex higher tier test design simulating environmental fate and effect. *Ecotoxicol Environ Saf* **227**, 112949 (2021). https://doi.org:10.1016/j.ecoenv.2021.112949
30 Kus-Liskiewicz, M., Fickers, P. & Ben Tahar, I. Biocompatibility and Cytotoxicity of Gold Nanoparticles: Recent Advances in Methodologies and Regulations. *Int J Mol Sci* **22** (2021). https://doi.org:10.3390/ijms222010952
31 Carnovale, C., Bryant, G., Shukla, R. & Bansal, V. Identifying Trends in Gold Nanoparticle Toxicity and Uptake: Size, Shape, Capping Ligand and Biological Corona. *ACS Omega* **4**, 242-256 (2019). https://doi.org:10.1021/acsomega.8b03227
32 Schlich, K. *et al.* Microbial Population Dynamics in Model Sewage Treatment Plants and the Fate and Effect of Gold Nanoparticles. *Toxics* **9** (2021). https://doi.org:10.3390/toxics9030054
33 Gkika, D. A. *et al.* Application of molecularly imprinted polymers (MIPs) as environmental separation tools. *RSC Applied Polymers* **2**, 127-148 (2024). https://doi.org:10.1039/d3lp00203a
34 Garg, M. & Pamme, N. Strategies to remove templates from molecularly imprinted polymer (MIP) for biosensors. *TrAC Trends in Analytical Chemistry* **170** (2024). https://doi.org:10.1016/j.trac.2023.117437
35 Wei, C. *et al.* Application of Molecularly Imprinted Polymers in the Analysis of Explosives. *Polymers* **17**, 1410 (2025). https://doi.org/10.3390/polym17101410

36 P. A. Lieberzeit and J. Wackerlig. polymers, Molecularly Imprinted. *Ullmann's Encycl. Ind. Chem* **61**, 79-86 (2016). https://doi.org:10.1002/14356007.q21_q01

37 Wong, A., De Oliveira, F. M., Tarley, C. R. T. & Sotomayor, M. D. P. T. Study on the cross-linked molecularly imprinted poly (methacrylic acid) and poly (acrylic acid) towards selective adsorption of diuron. *Reactive and Functional Polymers* **100**, 26-36 (2016). https://doi.org/10.1016/j.reactfunctpolym.2016.01.006

38 Sahiner, N. & Yasar, A. O. Monodispersed p (2-VP) and p (2-VP-co-4-VP) particle preparation and their use as template for metal nanoparticle and as catalyst for H2 production from NaBH4 and NH3BH3 hydrolysis. *International journal of hydrogen energy* **39**, 10476-10484 (2014). https://doi.org/10.1016/j.ijhydene.2014.04.214

39 Guc, M. & Schroeder, G. The molecularly imprinted polymers. influence of monomers on the properties of polymers-a review. *World Journal of Research and Review* **5**, 262721 (2017).

40 Vasapollo, G. *et al.* Molecularly imprinted polymers: present and future prospective. *International journal of molecular sciences* **12**, 5908-5945 (2011). https://doi.org/10.3390/ijms12095908

41 Es-Haghi, H., Bouhendi, H., Marandi, G. B., Zohurian-Mehr, M. & Kabiri, K. Rheological properties of microgel prepared with long-chain crosslinkers by a precipitation polymerization method. *Journal of Macromolecular Science, Part B* **51**, 880-896 (2012). https://doi.org/10.1080/00222348.2011.610232

42 Mane, S., Ponrathnam, S. & Chavan, N. Role of interfacial tension of solvating diluents and hydrophilic–hydrophobic cross-Linkers in hyper-cross-linked solid supports. *Industrial & Engineering Chemistry Research* **54**, 6893-6901 (2015).

43 Li, Z. *et al.* Preparation of magnetic molecularly imprinted polymers with double functional monomers for the extraction and detection of chloramphenicol in food. *J Chromatogr B Analyt Technol Biomed Life Sci* **1100-1101**, 113-121 (2018). https://doi.org:10.1016/j.jchromb.2018.09.032

44 Thach, U. D., Nguyen Thi, H. H., Pham, T. D., Mai, H. D. & Nhu-Trang, T. T. Synergetic Effect of Dual Functional Monomers in Molecularly Imprinted Polymer Preparation for Selective Solid Phase Extraction of Ciprofloxacin. *Polymers (Basel)* **13** (2021). https://doi.org:10.3390/polym13162788

45 Niu, J., Du, M., Wu, W., Yang, J. & Chen, Q. Advances in the selection of functional monomers for molecularly imprinted polymers: A review. *J Sep Sci* **47**, e2400353 (2024). https://doi.org:10.1002/jssc.202400353

46 Muhammad, T. *et al.* Rational design and synthesis of water-compatible molecularly imprinted polymers for selective solid phase extraction of amiodarone. *Anal Chim Acta* **709**, 98-104 (2012). https://doi.org:10.1016/j.aca.2011.10.009

47 Parkatzidis, K., Wang, H. S., Truong, N. P. & Anastasaki, A. Recent Developments and Future Challenges in Controlled Radical Polymerization: A 2020 Update. *Chem* **6**, 1575-1588 (2020). https://doi.org:10.1016/j.chempr.2020.06.014

48 Speltini, A., Scalabrini, A., Maraschi, F., Sturini, M. & Profumo, A. Newest applications of molecularly imprinted polymers for extraction of contaminants from environmental and food matrices: A review. *Anal Chim Acta* **974**, 1-26 (2017). https://doi.org:10.1016/j.aca.2017.04.042

49 Farooq, S. *et al.* Molecularly imprinted polymers' application in pesticide residue detection. *Analyst* **143**, 3971-3989 (2018). https://doi.org:10.1039/c8an00907d

50 Metwally, M. G., Benhawy, A. H., Khalifa, R. M., El Nashar, R. M. & Trojanowicz, M. Application of Molecularly Imprinted Polymers in the Analysis of Waters and Wastewaters. *Molecules* **26** (2021). https://doi.org:10.3390/molecules26216515

51 Subrahmanyam, S. *et al.* Optimisation of experimental conditions for synthesis of high affinity MIP nanoparticles. *European Polymer Journal* **49**, 100-105 (2013). https://doi.org:10.1016/j.eurpolymj.2012.09.022

52 Yoshimatsu, K. *et al.* Uniform molecularly imprinted microspheres and nanoparticles prepared by precipitation polymerization: the control of particle size suitable for different analytical applications. *Anal Chim Acta* **584**, 112-121 (2007). https://doi.org:10.1016/j.aca.2006.11.004

53 Zhang, R., Gao, R., Gou, Q., Lai, J. & Li, X. Precipitation Polymerization: A Powerful Tool for Preparation of Uniform Polymer Particles. *Polymers (Basel)* **14** (2022). https://doi.org:10.3390/polym14091851

54 Zhao, W. *et al.* Molecularly imprinted polymeric nanoparticles decorated with Au NPs for highly sensitive and selective glucose detection. *Biosensors and Bioelectronics* **100**, 497-503 (2018). https://doi.org/10.1016/j.bios.2017.09.020

55 Fan, J.-P., Xu, X.-K., Xu, R., Zhang, X.-H. & Zhu, J.-H. Preparation and characterization of molecular imprinted polymer functionalized with core/shell magnetic particles (Fe3O4@ SiO2@ MIP) for the simultaneous recognition and enrichment of four taxoids in Taxus× media. *Chemical Engineering Journal* **279**, 567-577 (2015). https://doi.org/10.1016/j.cej.2015.05.045

56 Qin, F. *et al.* Electrochemical detection of gallic acid in green tea using molecularly imprinted polymers on TiO2@ CNTs nanocomposite modified glassy carbon electrode. *International Journal of Electrochemical Science* **17**, 220426 (2022). https://doi.org/10.20964/2022.04.06

57 Mokhtari, S., Faghihian, H. & Mirmohammadi, M. A core/shell TiO2 magnetized molecularly imprinted photocatalyst (MMIP@ TiO2): synthesis and its photodegradation activity towards sulfasalazine. *Environmental Science and Pollution Research* **30**, 13624-13638 (2023). https://doi.org/10.1007/s11356-022-22792-5

58 Roushani, M. & Zalpour, N. Selective detection of Asulam with in-situ dopamine electropolymerization based electrochemical MIP sensor. *Reactive and Functional Polymers* **169** (2021). https://doi.org:10.1016/j.reactfunctpolym.2021.105069

59 Apodaca, D. C., Pernites, R. B., Ponnapati, R., Del Mundo, F. R. & Advincula, R. C. Electropolymerized Molecularly Imprinted Polymer Film: EIS Sensing of Bisphenol A. *Macromolecules* **44**, 6669-6682 (2011). https://doi.org:10.1021/ma2010525

60 Gavrilă, A.-M., Stoica, E.-B., Iordache, T.-V. & Sârbu, A. Modern and Dedicated Methods for Producing Molecularly Imprinted Polymer Layers in Sensing Applications. *Applied Sciences* **12** (2022). https://doi.org:10.3390/app12063080

61 Arshad, U. *et al.* Molecularly imprinted polymeric coatings for sensitive and selective gravimetric detection of artemether. *RSC Adv* **10**, 34355-34363 (2020). https://doi.org:10.1039/d0ra04785f

62 Mastan, E., Li, X. & Zhu, S. Modeling and theoretical development in controlled radical polymerization. *Progress in Polymer Science* **45**, 71-101 (2015). https://doi.org:10.1016/j.progpolymsci.2014.12.003

63 Truong, N. P., Jones, G. R., Bradford, K. G. E., Konkolewicz, D. & Anastasaki, A. A comparison of RAFT and ATRP methods for controlled radical polymerization. *Nat Rev Chem* **5**, 859-869 (2021). https://doi.org:10.1038/s41570-021-00328-8

64 Hu, Q. *et al.* Electrochemically Controlled RAFT Polymerization for Highly Sensitive Electrochemical Biosensing of Protein Kinase Activity. *Anal Chem* **91**, 1936-1943 (2019). https://doi.org:10.1021/acs.analchem.8b04221

65 Moad, G., Rizzardo, E. & Thang, S. H. RAFT polymerization and some of its applications. *Chem Asian J* **8**, 1634-1644 (2013). https://doi.org:10.1002/asia.201300262

66 Min, H. S. in *Research Aspects in Chemical and Materials Sciences Vol. 5* 16-28 (2022). 10.9734/bpi/racms/v5/4419E

67 Ali, A., Zhang, N. & Santos, R. M. Mineral Characterization Using Scanning Electron Microscopy (SEM): A Review of the Fundamentals, Advancements and Research Directions. *Applied Sciences* **13** (2023). https://doi.org:10.3390/app132312600
68 Huang, L. & Gan, Y. A review on SEM imaging of graphene layers. *Micron* **187**, 103716 (2024). https://doi.org:10.1016/j.micron.2024.103716
69 Scimeca, M., Bischetti, S., Lamsira, H. K., Bonfiglio, R. & Bonanno, E. Energy Dispersive X-ray (EDX) microanalysis: A powerful tool in biomedical research and diagnosis. *Eur J Histochem* **62**, 2841 (2018). https://doi.org:10.4081/ejh.2018.2841
70 Liu, S. & Wang, Y. Application of AFM in microbiology: a review. *Scanning* **32**, 61-73 (2010). https://doi.org:10.1002/sca.20173
71 Giessibl, F. J. Advances in atomic force microscopy. *Reviews of modern physics* **75**, 949 (2003). https://doi.org/10.1103/RevModPhys.75.949
72 Hölscher, H. in *Encyclopedia of nanotechnology* 99-99 (Springer, 2012).
73 Cleveland, J., Anczykowski, B., Schmid, A. & Elings, V. Energy dissipation in tapping-mode atomic force microscopy. *Applied physics letters* **72**, 2613-2615 (1998).
74 Kandapal, S. & Xu, B. Atomic Force Microscopy as a Tool to Study Transport Phenomena in Biological Systems. *Processes* **11** (2023). https://doi.org:10.3390/pr11082430
75 Makan, A. C., Spallek, M. J., du Toit, M., Klein, T. & Pasch, H. Advanced analysis of polymer emulsions: Particle size and particle size distribution by field-flow fractionation and dynamic light scattering. *Journal of Chromatography A* **1442**, 94-106 (2016). https://doi.org/10.1016/j.chroma.2016.03.013
76 Stetefeld, J., McKenna, S. A. & Patel, T. R. Dynamic light scattering: a practical guide and applications in biomedical sciences. *Biophys Rev* **8**, 409-427 (2016). https://doi.org:10.1007/s12551-016-0218-6
77 Li, Y., Lubchenko, V. & Vekilov, P. G. The use of dynamic light scattering and Brownian microscopy to characterize protein aggregation. *Review of Scientific Instruments* **82** (2011). https://doi.org/10.1063/1.3592581
78 Mörters, P. & Peres, Y. *Brownian motion*. Vol. 30 (Cambridge University Press, 2010). https://doi.org/10.1017/CBO9780511750489
79 Karatzas, I., Shreve, S. E., Karatzas, I. & Shreve, S. E. Brownian motion. *Brownian motion and stochastic calculus*, 47-127 (1998).
80 Habib, I. Y., Kumara, N. T. R. N., Lim, C. M. & Mahadi, A. H. Dynamic Light Scattering and Zeta Potential Studies of Ceria Nanoparticles. *Solid State Phenomena* **278**, 112-120 (2018). https://doi.org:10.4028/www.scientific.net/SSP.278.112
81 Bhattacharjee, S. DLS and zeta potential - What they are and what they are not? *J Control Release* **235**, 337-351 (2016). https://doi.org:10.1016/j.jconrel.2016.06.017
82 Bucur, B., Munteanu, F. D., Marty, J. L. & Vasilescu, A. Advances in Enzyme-Based Biosensors for Pesticide Detection. *Biosensors (Basel)* **8** (2018). https://doi.org:10.3390/bios8020027
83 de Jong, L. A., Uges, D. R., Franke, J. P. & Bischoff, R. Receptor-ligand binding assays: technologies and applications. *J Chromatogr B Analyt Technol Biomed Life Sci* **829**, 1-25 (2005). https://doi.org:10.1016/j.jchromb.2005.10.002
84 Fadeel, B. Understanding the immunological interactions of engineered nanomaterials: Role of the bio-corona. *Wiley Interdiscip Rev Nanomed Nanobiotechnol* **14**, e1798 (2022). https://doi.org:10.1002/wnan.1798
85 Cammann, K. *et al.* Chemical Sensors and Biosensors—Principles and Applications. *Angewandte Chemie International Edition in English* **30**, 516-539 (2003). https://doi.org:10.1002/anie.199105161

86 Pang, W. *et al.* Piezoelectric microelectromechanical resonant sensors for chemical and biological detection. *Lab Chip* **12**, 29-44 (2012). https://doi.org:10.1039/c1lc20492k
87 Dickert, F. & Latif, U. in *Comprehensive Supramolecular Chemistry II: 2nd Edition* 201-211 (Elsevier, 2017).
88 Uludağ, Y., Piletsky, S. A., Turner, A. P. & Cooper, M. A. Piezoelectric sensors based on molecular imprinted polymers for detection of low molecular mass analytes. *The FEBS journal* **274**, 5471-5480 (2007).https://doi.org/10.1111/j.1742-4658.2007.06079.x
89 Janata, J. *Principles of chemical sensors*. (Springer Science & Business Media, 2009).
90 Janshoff, A., Galla, H. J. & Steinem, C. Piezoelectric mass-sensing devices as biosensors—an alternative to optical biosensors? *Angewandte Chemie International Edition* **39**, 4004-4032 (2000). https://doi.org/10.1002/1521-3773(20001117)39:22<4004::AID-ANIE4004>3.0.CO;2-2
91 Huang, X., Chen, Q., Pan, W. & Yao, Y. Advances in the mass sensitivity distribution of quartz crystal microbalances: a review. *Sensors* **22**, 5112 (2022). https://doi.org/10.3390/s22145112
92 Latif, U., Can, S., Hayden, O., Grillberger, P. & Dickert, F. L. Sauerbrey and anti-Sauerbrey behavioral studies in QCM sensors—Detection of bioanalytes. *Sensors and Actuators B: Chemical* **176**, 825-830 (2013). https://doi.org/10.1016/j.snb.2012.09.064
93 Alassi, A., Benammar, M. & Brett, D. Quartz crystal microbalance electronic interfacing systems: A review. *Sensors* **17**, 2799 (2017). https://doi.org/10.3390/s17122799
94 Keiji Kanazawa, K. & GORDON, J. I. Frequency of a quartz microbalance in contact with liquid. *Analytical chemistry (Washington, DC)* **57**, 1770-1771 (1985).
95 Kielczynski, P. The analog of the Kanazawa-Gordon formula for cylindrical resonators. *IEEE Transactions on Ultrasonics, Ferroelectrics and Frequency Control* **51**, 1367-1372 (2004). 10.1109/TUFFC.2004.1367474
96 Voglhuber-Brunnmaier, T. & Jakoby, B. Electromechanical resonators for sensing fluid density and viscosity—A review. *Measurement Science and Technology* **33**, 012001 (2021). 10.1088/1361-6501/ac2c4a
97 Chevion, S., Roberts, M. A. & Chevion, M. The use of cyclic voltammetry for the evaluation of antioxidant capacity. *Free radical biology and medicine* **28**, 860-870 (2000). https://doi.org/10.1016/S0891-5849(00)00178-7
98 Heinze, J. Cyclic voltammetry—"electrochemical spectroscopy". New analytical methods (25). *Angewandte Chemie International Edition in English* **23**, 831-847 (1984). https://doi.org/10.1002/anie.198408313
99 Pereira, A. V., Cervini, P. & Cavalheiro, É. T. G. Do voltammetry electrodes modified with MIPs really work? The role of large molecules: folic acid as a probe. *Analytical Methods* **6**, 6658-6667 (2014). https://doi.org/10.1039/C4AY00616J
100 Al Faysal, A., Cetinkaya, A., Erdoğan, T., Ozkan, S. A. & Gölcü, A. Comparative study of two MIP-based electrochemical sensors for selective detection and quantification of the antiretroviral drug lopinavir in human serum. *Talanta* **281**, 126791 (2025). https://doi.org/10.1016/j.talanta.2024.126791
101 Piskin, E., Korkut, F. A., Cetinkaya, A. & Ozkan, S. A. Highly selective and sensitive detection of atorvastatin from using a MIP-based electrochemical sensor. *Journal of Pharmaceutical and Biomedical Analysis Open*, 100061 (2025). https://doi.org/10.1016/j.jpbao.2025.100061
102 Lahcen, A. A. & Amine, A. Recent advances in electrochemical sensors based on molecularly imprinted polymers and nanomaterials. *Electroanalysis* **31**, 188-201 (2019). https://doi.org/10.1002/elan.201800623
103 Piskin, E. *et al.* Development of ultra-sensitive and selective molecularly imprinted polymer-based electrochemical sensor for L-lactate detection. *Microchemical Journal* **204**, 111163 (2024). https://doi.org/10.1016/j.microc.2024.111163

104 LI, X. Research and development of elimination voltammetry. (2024).
105 Mitsugi, J., Kawakita, Y., Egawa, K. & Ichikawa, H. Perfectly Synchronized Streaming From Multiple Digitally Modulated Backscatter Sensor Tags. *IEEE Journal of Radio Frequency Identification* **3**, 149-156 (2019). https://doi.org:10.1109/jrfid.2019.2914246
106 Nirschl, M. *et al.* CMOS-integrated film bulk acoustic resonators for label-free biosensing. *Sensors (Basel)* **10**, 4180-4193 (2010). https://doi.org:10.3390/s100504180
107 Crucho, C. I. C. & Barros, M. T. Polymeric nanoparticles: A study on the preparation variables and characterization methods. *Mater Sci Eng C Mater Biol Appl* **80**, 771-784 (2017). https://doi.org:10.1016/j.msec.2017.06.004
108 Fresco-Cala, B., Batista, A. D. & Cardenas, S. Molecularly Imprinted Polymer Micro- and Nano-Particles. A review. *Molecules* **25** (2020). https://doi.org:10.3390/molecules25204740
109 Wackerlig, J. & Lieberzeit, P. A. Molecularly imprinted polymer nanoparticles in chemical sensing – Synthesis, characterisation and application. *Sensors and Actuators B: Chemical* **207**, 144-157 (2015). https://doi.org:10.1016/j.snb.2014.09.094
110 Zhang, H. Molecularly Imprinted Nanoparticles for Biomedical Applications. *Adv Mater* **32**, e1806328 (2020). https://doi.org:10.1002/adma.201806328
111 Cooney, C. L. & Acevedo, F. Theoretical conversion yields for penicillin synthesis. *Biotechnology and bioengineering* **19**, 1449-1462 (1977).
112 Sheehan, J. C. & Henery-Logan, K. R. The total synthesis of penicillin V. *Journal of the American Chemical Society* **81**, 3089-3094 (1959).
113 Zhang, Z., Li, H., Liao, H., Nie, L. & Yao, S. Influence of cross-linkers' amount on the performance of the piezoelectric sensor modified with molecularly imprinted polymers. *Sensors and Actuators B: Chemical* **105**, 176-182 (2005). https://doi.org:10.1016/j.snb.2004.05.058
114 Wang, L., Pagett, M. & Zhang, W. Molecularly imprinted polymer (MIP) based electrochemical sensors and their recent advances in health applications. *Sensors and Actuators Reports* **5**, 100153 (2023). https://doi.org:https://doi.org/10.1016/j.snr.2023.100153
115 Reindl, M., Zach, V. & Schwaminger, S. P. Biocompatible Poly (acrylic acid-co-methacrylic acid)-Coated Iron Oxide Nanoparticles for Enhanced Adsorption and Antimicrobial Activity of Lasioglossin-III. *ACS Applied Materials & Interfaces* **17**, 16644-16657 (2025). 10.1021/acsami.4c22603
116 Salazar, A. anderson, N. & Stansbury, J. Formulating Mechanically Robust Composite Restorative Materials for High Performance. *Journal of Functional Biomaterials* **16**, 101 (2025).
117 Tian, X. *et al.* A comprehensive study on the application properties of different soft, hard and functional monomers to polyacrylate emulsion and water-based inks. *Journal of Applied Polymer Science* **142**, e56473 (2025). https://doi.org/10.1002/app.56473
118 Maciejewska, M. & Rogulska, M. Porous Copolymers of 3-(Trimethoxysilyl) propyl Methacrylate with Trimethylpropane Trimethacrylate Preparation: Structural Characterization and Thermal Degradation. *Materials* **17**, 4796 (2024). https://doi.org/10.3390/ma17194796
119 Cegłowski, M., Kurczewska, J., Lusina, A., Nazim, T. & Ruszkowski, P. EGDMA-and TRIM-based microparticles imprinted with 5-fluorouracil for prolonged drug delivery. *Polymers* **14**, 1027 (2022). https://doi.org/10.3390/polym14051027
120 Chesnokov, S. A. *et al.* Porous Polymer Scaffolds based on Cross-Linked Poly-EGDMA and PLA: Manufacture, Antibiotics Encapsulation and In Vitro Study. *Macromolecular Bioscience* **21**, 2000402 (2021). https://doi.org/10.1002/mabi.202000402
121 Winning, D. *et al.* Thermoresponsiveness Across the Physiologically Accessible Range: Effect of Surfactant, Cross-Linker and Initiator Content on Size, Structure and Transition Temperature of Poly (N-isopropylmethacrylamide) Microgels. *ACS omega* **9**, 36185-36197 (2024). 10.1021/acsomega.4c02115

122 Tom, L. A., Schneck, N. A. & Walter, C. Improving the imprinting effect by optimizing template: monomer: cross-linker ratios in a molecularly imprinted polymer for sulfadimethoxine. *Journal of Chromatography B* **909**, 61-64 (2012). https://doi.org/10.1016/j.jchromb.2012.10.020
123 Glad, M., Reinholdsson, P. & Mosbach, K. Molecularly imprinted composite polymers based on trimethylolpropane trimethacrylate (TRIM) particles for efficient enantiomeric separations. *Reactive polymers* **25**, 47-54 (1995). https://doi.org/10.1016/0923-1137(95)00018-E
124 Yoshimatsu, K., Yamazaki, T., Chronakis, I. S. & Ye, L. Influence of template/functional monomer/cross-linking monomer ratio on particle size and binding properties of molecularly imprinted nanoparticles. *Journal of Applied Polymer Science* **124**, 1249-1255 (2012). https://doi.org/10.1002/app.35150
125 Müller, K., Klapper, M. & Müllen, K. Synthesis of conjugated polymer nanoparticles in non-aqueous emulsions. *Macromolecular rapid communications* **27**, 586-593 (2006). https://doi.org/10.1002/marc.200600027
126 Luliński, P. & Maciejewska, D. Impact of functional monomers, cross-linkers and porogens on morphology and recognition properties of 2-(3,4-dimethoxyphenyl)ethylamine imprinted polymers. *Materials Science and Engineering: C* **31**, 281-289 (2011). https://doi.org:10.1016/j.msec.2010.09.010
127 Saha, K., Agasti, S. S., Kim, C., Li, X. & Rotello, V. M. Gold nanoparticles in chemical and biological sensing. *Chem Rev* **112**, 2739-2779 (2012). https://doi.org:10.1021/cr2001178
128 Zhang, G. Functional gold nanoparticles for sensing applications. *Nanotechnology Reviews* **2**, 269-288 (2013). https://doi.org:10.1515/ntrev-2012-0088
129 Fischer, M. J. in *Surface plasmon resonance: methods and protocols* 55-73 (Springer, 2010).
130 Leekumjorn, S., Gullapalli, S. & Wong, M. S. Understanding the solvent polarity effects on surfactant-capped nanoparticles. *J Phys Chem B* **116**, 13063-13070 (2012). https://doi.org:10.1021/jp307985c
131 Tiani, D. J. & Pemberton, J. E. Emersion of 11-mercapto-1-undecanol-modified Ag substrates from aqueous and nonaqueous solvents: The effect of emersion velocity on emersed solvent layer thickness. *Langmuir* **19**, 6422-6429 (2003).
132 Gupta, R. K., Srinivasan, M. & Dharmarajan, R. Synthesis of 16-Mercaptohexadecanoic acid capped gold nanoparticles and their immobilization on a substrate. *Materials Letters* **67**, 315-319 (2012). https://doi.org/10.1016/j.matlet.2011.09.047
133 Zhou, L., Zhao, Y. & Ma, H. Experimental investigation on stability and thermal conductivity of dodecanethiol-coated copper nanofluids. *Journal of Nanoparticle Research* **22**, 199 (2020). 10.1007/s11051-020-04943-2
134 Monge, S., Darcos, V. & Haddleton, D. M. Effect of DMSO used as solvent in copper mediated living radical polymerization. *Journal of Polymer Science Part A: Polymer Chemistry* **42**, 6299-6308 (2004). https://doi.org/10.1002/pola.20403
135 Sam, S. *et al.* Semiquantitative study of the EDC/NHS activation of acid terminal groups at modified porous silicon surfaces. *Langmuir* **26**, 809-814 (2010). 10.1021/la902220a
136 Raghav, R. & Srivastava, S. Immobilization strategy for enhancing sensitivity of immunosensors: L-Asparagine–AuNPs as a promising alternative of EDC–NHS activated citrate–AuNPs for antibody immobilization. *Biosensors and Bioelectronics* **78**, 396-403 (2016). https://doi.org/10.1016/j.bios.2015.11.066
137 Elahi, M. F., Guan, G., Wang, L. & King, M. W. Influence of layer-by-layer polyelectrolyte deposition and EDC/NHS activated heparin immobilization onto silk fibroin fabric. *Materials* **7**, 2956-2977 (2014). https://doi.org/10.3390/ma7042956

Scientific Contribution

International Conferences

1. In-situ Synthesis of MIP Thin Films on QCM Electrodes to Sense Engineered Nanoparticles M. Bagheri, I. Selvistrovich, S. Haghdoust, P. Lieberzeit
   EUROSENSORS XXXVI International Conference, 1–4 September **2024**, Poster presentation
   https://www.ama-science.org/proceedings/details/5475
2. In-situ Synthesis of MIP to Detect Au Nanoparticles on QCM, M. Bagheri, P. Lieberzeit
   International Conference on Molecular Imprinting 2024, 19–21 June **2024**, Poster Presentation
   http://mip2024.com/index.php
3. Sensing Penicillin V in Aqueous Media with-MIP Nanoparticle Coatings on QCM, M. Bagher, O. Gatterbauer, P. Lieberzeit
   SMSI **2021**- Sensors and Instrument, 03-06 May **2021** (digital), Oral Presentation
   10.5162/SMSI2021/B4.2
4. Synthesis of MIP Nanoparticles for Selective Sensing of Penicillin V, M. Bagher, O. Gatterbauer, P. Lieberzeit
   SMSI **2021**- Sensors and Instrument, Poster presentation
   10.5162/SMSI2020/B3.4

Vienna Doctoral School of Chemistry (DosChem) Retreats

1. Exploring the Influence of Diverse Thiol Compounds in Surface Modification of Au NPs for Enhanced Removal from MIP, Mahdieh Bagheri, Peter A. Lieberzeit
   Panel A, 19-20 February **2024** in Hungary, Poster Presentation
2. In-situ synthesis of Molecularly Imprinted Polymers to Detect Au Nanoparticles on QCM, Mahdieh Bagheri, Shahin Haghdoust, Peter A. Lieberzeit
   Panel A, 15-17 March **2023** in Zeillern, Poster presentation
3. In-Situ polymerization and template removal techniques to synthesize Gold Nanoparticles MIPs, Mahdieh Bagheri, Peter A. Lieberzeit
   Panel A, 31.05-02.06 **2022** in Styria, Oral Presentation
4. Multi object optimization of MIP NPs for specific detection of Penicillin VK, Mahdieh Bagheri, Peter A. Lieberzeit
   Panel A, 15-17 November **2021** in Abbey Seitenstetten, Poster presentation

Publication

Zhang, Xiaorong, Aysu Yarman, Mahdien Bagheri, Ibrahim M. El-Sherbiny, Rabeay Y. A. Hassan, Sevinc Kurbanoglu, et al. “Imprinted Polymers on the Route to Plastibodies for Biomacromolecules (MIPs), Viruses (VIPs), and Cells (CIPs).” In Trends in Biosensing Research: Advances, Challenges and Applications, edited by Fred Lisdat and Nicolas Plumeré, 107–48. Advances in Biochemical Engineering/Biotechnology, vol. 187. Cham: Springer Nature Switzerland, **2024**. https://doi.org/10.1007/978-3-031-56913-5